

UC Berkeley

UC Berkeley Electronic Theses and Dissertations

Title

Tuning the Magnetic and Electronic Properties of $\text{Fe}_x\text{Si}_{1-x}$ Thin Films for Spintronics

Permalink

<https://escholarship.org/uc/item/1rh5j140>

Author

Karel, Julie Elizabeth

Publication Date

2012

Peer reviewed|Thesis/dissertation

Tuning the Magnetic and Electronic Properties of $\text{Fe}_x\text{Si}_{1-x}$
Thin Films for Spintronics

By

Julie Elizabeth Karel

A dissertation submitted in partial satisfaction of the
requirements for the degree of

Doctor of Philosophy

in

Engineering – Materials Science and Engineering

in the

Graduate Division

of the

University of California, Berkeley

Committee in charge:

Professor Frances Hellman, Chair

Professor Ronald Gronsky

Professor Zi Qiang Qiu

Fall 2012

Tuning the Magnetic and Electronic Properties of $\text{Fe}_x\text{Si}_{1-x}$ Thin Films for Spintronics

Copyright 2012
by
Julie Elizabeth Karel

Abstract

Tuning the Magnetic and Electronic Properties of $\text{Fe}_x\text{Si}_{1-x}$ Thin Films for Spintronics

by

Julie Elizabeth Karel

Doctor of Philosophy in Engineering – Materials Science and Engineering

University of California, Berkeley

Professor Frances Hellman, Chair

Advances in traditional CMOS devices, in pursuit of Moore's Law, have lead to the detrimental side effects of increased energy consumption and heat generation. Spintronic (spin-electronic) devices are a potential alternative to standard charge-based devices where the electron spin carries the information instead. Many proposed spintronic devices require a spin-injector, a material that can produce a highly spin-polarized current, and consequently significant work has gone into identifying these types of materials. $\text{Ga}_y\text{Mn}_{1-y}\text{As}$, the canonical dilute magnetic semiconductor, has been touted as a promising material in this capacity since it is theoretically predicted to be 100% spin polarized and offers the possibility to electrically tune the ferromagnetism. However, the Curie temperature remains low (~ 150 K), making the material unsuitable for room-temperature spintronic applications.

This dissertation investigated the magnetic and electronic properties of a potentially better alternative: off-stoichiometry, bcc-like $\text{Fe}_x\text{Si}_{1-x}$ thin films ($0.43 < x < 0.77$). Stoichiometric Fe_3Si , a Heusler alloy, has already been studied as a potential spin-injector due to a high Curie temperature, well above room temperature (> 800 K) and theoretically predicted high spin polarization (100%). However, little work has been done on off-stoichiometry $\text{Fe}_x\text{Si}_{1-x}$ thin films ($0.43 < x < 0.77$), where it may be possible to further enhance the properties, including the spin-polarization. In addition to being a potential spin-injector, the $\text{Fe}_x\text{Si}_{1-x}$ system is unique in that thin film growth techniques allow access to varying degrees of both chemical and structural order over a wide composition range. In the crystalline system, three different bcc-like structures (D0_3 , B2, A2), each with a different degree of chemical order, are possible. The A2 structure is a chemically disordered random bcc solid solution, and the B2 structure is a partially ordered CsCl structure with Fe on the cube corner sites and Fe/Si randomly arranged on the body center sites. Finally, the D0_3 structure is chemically ordered with Fe on the cube corners and Fe and Si alternating in the body centers. Amorphous $\text{Fe}_x\text{Si}_{1-x}$ thin films can also be fabricated, allowing for a comprehensive and direct comparison of the magnetic properties. This work probed the effects of chemical and structural disorder on the magnetic and electronic properties of $\text{Fe}_x\text{Si}_{1-x}$ thin films.

The local chemical order in epitaxial $\text{Fe}_x\text{Si}_{1-x}$ thin films was characterized using conversion electron Mössbauer spectrometry (CEMS); X-ray absorption fine structure (XAFS) and density functional theory (DFT) were used to characterize the local environments in the amorphous films. CEMS showed films have B2 chemical order for $x \leq 0.65$ and D0_3 for $x > 0.65$. Even very far from the equilibrium composition, $x=0.75$, the films still tended towards chemical order; the A2 structure was not successfully fabricated. Both theoretical DFT calculations and X-ray absorption fine structure for the amorphous materials indicate a local atomic structure that is well-ordered for Fe-Si pairs and less ordered for Fe-Fe; calculated and experimental interatomic distances are similar to a bcc structure, however with a decreased coordination number. Experimental and theoretical number densities in the amorphous structures are less than in the crystalline phase.

The magnetism was found to strongly depend on the chemical order for both the crystalline and amorphous structures. The chemically disordered A2 structure has more Fe-Fe pairs than the chemically ordered B2 or D0_3 structures, leading to a larger predicted moment. The magnetic moments for the B2 and D0_3 structures are not significantly different. They should, in fact, be essentially the same since the first nearest neighbor environments are the same; on average there are the same number of Fe-Fe first nearest neighbor pairs in both structures. Only the second nearest neighbor environments, which have a weaker effect on the magnetic moment, are different. An enhanced magnetic moment due to enhanced spin and orbital moments was observed in all amorphous films versus crystalline films of the same composition. The amorphous local environments (based on the fraction of Fe-Fe nearest neighbors, $N^1_{\text{Fe-Fe}}/\text{CN}^1$) are approximately intermediate between the chemically disordered A2 structure and the chemically ordered D0_3 or B2 structures; the amorphous materials, while structurally disordered, are only partially chemically disordered. The amorphous materials have a different structure; there are however more Fe-Fe pairs than the D0_3 or B2 structures (although less than A2), explaining the observed enhanced moment.

Not surprisingly, the electronic properties were also found to depend strongly on chemical and structural order, based on hard X-ray photoemission spectroscopy and DFT calculations. The core-level peaks in the amorphous structure ($x=0.67$) show little broadening despite a significant energy shift, suggesting that the local environment around the Si atoms is different than in the crystalline materials but far more uniform than expected, consistent with XAFS results, which showed that Si is well-ordered. A well-resolved Si 2p spin-orbit splitting for two epitaxial alloys, $x=0.72$ (D0_3) and 0.67 (B2) suggests that nearest-neighbor interactions are the dominant effect on binding energy for the Si atoms in the sample. The Si 2p peak in the amorphous sample also shows spin-orbit splitting, another indication that the local structure around each Si atom is relatively well defined. The valence bands show a broadening of the features when chemical and structural disorder is increased, consistent with theoretical band structure calculations for D0_3 , B2, A2 and amorphous structures.

The electronic structure calculations reveal that the spin-polarization, $|P|$, is relatively insensitive to x in the amorphous structures and is negative and comparable in magnitude to the B2 structure. It is larger, by more than a factor of 3, than $|P|$ in the hypothetical A2 structure. The D0₃ structure has the largest $|P|$. Remarkably, Andreev reflection measurements reveal that the spin polarization in the amorphous film ($x=0.65$) is significantly larger than the epitaxial (B2) film ($x=0.65$). In fact, the spin polarization of the amorphous film is larger than spin polarization measurements by Andreev reflection reported on an $x=0.75$ (D0₃) epitaxial film.

Lastly, the anomalous Hall effect, observed in all films, was very large in the amorphous films versus epitaxial films with the same composition. To investigate the origins of the AHE, σ_{xy}/M_z was plotted versus σ_{xx} , allowing for comparison to recent theoretical calculations. In the epitaxial films, σ_{xy}/M_z is constant, meaning the AHE is dominated by the intrinsic mechanism, as predicted theoretically in this moderate longitudinal conductivity regime. The AHE in the low conductivity regime (amorphous films) shows a scaling with conductivity similar to that seen in low conductivity GaMnAs films despite much larger disorder and carrier concentration in the amorphous films. The AHE scaling in these material systems was compared to other materials in the low conductivity regime, and all were found to be approximately linearly dependent on the longitudinal conductivity, suggesting dependence on the number of carriers.

Table of Contents

Chapter 1: Background and Motivation	1
Chapter 2: Thin Film Growth and Characterization	9
2.1 Thin Film Deposition	9
2.2 X-ray Diffraction	9
2.3 Transmission Electron Microscopy	14
2.4 Rutherford Backscattering Spectrometry	18
2.5 Electronic Transport and Hall Effect	18
2.6 Magnetic Characterization	20
2.7 Synchrotron Techniques	21
2.7.1 Hard X-ray Photoemission Spectroscopy	21
2.7.2 X-ray Absorption Fine Structure	21
2.7.3 X-ray Absorption Spectroscopy and X-ray Magnetic Circular Dichroism	22
Chapter 3: Chemical Order and Magnetization in Epitaxial Off-Stoichiometry	
Fe_xSi_{1-x} Thin Films.....	24
3.1 Introduction.....	24
3.2 Methods.....	25
3.2.1 Theoretical Density Functional Theory (DFT) Calculations	25
3.2.2 Experimental Procedure.....	26
3.3 Results	27
3.3.1 Structural Characterization and Chemical Order.....	27
3.3.2 Electronic Properties.....	33
3.3.3 Magnetic Properties	35
3.4 Discussion.....	36
3.5 Conclusion	38
Chapter 4: Magnetism and Local Atomic Structure in Amorphous Fe_xSi_{1-x} Thin	
Films	39
4.1 Introduction.....	39
4.2 Methods.....	40
4.2.1 Theoretical DFT Calculations	40
4.2.2 Experimental Procedure.....	41
4.3 Results.....	42
4.3.1 Magnetism	42
4.3.1.A. Theoretical DFT Calculations	42
4.3.1.B. Experimental Thin Film Magnetism	42
4.3.2 Local Atomic Structure.....	45
4.3.2.A. Theoretical DFT Calculations	45
4.3.2.B. Experimental Structural Characterization	48
4.3.3 Electronic Structure and Spin Polarization	51
4.3.3.A. Theoretical DFT Calculations	51
4.3.3.B. Experimental Spin Polarization Measurements	52

4.4 Discussion	54
4.5 Conclusion	55
Chapter 5: Hard X-ray Photoemission Spectroscopy in $\text{Fe}_x\text{Si}_{1-x}$ Thin Films	56
5.1 Introduction	56
5.2 Experimental Methods	56
5.3 Results and Discussion	57
5.3.1 Core Level Spectra	57
5.3.2 Valance-Band Spectra	60
5.3.3 Theoretical Analysis	61
5.4 Conclusion	64
Chapter 6: Electronic Transport and the Anomalous Hall Effect in $\text{Fe}_x\text{Si}_{1-x}$ Thin Films	66
6.1 Introduction	66
6.2 Experimental Procedure	67
6.3 Results and Discussion	67
6.4 Conclusion	75
Chapter 7: Conclusion	76
Bibliography	77
Appendix A: Anomalous Hall Effect and Out-of-Plane Magnetization	82
Appendix B: In-plane and Out-of-Plane Magnetization	84

List of Figures

1.1 Fe ₃ Si crystal structure. Fe atoms occupy two non-equivalent sites in the lattice	2
1.2 Partial Fe-Si binary phase diagram	3
1.3 Off-stoichiometry ($x < 0.75$) (a) D0 ₃ and (b) B2 structures.	4
1.4 Temperature coefficient of resistivity, α , versus resistivity for bulk alloys (+), thin films (•) and amorphous alloys (x). Figure and caption from ref [38].	6
2.1 Representative X-ray diffraction patterns. (a) θ -2 θ scans for $x=0.72$ (black) and $x=0.67$ (red) epitaxial films. (b) ϕ scans on in-plane 220 peak for $x=0.72$ (black) and 110 peak for $x=0.67$ (red)	10
2.2 Out of plane lattice constants for Fe _x Si _{1-x} epitaxial films calculated from the X-ray diffraction superlattice peak.	11
2.3 Calculated and experimental ratio of superlattice to fundamental X-ray diffraction peak for epitaxial Fe _x Si _{1-x} thin films.	13
2.4 θ -2 θ X-ray diffraction scan from two amorphous Fe _x Si _{1-x} thin films, $x=0.55$ and $x=0.60$	14
2.5 TEM image and electron diffraction pattern (inset) for the amorphous film $x=0.67$. The image displays a ~5 nm diameter nanocrystal (circled) in an amorphous matrix. In addition to strong spots from the <110>-oriented Si substrate, the electron diffraction pattern shows a broad diffuse ring originating from the amorphous film, as well as some random spots due to nanocrystals. (Images courtesy of D. Smith).....	15
2.6 TEM image from $x=0.55$ amorphous sample. Poorly formed lattice fringes are highlighted. (Image courtesy of D. Smith)	15
2.7 (a) Bright field TEM image and (b) electron diffraction pattern from an epitaxial $x=0.55$ thin film. The arrow in (a) indicates the [100] direction. ~10% of the sample is not oriented in the [100] direction (top left corner of bright field image). In (b), the reflections corresponding to the MgO substrate are indexed below the spot in white. The MgO zone axis is <100>. The reflections from the film are indexed to the B2 structure above the spot in purple (unless indicated with an arrow); arrows were used when the spots were faint or too close to other spots. The zone axis for the film is <110>. Note that the 002 MgO substrate reflection and the -110 film reflection are the same spot. Superlattice reflections (i.e. 001 and 111) for the film are also indicated. The yellow circles correspond to diffraction spots from the top left corner of the bright field image. (Image courtesy of D. Smith).....	17
2.8 Experimental RBS data and fit for an amorphous $x=0.43$ film on SiN _x on Si.....	18
2.9 Image of hall bar with schematic of experimental setup. Different orientations of the applied magnetic field with respect to the device are shown as (a), (b) and (c). Orientation	

(a) is used in Hall effect and magnetoresistance measurements, and (b) and (c) are for magnetoresistance measurements.	20
2.10 Raw XAS spectra for amorphous $x=0.60$, showing an energy shift between scans..	23
3.1. (a) $D0_3$ crystal structure for $x=0.75$ and off-stoichiometry ($x<0.75$) (b) $D0_3$ and (c) B2	24
3.2. Experimental and calculated superlattice to fundamental peak intensity ratios versus x . The inset shows the lattice constants versus x , calculated from the superlattice peak ..	28
3.3. (a) Bright field TEM image and (b) electron diffraction pattern from an epitaxial $x=0.55$ thin film. The arrow in (a) indicates the [100] direction. ~10% of the sample is not oriented in the [100] direction (top left corner of bright field image). In (b), the reflections corresponding to the MgO substrate are indexed below the spot in white. The MgO zone axis is $\langle 100 \rangle$. The reflections from the film are indexed to the B2 structure above the spot in purple (unless indicated with an arrow); arrows were used when the spots were faint or too close to other spots. The zone axis for the film is $\langle 110 \rangle$. Note that the 002 MgO substrate reflection and the -110 film reflection are the same spot. Superlattice reflections (i.e. 001 and 111) for the film are also indicated. The yellow circles correspond to diffraction spots from the top left corner of the bright field image. (Image courtesy of D. Smith).....	30
3.4. Measured CEM spectra at 293 K of epitaxial Fe_xSi_{1-x} films on MgO (001) for (a) $x=0.77$, (b) $x=0.75$, (c) $x=0.65$ and (d) $x=0.55$. The right-hand side shows the hyperfine field distribution, $P(B_{hf})$, for each sample. Corresponding least-squared fitted components (labeled 1-4) are shown below the spectra for (a) and (b); the spectra in (c) are fit with $P(B_{hf})$	31
3.5. (a) Experimental Fe L-edge X-ray absorption spectra and (b) theoretical XAS for $x=0.55-1.0$	33
3.6. Bloch spectral functions for (a) the $x=0.55$ B2 structure and (b) non-magnetic bcc Fe. The circles in (a) indicate the flat bands with d-character, and the arrows in (b) show the same bands at higher energy	34
3.7. Experimental magnetic moments measured at 2 K for Fe_xSi_{1-x} epitaxial films and CPA and supercell theoretical calculations for different chemical order – A2, B2 and $D0_3$	35
3.8. $M(T)$ for $x=0.65$ and 0.55 at $H=1000$ Oe	36
3.9. Experimental and CPA calculated (a) spin and (b) orbital moments $x=0.55-1.0$ at 300 K. The $x=0.55$ composition is measured at 79 K, as indicated.....	36
4.1. Magnetization at 2 K versus Fe concentration for Fe_xSi_{1-x} amorphous and crystalline materials. Solid symbols are experimental data: amorphous films (red squares) and epitaxial films (blue stars). Open symbols are theory: amorphous (red stars), A2 (half filled black circle), B2 (blue triangle), $D0_3$ (blue square with cross). The red and blue dashed lines are a guide to the eye. The error is less than the size of the data points	43

4.2. (a) M(H) for amorphous and epitaxial $x=0.65$, (b) normalized M(T) measurements for amorphous and epitaxial $x=0.65$ and $x=0.55$, (c) M(T) measurements for all amorphous films and (d) normalized M vs H/T for $x=0.45$ and Brillouin functions ($S=1/2$, $3/2$) at 2 K.	44
4.3. XAS spectra for (a) epitaxial and (b) amorphous films.	45
4.4. (a) Spin and (b) orbital moments, calculated from the sum rules versus x for amorphous and epitaxial thin films. Measurements were performed at 300 K (except as indicated) in ± 0.5 T. Symbols are experimental data: amorphous films (red squares) and epitaxial films (blue stars). The $x=0.55$ data enclosed by a box is at 79 K	45
4.5. Total number density versus Fe concentration for $\text{Fe}_x\text{Si}_{1-x}$ amorphous and crystalline materials. Solid symbols are experimental data: amorphous films (red squares) and epitaxial films (blue stars). Open symbols are theory: amorphous (red stars), A2 (half filled black circle), B2 (blue triangle), D0 ₃ (blue square with cross). The red and blue dashed lines are a guide to the eye.....	46
4.6. The calculated total pair correlation function, $g_{tot}(r)$, (black) of $\text{Fe}_x\text{Si}_{1-x}$ amorphous alloys, (a) $x=0.55$ and (b) $x=0.65$. The green and blue shades display the fitted Gaussians of the first peak, and the red is the sum of the two fits. The $g_{tot}(r)$ of D0 ₃ Fe_3Si is represented by the magenta lines. The insets display two typical structures of Fe (blue) and Si (yellow) atoms around an Fe atom within 2.3~2.6 Å.	47
4.7. Fe K-edge Fourier transformed XAFS, $ \chi(R) $, for amorphous $\text{Fe}_x\text{Si}_{1-x}$ samples.	49
4.8. Fourier transformed XAFS $ \chi(R) $ and fit for $x=0.45$. The inset is the XAFS in k -space, weighted by k^2 and the fit.	50
4.9. Calculated density of states (a) for the amorphous structures with various x and (b) for crystalline and amorphous structures near $x=0.65$	51
4.10. The absolute value of spin-polarization, $ P $, at E_F (solid squares, left axis) and M_{total} (half open squares, right axis) for (a) the amorphous structures with various x and (b) crystalline and amorphous structures with $x \sim 0.65$. P is positive for D0 ₃ and B2 and negative for A2 and all amorphous structures.	52
4.11. Representative conductance curves (with Pb tip) obtained from amorphous and crystalline $x=0.65$ samples with (a) small Z factor and (b) large Z factor. Open squares are experimental data for the crystalline sample; open circles are for the amorphous sample. The solid and dashed lines are the best fit to the data with the parameters listed in the inset.....	53
4.12. The spin polarization of crystalline (open squares) and amorphous (open circles) $x=0.65$ thin films as a function of Z factor. The dashed lines are a guide to the eye.....	53
5.1. Si 1s core peak spectra obtained for all three samples – epi- $\text{Fe}_{0.72}\text{Si}_{0.28}$, epi- $\text{Fe}_{0.67}\text{Si}_{0.33}$ and α - $\text{Fe}_{0.67}\text{Si}_{0.33}$	58
5.2. (a) Experimental Fe 2p spectra collected for all three samples, which do not exhibit any evidence of iron oxidation. (b) Fe 3s and Si 2p spectra obtained for all three samples. Fe 3s also does not show evidence of oxidation.	59

5.3. (a) Extended valence-band spectra obtained for all three samples, including the valence-band features labeled A-D and the sub-valence feature, later decomposed into four components (P1-P4), and normalized to the high-binding energy inelastic background tail. (b) Higher-binding energy valence feature, background-subtracted and fitted, with a dominant peak (P2) corresponding to the photoemission from O 2s levels in the SiO ₂ layer	61
5.4. Total calculated densities of states for ordered D0 ₃ Fe ₃ Si (used as the model for epi-Fe _{0.72} Si _{0.28}), partially disordered FeFe _{0.3} Si _{0.7} in the B2 structure (epi-Fe _{0.67} Si _{0.33}), and for chemically disordered bcc Fe _{0.67} Si _{0.33} , used for the amorphous a-Fe _{0.67} Si _{0.33} sample	62
5.5. Calculated element- and site- resolved angle-integrated XPS spectra for ordered D0 ₃ Fe ₃ Si (used to model epi-Fe _{0.72} Si _{0.28}), including 230 meV broadening due to the total experimental resolution.....	63
5.6. Room temperature XPS spectra for (a) ordered D0 ₃ Fe ₃ Si (used to model epi-Fe _{0.72} Si _{0.28}), (b) partially disordered FeFe _{0.3} Si _{0.7} in the B2 structure (used to model epi-Fe _{0.67} Si _{0.33}), and (c) chemically disordered bcc a-Fe _{0.67} Si _{0.33} at a photon energy of 5950.3 eV compared to calculated one-step theoretical spectra shown in grey. The black curves represent a broadening of the theoretical spectra with a 230 meV (FWHM) Gaussian to simulate the experimental resolution. Experimental data, normalized to the high-binding energy inelastic background tail are shown in red.....	64
6.1. (a) Resistivity versus temperature for amorphous films [A] and epitaxial films [E] of varying x. (b) Temperature coefficient of resistivity, α , versus longitudinal resistivity, ρ_{xx} , at 2 K for amorphous and partially crystalline films. The line is a guide to the eye.	68
6.2. In-plane magnetization versus field at 2 K for amorphous [A] and epitaxial [E] films of varying x. The inset in shows $M(H)$ of amorphous $x=0.43$ and 0.45 films on an expanded y-scale. The temperature-independent diamagnetic contribution (visible at high fields, same for H in-plane or out-of-plane) has been removed from all the data.	69
6.3. Magnetoresistance, $\Delta\rho_{xx}$, [$\Delta\rho_{xx}=\rho_{xx}(H)-\rho_{xx}(0)$] versus applied field with (a) H applied perpendicular to the film and I , with (b) H applied in the film plane and parallel to I and with (c) H in the film plane and perpendicular to I at various T for amorphous $x=0.43$	70
6.4. Hall Resistivity ρ_{xy} vs H at 2 K for amorphous [A] and epitaxial [E] films of various x . $\rho_{xy}(H) \propto M_z(H)$ for all samples. For $x=0.43$ and 0.45 , a small additional contribution to $\rho_{xy}(H)$ due to the ordinary Hall effect can be seen. The inset shows normalized out of plane magnetization (black squares) and normalized ρ_{xy} (AHE) (purple squares) at 2K for $x=0.43$. ρ_{xy} (OHE) has been subtracted from the data.....	71
6.5. σ_{xy}/M_z versus σ_{xx} for amorphous and epitaxial Fe _x Si _{1-x} thin films and GaMnAs thin films from [120]. The lines are fits to the low σ_{xx} data; $\sigma_{xy}/M_z \propto \sigma_{xx}^n$ with $n=1.3$ (Fe _x Si _{1-x}) and 0.8 (Ga _{1-y} Mn _y As).....	72
6.6. σ_{xx} versus n_h , with the relationship $\sigma_{xx} \propto n_h^{0.77}$ for the amorphous and epitaxial Fe _x Si _{1-x} thin films at 2 K and Ga _{1-y} Mn _y As at 15 K from ref [120]	73

6.7. $\sigma_{xy}/M_z n_h^{2/3}$ versus $\sigma_{xx}/n_h^{2/3}$ at 2 K for amorphous and epitaxial $\text{Fe}_x\text{Si}_{1-x}$ thin films and at 15 K for $\text{Ga}_{1-y}\text{Mn}_y\text{As}$ thin films from [120]	74
6.8. σ_{xy}/M_z versus σ_{xx} for epitaxial and amorphous $\text{Fe}_x\text{Si}_{1-x}$ thin films and previously reported itinerant ferromagnets and magnetic semiconductors. ^{24,51,52,63,120,130,131,132,133} The line is a fit to the low σ_{xx} data; $\sigma_{xy}/M_z \propto \sigma_{xx}^{1.6}$	75
A.1. Normalized out of plane magnetization (black squares) and normalized ρ_{xy} (AHE) (red squares) for amorphous (a) $x=0.71$ and (b) $x=0.65$ films	82
A.2. Normalized out of plane magnetization (black squares) and normalized ρ_{xy} (AHE) (red squares) for the amorphous $x=0.55$ film.....	82
A.3. Normalized out of plane magnetization (black squares) and normalized ρ_{xy} (AHE) (red squares) for amorphous (a) $x=0.45$ and (b) $x=0.43$ films. ρ_{xy} (OHE) has been subtracted from the data.....	83
A.4. Normalized out of plane magnetization (black squares) and normalized ρ_{xy} (AHE) (red squares) for epitaxial (a) $x=0.71$ and (b) $x=0.67$ films.....	83
B.1. In-plane and out-of-plane $M(H)$ curves at 2 K for an amorphous $x=0.55$ sample. Amorphous and epitaxial samples with $x \geq 0.55$ exhibited similar results.....	84
B.2. In-plane and out-of-plane $M(H)$ curves at 2 K for amorphous (a) $x=0.45$ and (b) $x=0.43$ thin films	84

List of Tables

2.1 Chemical coherence length for epitaxial $\text{Fe}_x\text{Si}_{1-x}$ thin films	12
3.1 Values of the isomer shift (δ), magnetic hyperfine field (B_{hf}) and relative spectral area (A_r) of the different components (Comp.) deduced from the least-squared fit of the Mössbauer spectra of $\text{Fe}_x\text{Si}_{1-x}$ thin films.	32
3.2 Short range order parameter, $P(4)$, for samples with D0 ₃ and B2 structure. The sample with composition $x=0.55$ is not reported since CEMS revealed a paramagnet at room temperature.	32
4.1 Coordination number, bond length and mean square disorder in bond length from DFT calculations or determined from fits to experimental XAFS data for first shell (grey) and second shell (white).	48

Acknowledgments

Graduate school is a journey, both personally and professionally. With a healthy dose of humility, patience, curiosity, hard work, a positive attitude and support, one can truly accomplish anything. Many people helped me during this process, and I would be remiss to not acknowledge the guidance and expertise of the people I have had the pleasure of working with over the last 5 years.

First and foremost, I have to thank my advisor, Professor Frances Hellman, for offering me the opportunity to come to Berkeley and spend every day doing what I love. You gave me the freedom to pursue my research interests with the guidance I needed to succeed. You showed me how to be a scientist. I also have to acknowledge Professor Ronald Gronsky and Professor Zi Qiang Qiu for their time serving as members of my qualifying exam and dissertation committees. I would also like to recognize the invaluable support of Professor Ronald Gronsky. I have had the honor and privilege of working with you, and your stewardship of the department and commitment to the university is truly exemplary.

Next, I would like to thank all of the members of the Hellman Lab, past and present, who have made coming into work every day enjoyable. Daniel Queen, David Cooke, Hyeon-Jun Lee and Zoe Boekelheide provided support, helpful suggestions and showed me how to do almost everything. You were always available to help me and were a pleasure to work with; I couldn't be more grateful. Chloe Baldasseroni, your attention to detail and desire to do things right the first time have been an inspiration to me. It has been wonderful to work with a friend every day. Catherine Bordel has supported me in every way, both professionally and personally. You have taught me so much, and I am honored to have worked with you. I couldn't have done it without you.

Science is inherently collaborative, and this dissertation would not exist without the scientific expertise and guidance of the following people. Dr. Jeff Kortright, Dr. Kevin Stone, Dr. Catherine Jenkins and Dr. Elke Arenholz assisted in X-ray absorption spectroscopy and X-ray magnetic circular dichroism measurements and analysis. Dr. Jean Juraszek took and analyzed beautiful conversion electron Mössbauer spectrometry data. Professor Ruqian Wu and Dr. Yanning Zhang provided insightful density functional theory (DFT) calculations on the amorphous structures, and Dr. Jan Minar did the same for the crystalline materials. I am grateful to Dr. Steve Heald who generously taught me X-ray absorption fine structure measurements and analysis. Professor David Smith did cross-sectional transmission electron microscopy on my samples, and Professor Tingyong Chen performed point contact Andreev reflection measurements and data analysis under difficult time constraints. Finally, Professor Charles Fadley and Dr. Alex Grey provided expertise in hard X-ray photoemission spectroscopy.

I gratefully acknowledge financial support from the United States Department of Energy and the Western Institute of Nanoelectronics (WIN).

None of this would have been possible without my parents. You both exemplify the values of hard work, class and integrity. You taught me to believe in myself and to dream big. Then you believed in me, even when I faltered, and supported me unconditionally. I cannot begin to thank you enough. Everything that I have done and will go on to do is because of you. I won the parent lottery. I love you both.

I owe my deepest gratitude to my partner, Carlos, who has had to bear a disproportionate amount of my frustrations, setbacks and mishaps, despite having no understanding of what I was actually talking about. All the while, you provided unwavering support and helped keep things in perspective by reminding me that “if getting a PhD was easy, everyone would do it.” I appreciated your insightful advice, and although it wasn’t always what I wanted to hear, it was always what I needed to hear. I can’t imagine how this would have gone without you; you are my rock. I look forward to what the future holds for us.

Chapter 1: Background and Motivation

The continuing pursuit of Moore's Law has led to logic technologies with not only the expected increase in transistor density but also significant increases in energy consumption and heat generation, making thermal management more difficult with each new generation. To continue pushing computing technology, an alternative must be realized. Semiconductor spintronics, or spin-electronics, has been touted as a potential replacement, where the spin rather than the charge of an electron is utilized. Traditional CMOS devices rely on moving charges by imposing and removing barriers, which inherently require energy.¹ Depending on the design of a spin device, where for instance a spin-selective barrier could be employed, the same energy constraints do not exist, and it has been theoretically shown that these devices are predicted to outperform traditional CMOS devices.^{1,2} Many proposed spintronic devices, including the original spin field effect transistor (spinFET) proposed by Datta and Das, require a spin-polarized material to inject a spin-polarized current into a semiconductor.^{3,4}

One of the most heavily investigated systems in this regard is the canonical dilute magnetic semiconductor, $\text{Ga}_{1-y}\text{Mn}_y\text{As}$ ($y < 0.08$), which offers the potential to make devices with electrically tunable ferromagnetism.^{5,6} Mn, when substituted for Ga in the semiconductor lattice, introduces holes and local magnetic moments due to the partially occupied d-orbitals, leading to carrier mediated ferromagnetism and a very high degree of spin polarization ($> 85\%$).^{5,6,7} However, the system is prone to phase segregation, making incorporation of Mn above $\sim 8\%$ very difficult even with careful control of the growth and annealing conditions.⁶ As a result, the maximum reported Curie temperature (T_c) remains low (~ 150 K), meaning this material is not suitable for room temperature spin-injector applications.⁵

The binary Heusler alloy, Fe_3Si , is a potentially better candidate for a spin injector. This material has a high Curie temperature (> 800 K) and has been theoretically shown to possess high spin-polarization.^{8,9,10,11,12} Additionally, it can be grown epitaxially on many different semiconductor and insulator substrates, offering a wide range of device applications.^{12,13,14,15} Stoichiometric Fe_3Si has the D0_3 crystal structure shown in Figure 1.1 where the unit cell is made up of four fcc Bravais lattices and can be thought of as 8 bcc-like sub-units with Fe (Fe_{II}) on the cube corners and Fe (Fe_{I}) and Si alternating in the body centers.^{13,16} Fe has two unique sites in the lattice; Fe_{II} is surrounded by 4 Fe nearest neighbors (NN) and 4 Si NN, and Fe_{I} is surrounded by 8 Fe NN. The Fe_{I} atoms behave similarly to those of pure Fe, while the properties of the Fe_{II} atoms can be strongly influenced by the nearest neighbor species.¹⁶

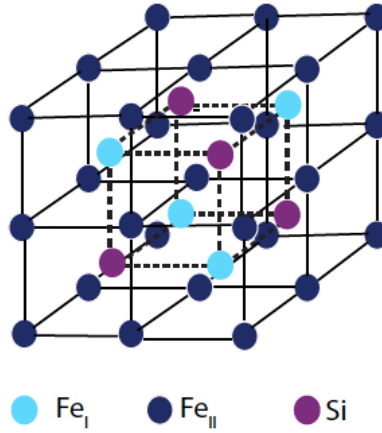


Figure 1.1 Fe_3Si crystal structure. Fe atoms occupy two non-equivalent sites in the lattice.

Despite the potential of Fe_3Si , the material is not predicted to be fully spin-polarized and can be improved.^{9,10} In transition metals, d-bands are spin-polarized, but unpolarized s-bands also cross the Fermi energy (E_F) and contribute minority carriers to conduction. The transition metal can be alloyed in order to shift these s-bands either above or below E_F so that only polarized d-bands remain. The situation is indeed more complex in real materials due to orbital hybridization, but this is the general framework.¹⁷ We suggest that increasing the Si concentration by investigating the range $0.43 < x < 0.75$ for $\text{Fe}_x\text{Si}_{1-x}$ could lead to increased spin-polarization. Higher Si concentration will lead to a reduction in carrier concentration, which should favor sharper energy bands, and thus a large density of states. Based on the Stoner criterion, a large density of states will tend to favor spin splitting.¹⁸ Furthermore, in this composition range thin film growth techniques can be used to fabricate metastable bcc-like epitaxial and amorphous films, where chemical and structural order can tune the magnetic and electronic properties.

This work will investigate the effect of chemical and structural order on the magnetic and electronic properties of amorphous and epitaxial $\text{Fe}_x\text{Si}_{1-x}$ thin films in the composition range $0.43 < x < 0.75$. This range was investigated because the Si concentration can be increased compared to Fe_3Si while still maintaining ferromagnetism in the system. Figure 1.2 shows a portion of the equilibrium phase diagram for the binary Fe-Si system, and the proposed range lies mostly in a two-phase phase field.¹⁹ Thin film growth techniques were used to fabricate metastable bcc-like epitaxial and amorphous films. The Fe-rich portion of the phase diagram shows varying amounts of chemical order (D0_3 , B2 , A2) depending on composition and temperature, and these different degrees of chemical order might be expected in the metastable bcc-like films as well. The stoichiometric ordered structures are $x=0.75$ D0_3 (discussed above) and $x=0.50$ B2 (CsCl), with Fe at the cube corners surrounded by Si in the body centers. When the composition is off stoichiometry, in the chemically ordered D0_3 structure, additional Si (Fe) substitutes onto Fe_I (Si) lattice sites (figure 1.3a). Partial ordering occurs in the B2 (CsCl) crystal structure, where Fe is ordered at the cube corners, but Fe and Si randomly

occupy the body center sites (figure 1.3b). In the A2 crystal structure, there is no long-range chemical ordering, but structural order is maintained.

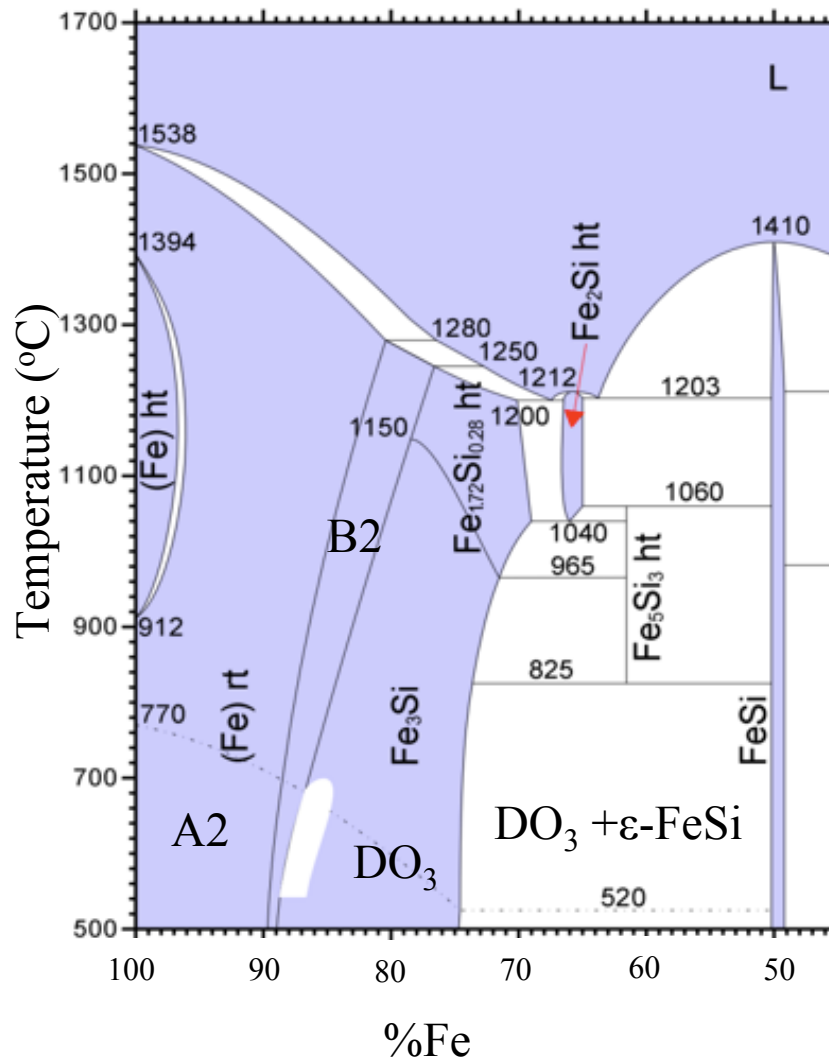


Figure 1.2. Partial Fe-Si binary phase diagram.¹⁹

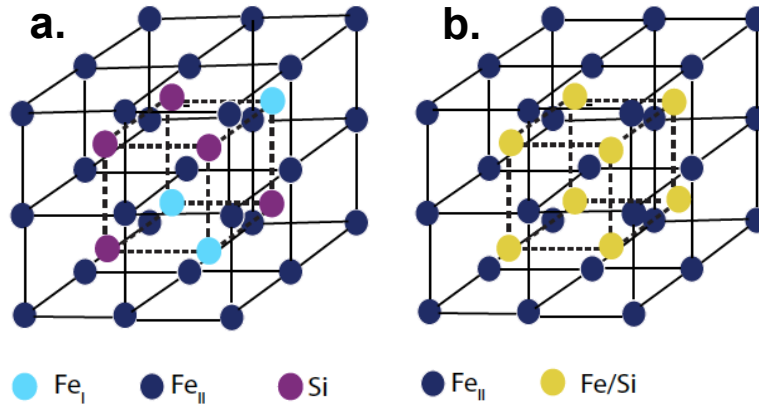


Figure 1.3 Off-stoichiometry ($x < 0.75$) (a) D0₃ and (b) B2 structures.

In the amorphous films, the local structure can also change as a function of composition. Local atomic structures in amorphous solids are generally determined by the bond type. In semiconductors with covalent bonding, the structure is typically referred to as a continuous random network (CRN), where each atom has a few (2-4) directional bonds.²⁰ On the other hand, amorphous metals typically form random dense-packed structures with coordination numbers between 8-12 due to the non-directionality of their bonds.²⁰ The structure of an amorphous alloy of Fe and Si might be expected to vary from CRN for the Si-rich compositions to a dense-packed structure on the Fe-rich side.²¹

Chapter 2 will discuss thin film growth and characterization techniques, and Chapter 3 will investigate how different degrees of chemical order can be used to tune the magnetic and electronic properties in epitaxial Fe_xSi_{1-x} thin films. Previous experimental work on bulk Fe_xSi_{1-x} alloys (for x near 0.75) has shown the magnetic properties are strongly dependent on Fe concentration and chemical order.^{16,22} Additionally, theoretical studies show that the density of states can be tuned by varying the Fe concentration or by doping with small amounts of V, Mn or Cr.^{9,23} Most of this prior work has focused primarily on the chemically ordered endpoints of the Fe_xSi_{1-x} composition range, however. In this chapter, Fe_xSi_{1-x} epitaxial thin films with different chemical order have been fabricated and investigated across a wide composition range, $0.55 < x < 0.77$. Using conversion electron Mössbauer spectroscopy (CEMS) results, this chapter will show that the films have B2 chemical order for $x \leq 0.65$ and D0₃ for $x > 0.65$. Even very far from the equilibrium composition, $x = 0.75$, the films still tended towards chemical order; the A2 structure was not successfully fabricated. The theoretically calculated magnetic moments for the B2 and D0₃ structures are not significantly different but are both reduced from the A2 moment due to less Fe-Fe pairs. Finally, this chapter will also show that additional features observed in the experimental and theoretical X-ray absorption spectra are due to Fe-Si hybridization.

Chapter 4 will probe the local atomic structure and magnetism in *amorphous* Fe_xSi_{1-x} thin films. The nature of magnetism in amorphous solids is strongly dependent on the local environments. Under the assumption the direct exchange interaction is isotropic, it

depends only on the distance between interacting atoms.²⁰ In amorphous materials, each lattice site is different with respect to nearest neighbor distances and coordination numbers, leading to the potential for both positive and negative exchange interactions.²⁰ Pure amorphous Fe has been prepared by quench-condensing and found to have mostly positive exchange interactions (ferromagnetic), however it exhibits a decreased magnetic moment compared to crystalline bcc Fe.^{24,25} This reduction was attributed to the presence of some negative exchange interactions (similar to γ -Fe). If the exchange interaction is equally likely to be positive or negative, the system is often termed “frustrated” or a spin glass. Many amorphous $\text{Fe}_y\text{Z}_{1-y}$ alloys (Z=Nb, Ta, Y, Zr, Lu) are ferromagnetic as y approaches 1 but exhibit spin glass behavior with decreasing y .^{26,27,28,29,30} This chapter will show that amorphous $\text{Fe}_x\text{Si}_{1-x}$ thin films have a striking enhancement in magnetization (both spin and orbital) and spin polarization compared to crystalline films with the same composition ($0.45 < x < 0.75$); density functional theory (DFT) calculations also show this enhanced magnetization. X-ray absorption fine structure (XAFS) results and theoretical DFT calculations of the local structural ordering are presented to explain the origin of the enhanced magnetization.

In Chapter 5, hard X-ray photoemission spectroscopy (HAXPES) is used to experimentally investigate the differences in the electronic properties as a function of composition and structure. X-ray photoelectron spectroscopy (XPS) has been used extensively to study the chemical and electronic properties of Heusler alloys.^{31,32,33} However, due to the low inelastic mean-free path (IMFP) of the photoemitted electrons, conventional XPS measurements are inherently surface-sensitive. By performing photoemission measurements in the hard x-ray regime, the measurement probes 4-7 times deeper, providing truly bulk information.^{34,35} This chapter will show the electronic structure can be tuned by variations in composition and structural order, and the environment around Si is remarkably well ordered in the amorphous state, consistent with findings in Chapter 4.

Chapter 6 will discuss electronic transport, magnetotransport and the anomalous Hall effect (AHE) in amorphous and crystalline $\text{Fe}_x\text{Si}_{1-x}$ thin films. Electrical resistivity in metals is given by the following equation

$$\rho = \frac{m}{ne^2\tau} \quad (1.1)$$

where m is the mass of the charge carrier, n is the number of charge carriers, e is the charge and τ is the collision time (carrier lifetime). τ is related to the mean free path, l , and the velocity at the Fermi surface (v_F) through $\tau = l/v_F$. Typically for a given crystalline metal, the parameter that varies as a function of temperature is τ . The electrical resistivity decreases as the temperature is reduced from room temperature, where τ is dominated by phonons, to low temperature, where τ is dependent on impurities, chemical or structural, in the crystal.³⁶ This behavior is defined as a positive coefficient of resistivity, α . Here α is defined in $\rho_l = \rho_{\text{ref}}[1 + \alpha(T_l - T_{\text{ref}})]$ where ρ_l and ρ_{ref} are the resistivities at $T_l = 10$ K and $T_{\text{ref}} = 300$ K (for example). In an amorphous metal, however, the electrical resistivity is essentially temperature independent. Structural

disorder leads to a mean free path on the order of the interatomic spacing, meaning a constant l . α is small but can be either positive or negative and includes the temperature dependence of n and more complex phenomena like weak localization and electron correlation effects.³⁷ Upon comparison between different amorphous metals and metal alloys, n is the parameter that typically varies. It has been shown that a linear correlation exists between the electrical resistivity (essentially n) and α , as shown in Figure 1.4.³⁸ The resistivity where the crossover between positive and negative α occurs is typically between 50-250 $\mu\Omega\text{cm}$.³⁹

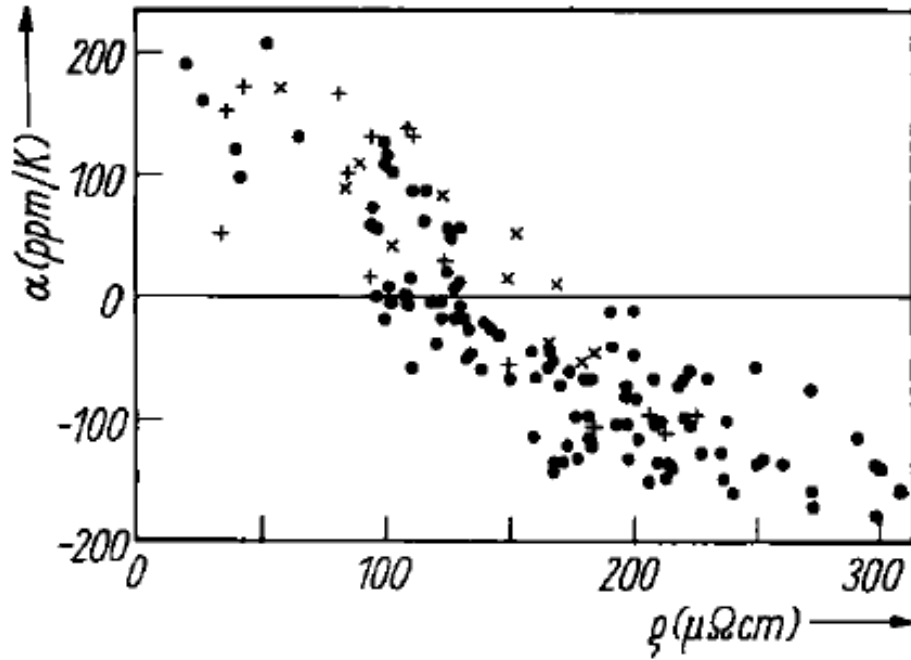


Figure 1.4. Temperature coefficient of resistivity, α , versus resistivity for bulk alloys (+), thin films (•) and amorphous alloys (x). Figure and caption from ref [38]

Intrinsic magnetoresistance (MR) can have many origins; some phenomena, although not all, specifically occurring in ferromagnetic materials are discussed here. MR, $\Delta\rho_{xx}$, is defined by the following equation:

$$\Delta\rho_{xx} = \rho_{xx}(H) - \rho_{xx}(0) \quad (1.2)$$

$\rho_{xx}(H)$ is the longitudinal resistivity at some applied magnetic field, and $\rho_{xx}(0)$ is the longitudinal resistivity at zero field. Ordinary MR, occurring in all metals, is positive and due to the cyclotron motion of electrons in an applied magnetic field.^{18,40} In ferromagnetic metals, anisotropic magnetoresistance (AMR) is common and dependent on the orientation between the magnetization and the current direction. AMR can be positive or negative and is a consequence of anisotropic carrier scattering due to the spin-orbit interaction.^{40,41} Additionally, negative MR in ferromagnetic metals can occur by

carrier scattering from localized magnetic moments, disordered spins (particularly near the magnetic transition temperature) or magnetic domain walls.^{18,42}

The Hall effect in ferromagnetic materials has two contributions, one from the ordinary Hall effect (OHE) due to the Lorentz force, which is proportional to the applied magnetic field and one from the anomalous Hall effect (AHE) due to asymmetric scattering, which is proportional to the perpendicular component of the magnetization. The equation describing this effect takes the form:

$$\rho_{xy}(total) = \rho(OHE) + \rho(AHE) = R_0 H + R_s M_z \quad (1.3)$$

Here, R_0 is the ordinary Hall coefficient ($R_0 = \pm 1/ne$), and R_s is the anomalous Hall coefficient. H and M_z are the magnetic field and the magnetization perpendicular to the layer, respectively.

The origin of the Anomalous Hall effect (AHE) in ferromagnetic materials remains controversial, but recently a unified theory has been proposed.^{43,44} The theory generally splits the anomalous Hall conductivity ($\sigma_{xy} = \rho_{xy}(AHE)/\rho_{xx}^2 + \rho_{xy}^2 \sim \rho_{xy}(AHE)/\rho_{xx}^2$) into three regions based on the longitudinal conductivity (σ_{xx}). In the clean limit ($\sigma_{xx} > 10^6 \Omega^{-1} \text{cm}^{-1}$) at low temperatures, the skew-scattering mechanism, which is due to asymmetric spin scattering from impurities with spin-orbit coupling, dominates, and $\sigma_{xy} \propto \sigma_{xx}$.^{44,45,46,47} In the second regime ($10^4 \Omega^{-1} \text{cm}^{-1} < \sigma_{xx} < 10^6 \Omega^{-1} \text{cm}^{-1}$), the intrinsic mechanism is the dominant contribution to σ_{xy} . The intrinsic contribution is attributed to interband spin-orbit coupling that causes a gap to open at band anti-crossing points in the electronic band structure. If the Fermi energy lies near these points, a large Berry phase curvature will occur, thus significantly enhancing σ_{xy} .^{44,48} In this regime, $\sigma_{xy} = \text{constant}$. Although it may be counterintuitive that the skew-scattering mechanism dominates in a σ_{xx} range with fewer impurities and the intrinsic contribution dominates in a regime with more, the intrinsic contribution is actually independent of the carrier lifetime, τ , while the skew-scattering mechanism is not. So skew-scattering will always dominate when τ is large, as in the clean limit. Numerous experimental results have verified the dependences of the anomalous Hall conductivity in these two regimes for Fe, Co, Ni, and Gd.^{49,50,51} The low conductivity regime ($\sigma_{xx} < 10^4 \Omega^{-1} \text{cm}^{-1}$, $\rho_{xx} > 100 \mu\Omega \text{cm}$) is less well understood. Experimental results from ultrathin Fe,⁵² chalcogenide-spinel structures ($\text{Cu}_{1-x}\text{Zn}_x\text{Cr}_2\text{Se}_4$),⁵⁰ Fe_3O_4 and $\text{Fe}_{3-x}\text{Zn}_x\text{O}_4$ ⁴⁷ show $\sigma_{xy} \propto \sigma_{xx}^n$ where $1.6 < n < 1.8$. These data have been obtained by varying the film thickness, measurement temperature or impurity concentration. It has been suggested that the observed behavior is due to a gradual decrease in the intrinsic effect due to disorder, however there is no theory to support this scaling.⁴⁴ Conventionally, σ_{xy} is plotted against σ_{xx} , however the carrier concentration seems the more relevant parameter in this regime.

Although there seems to be good agreement between these experimental results, this work suggests that the behavior in [43] is not universal. In this chapter, a different scaling is shown in the low σ_{xx} regime by studying the AHE and M at 2 K in a series of

amorphous and epitaxial $\text{Fe}_x\text{Si}_{1-x}$ thin films ($0.45 < x < 0.71$), where the hole carrier concentration (n_h) is varied. The scaling roughly depends on n_h , and the results are compared to a $\text{Ga}_{1-y}\text{Mn}_y\text{As}$ study, which reported a similar dependence on charge carriers. The AHE scaling in these material systems was then compared to other materials in the low conductivity regime, and all were found to be approximately linearly dependent on the longitudinal conductivity, suggesting dependence on the number of carriers.

Chapter 2: Thin Film Growth and Characterization

2.1 Thin Film Deposition

$\text{Fe}_x\text{Si}_{1-x}$ ($0.43 < x < 0.77$) thin films (1000-2000 Å) were grown by electron beam co-evaporation of Fe and Si at a base pressure between 1.0×10^{-8} and 1.0×10^{-9} torr. Each source was a Cu crucible containing pure elemental material. Si has a negative coefficient of thermal expansion, so the heating and cooling rates of the source were carefully controlled. If the source cooled too quickly, it necessitated heating *extremely* slowly before the next deposition to prevent it from exploding. For Fe, the rate at which the source was heated and cooled was less critical. The deposition rate for each source was monitored individually with quartz crystal microbalances, and a constant deposition rate was maintained by means of a PID feedback loop. The desired composition was obtained by varying the individual deposition rates.

Deposition temperatures and substrates were varied to obtain desired film structures. Amorphous films were grown at room temperature on amorphous SiN_x on Si substrates. Epitaxial $\text{Fe}_x\text{Si}_{1-x}$ thin films were obtained by deposition on (001) MgO at 200-300°C for $x > 0.65$. For samples with compositions $x \leq 0.65$, a Cr layer, deposited at 200°C on (001) MgO prior to film growth was necessary to obtain epitaxy. A similar process was used by Walterfang *et. al.*¹⁵ SrTiO_3 (001) substrates were also tested for $x < 0.65$, however epitaxy was not realized. Further details of lattice constants, epitaxial relationships and x-ray diffraction will be discussed in the following section.

Depending on the measurement technique, some films were capped with 15-20 Å of Al, which oxidized and prevented film oxidation. X-ray absorption fine structure (XAFS) and X-ray magnetic circular dichroism (XMCD) require capped samples in order to probe only metallic Fe. Hard X-ray photoemission spectroscopy (HAXPES), on the other hand, is best performed with uncapped samples because non-oxidized Al will convolute the valance band spectra. For the other measurement techniques discussed, capping the samples had no bearing on the data quality.

2.2 X-ray Diffraction

Figure 2.1(a) is a representative θ - 2θ scan from two epitaxial $\text{Fe}_x\text{Si}_{1-x}$ thin films, $x=0.72$ and 0.67. The superlattice (*i.e.* 200 D0₃ and 100 B2) and fundamental (*i.e.* 400 D0₃ and 200 B2) reflections referenced to the A2 structure are present as indicated in the figure. No other peaks were present in the scan, indicating a single out of plane orientation in the film. In order to confirm epitaxy, azimuthal (ϕ) scans were performed on the off-axis 110 (B2) or 220 (D0₃) peak. Fig. 2.1(b) shows the ϕ scans from these films; four-fold symmetry was observed, confirming an epitaxial film in both cases. Similar θ - 2θ and ϕ scans were obtained for all epitaxial $\text{Fe}_x\text{Si}_{1-x}$ thin films. The films are oriented [100] out-of-plane and rotated 45° in plane with respect to the MgO substrate, *i.e.* $\text{Fe}_{1-x}\text{Si}_x$ [100] || MgO [110].

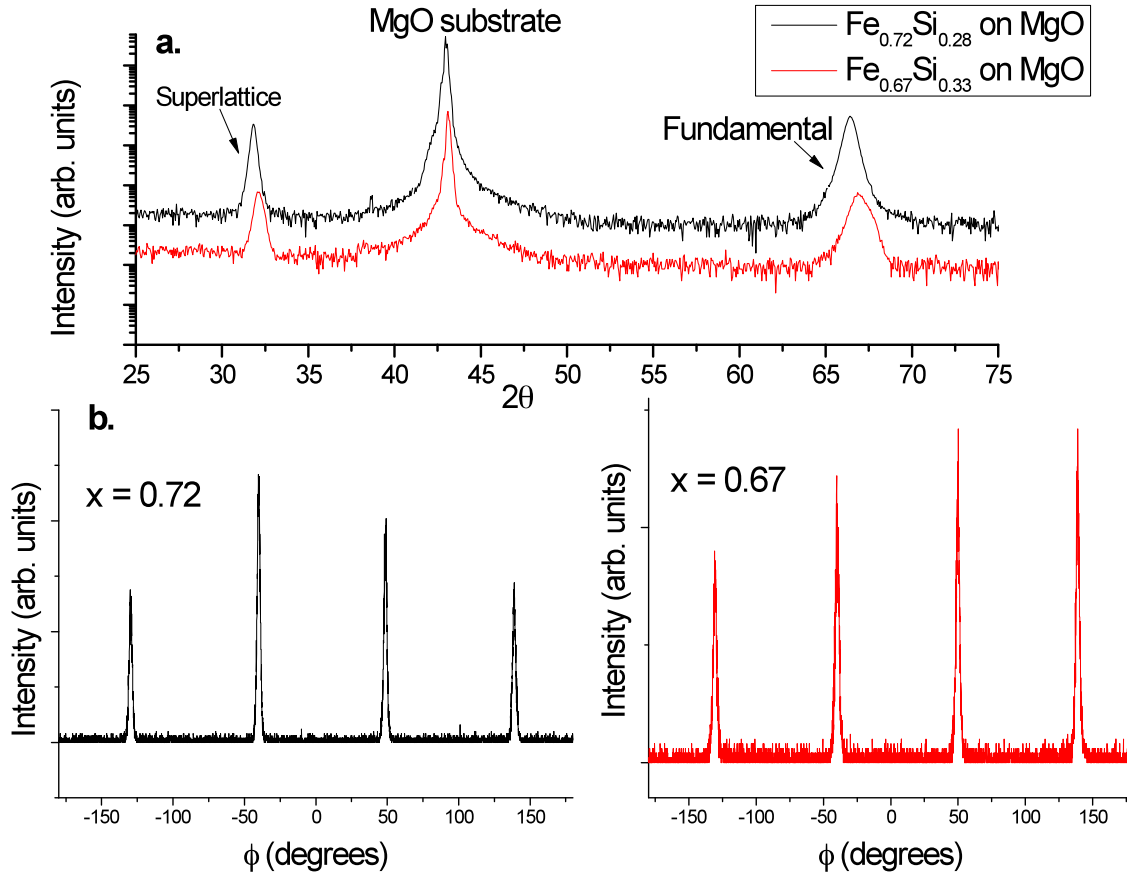


Figure 2.1. Representative X-ray diffraction patterns. **(a)** θ - 2θ scans for $x=0.72$ (black) and $x=0.67$ (red) epitaxial films. **(b)** ϕ scans on in-plane 220 peak for $x=0.72$ (black) and 110 peak for $x=0.67$ (red)

From the location of the superlattice peak, the lattice constant was calculated using Bragg's Law:⁵³

$$\lambda = 2d_{hkl} \sin \theta \quad (2.1)$$

$$\text{where } d_{hkl} = \frac{a_0}{\sqrt{h^2 + k^2 + l^2}} \quad (2.2)$$

Measurements were performed with Cu K α radiation, hence $\lambda = 1.5418 \text{ \AA}$. Figure 2.2 shows the lattice constants calculated with equations 2.1 and 2.2 as a function of Fe concentration. This linear variation in lattice constant as a function of Fe concentration is a strong indication of chemical homogeneity in the samples, with no evidence of secondary phase formation. As indicated in the figure, films with the B2 and D0₃ crystal structure possess lattice constants that differ by a factor of 2, since the D0₃ unit cell is double the size of the B2 (CsCl) unit cell. Further details of the chemical order will be discussed later.

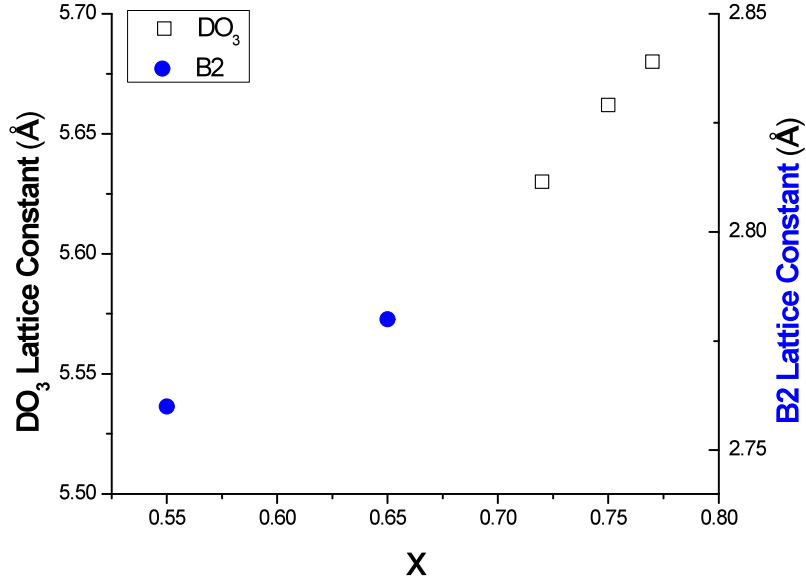


Figure 2.2. Out of plane lattice constants for $\text{Fe}_x\text{Si}_{1-x}$ epitaxial films calculated from the X-ray diffraction superlattice peak.

An approximation of the chemical coherence length, t , can be calculated using the Scherrer formula:⁵³

$$t = \frac{0.9\lambda}{B \cos \theta_B} \quad (2.3)$$

where λ is as defined in equation 2.1, B is the full width at half max (FWHM) of the superlattice peak, and θ_B is the location of the superlattice peak. Table 2.1 gives the result of this calculation for the epitaxial $\text{Fe}_x\text{Si}_{1-x}$ thin films. The length scale over which chemical coherence is maintained is on the order of 200-300 Å, indicating good chemical order in the films. A calculation of the bcc coherence length from the fundamental peak was not accurate; the diffractometer used in these measurements exhibits a half angle substrate peak at the same location as the fundamental film peak, leading to peak broadening.

Concentration	Structure	Chemical Coherence Length (Å)
0.77	D0 ₃	205
0.75	D0 ₃	225
0.72	D0 ₃	296
0.67	B2	176
0.65	B2	265
0.55	B2	229

Table 2.1 Chemical coherence length for epitaxial Fe_xSi_{1-x} thin films

The 100 reflection in bcc Fe is forbidden by structure factor.⁵³ However, this superlattice peak is observed in all epitaxial Fe_xSi_{1-x} thin films, indicating either B2 or D0₃ order. From these reflections, it is not possible to distinguish between these two types of order because for a given composition the intensity and location of the superlattice peak are the same for both structures. Scattering from the (111) planes will lead to a diffraction condition for the D0₃ structure but not the B2 structure.

An estimation of the chemical order is obtained by calculating the intensity ratio of the superlattice to fundamental peaks. Diffraction is strongest in the forward scattered direction ($\theta = 0^\circ$), and the intensity drops off precipitously as θ increases. This fact must be considered when comparing peak intensities at different θ values. The chemical order calculation was performed by taking the ratio of $|F|^2$ values for each peak, where $|F|^2$ is calculated using the following approximation:⁵³

$$I = |F|^2 p \left(\frac{1 + \cos^2 2\theta}{\sin^2 \theta \cos \theta} \right) \quad (2.4)$$

Here, I is the integrated intensity, and p is the multiplicity factor. In this case, p is taken to be unity since only 100 reflections from an epitaxial film are being compared. For comparison, ratios for perfect chemical order can be obtained from the following approximation:

$$\frac{I_s}{I_f} \approx \frac{|F_s|^2}{|F_f|^2} = \frac{(f_{Fe} - f_{Si})^2}{(f_{Fe} + f_{Si})^2} \quad (2.5)$$

where f_{Fe} and f_{Si} are the atomic scattering factors for Fe and Si, respectively. This equation only applies for $x=0.5$ and becomes the following for $x>0.50$:

$$\frac{I_s}{I_f} \approx \frac{|F_s|^2}{|F_f|^2} = \frac{(f_{Fe} - f_{avg})^2}{(f_{Fe} + f_{avg})^2} \quad (2.6)$$

$$\text{where } f_{avg} = \left(\frac{x - 50}{50} \right) f_{Fe} + \left(\frac{1 - x}{50} \right) f_{Si} \quad (2.7)$$

Atomic scattering factors were obtained from ref [54]. The results of these calculations are presented in figure 2.3. The ratio decreases as the Fe concentration increases, as

expected since at $x=1.0$ the reflection is forbidden. The experimental intensity ratios are close to the calculated values for perfect order, indicating epitaxial films with good chemical order.

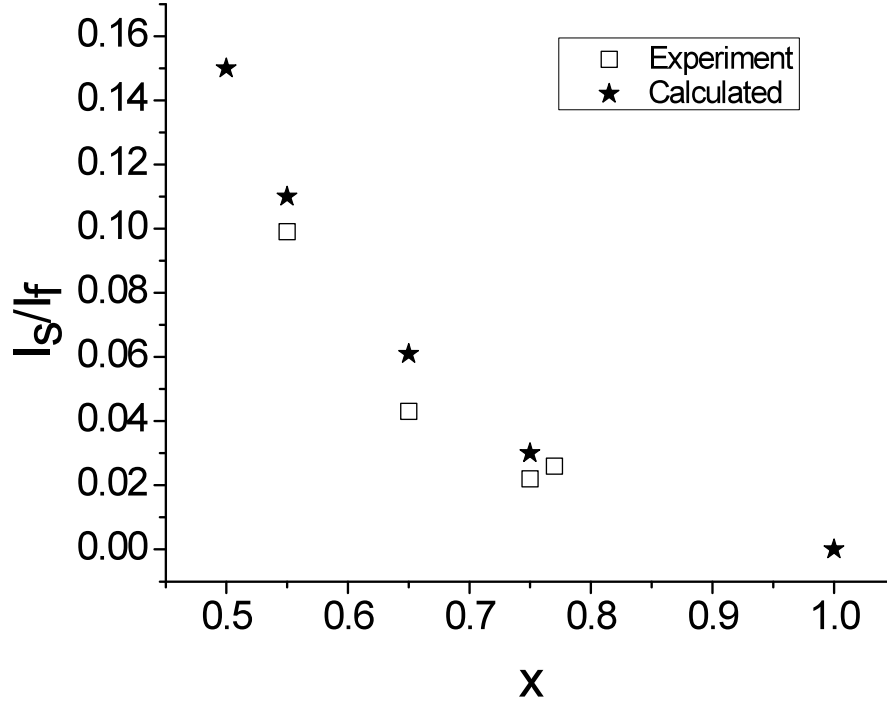


Figure 2.3. Calculated and experimental ratio of superlattice to fundamental X-ray diffraction peak for epitaxial $\text{Fe}_x\text{Si}_{1-x}$ thin films.

Figure 2.4 shows representative θ - 2θ scans from two amorphous samples, $x=0.55$ and $x=0.60$. In bcc materials, $[110]$ is the low energy out of plane growth direction because it maximizes in-plane bonds. As such, 110 diffraction peaks should be expected if an epitaxial relationship does not exist with the substrate. In all amorphous samples with $x < 0.71$, no film peaks were observed. For $x > 0.71$, peaks corresponding to the 220 reflection were present, meaning the films were polycrystalline. Polycrystalline films were not significantly investigated in this work. The lack of film peaks in X-ray diffraction for samples with $x < 0.71$ does not confirm the sample is fully amorphous, however. Grain size is inversely proportional to the FWHM of a diffraction peak (equation 2.3), so nanocrystalline grains will sufficiently broaden the peak rendering it indistinguishable from the background. In order to confirm the samples were amorphous, transmission electron microscopy (TEM) was performed, and the results will be discussed in the next section.

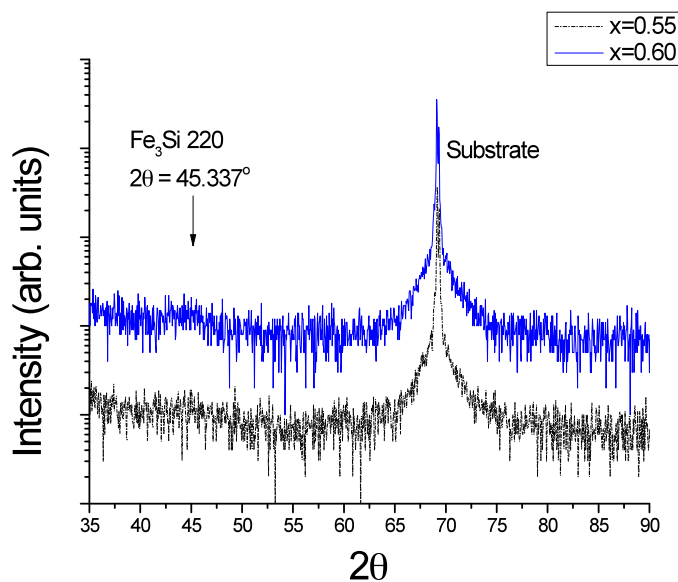


Figure 2.4. θ - 2θ X-ray diffraction scan from two amorphous $\text{Fe}_x\text{Si}_{1-x}$ thin films, $x=0.55$ and $x=0.60$.

SrTiO_3 (STO) (001) substrates were investigated as a means to obtain epitaxy in low Fe concentration films ($x \leq 0.65$) without the aid of a Cr seed layer, however this work was not successful. The distance between atoms in the [110] direction is 2.76 \AA in STO, which corresponds well to the lattice constant for $x=0.55$ (2.76 \AA). However, samples grown at temperatures at or below $175 \text{ }^\circ\text{C}$ produced amorphous films, and above this temperature the films exhibited the high temperature Fe_5Si_3 phase, as indicated in the phase diagram in figure 1.2.

2.3 Transmission Electron Microscopy

Cross-section transmission electron microscopy (TEM) was performed on $\text{Fe}_x\text{Si}_{1-x}$ samples ($x=0.55$ and 0.67) grown at room temperature on $a\text{-SiN}_x$ on Si. These samples did not exhibit any peaks in X-ray diffraction. Figure 2.5 shows a TEM image from $x=0.67$, which displays a predominantly amorphous structure with some nanocrystals on the order of 5 nm in size embedded in it. The electron diffraction pattern (inset) displays sharp diffraction spots from the Si substrate and a broad diffraction ring with some weak spots, further indicating partial crystallinity. The volume fraction of the amorphous matrix is estimated from these images to be on the order of 80% , with $\sim 20\%$ representing nanocrystalline areas. Samples with $x > 0.67$ are considered partially crystalline, based on these results. Figure 2.6 is a high-resolution (HR) cross-sectional TEM image from the $x=0.55$ amorphous sample which displays no clear nanocrystallinity. In a few places, (diameter $< 2 \text{ nm}$) we observe evidence of poorly defined lattice fringes (indicated in the figure) suggesting nanocrystal precursors increase (in size and number) with increasing Fe concentration.

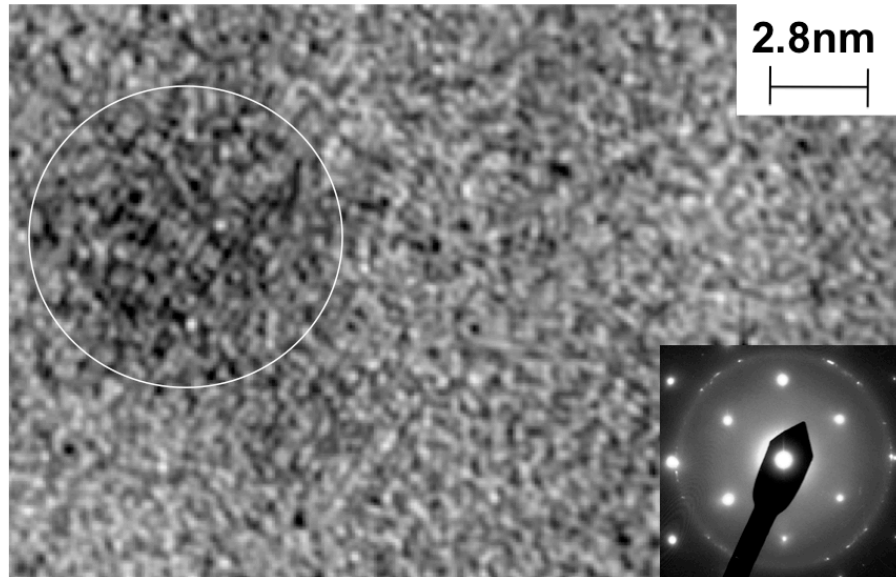


Figure 2.5. TEM image and electron diffraction pattern (inset) for the amorphous film $x=0.67$. The image displays a ~ 5 nm diameter nanocrystal (circled) in an amorphous matrix. In addition to strong spots from the $\langle 110 \rangle$ -oriented Si substrate, the electron diffraction pattern shows a broad diffuse ring originating from the amorphous film, as well as some random spots due to nanocrystals. (Images courtesy of D. Smith)

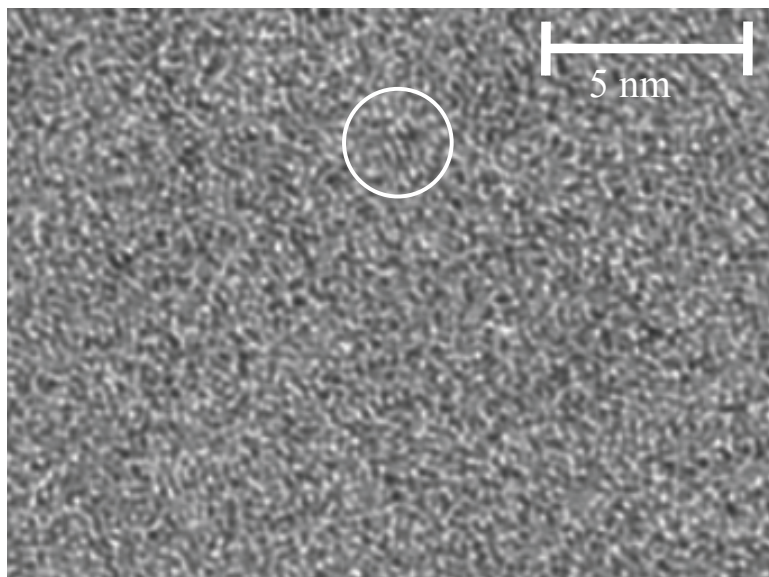


Figure 2.6. TEM image from $x=0.55$ amorphous sample. Poorly formed lattice fringes are highlighted. (Image courtesy of D. Smith)

Cross-section TEM was also performed on an epitaxial $x=0.55$ thin film, and figure 2.7 shows the (a) bright field image and (b) electron diffraction pattern. Lattice fringes are clearly observed in the $[100]$ direction, which correspond to the out of plane direction of

the film. The electron diffraction pattern shows many reflections. The reflections corresponding to the MgO substrate are indexed below the spot in white. As expected, the zone axis is $\langle 010 \rangle$. The reflections from the film are indexed above the spot in purple (unless indicated with an arrow); the zone axis for the film is $\langle 110 \rangle$. Superlattice reflections (*i.e.* 001 and 111) are observed, indicating additional ordering beyond the A2 structure. The nature of this chemical ordering will be discussed in Chapter 3. These results show the orientation between the film and the substrate is $\text{Fe}_{0.55}\text{Si}_{0.45} [100] \parallel \text{MgO} [110]$. All of these results are consistent with XRD measurements on this sample.

In the top left corner of the bright field image, there is a small region where the lattice fringes appear oriented in a different direction, although fringes along the $[100]$ direction can still be distinguished. A Fourier transform of the image from this region reveals spots similar to those circled in yellow on the electron diffraction pattern. Possible origins of these spots will also be discussed in Chapter 3.

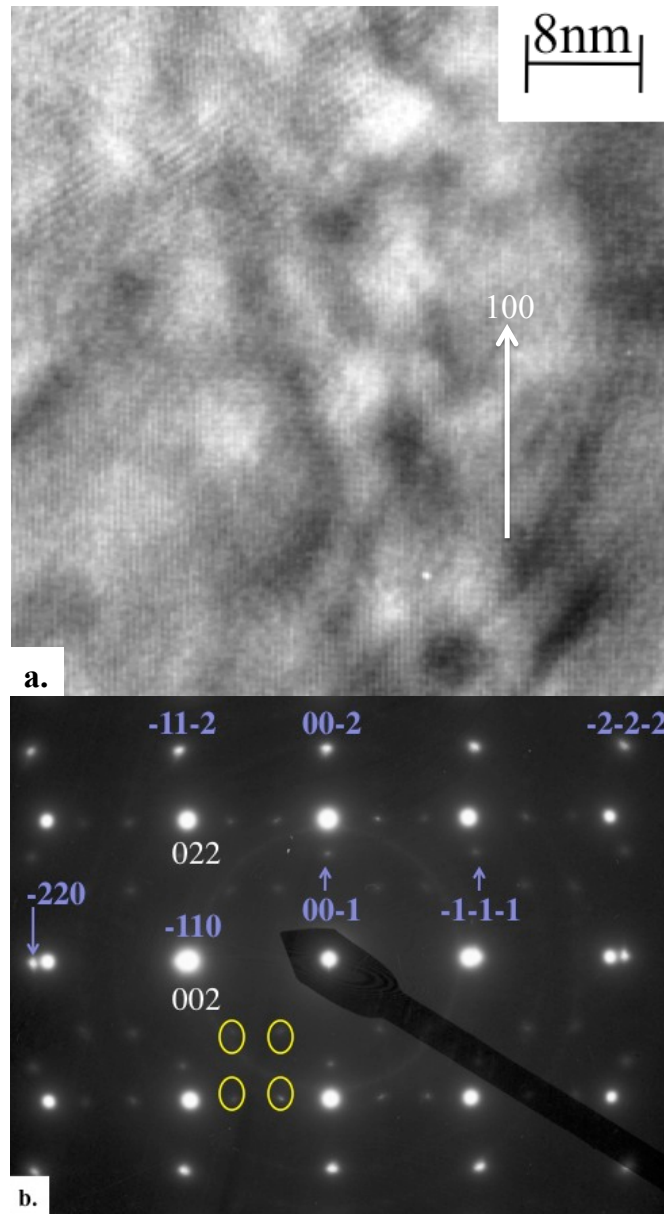


Figure 2.7. (a) Bright field TEM image and **(b)** electron diffraction pattern from an epitaxial $x=0.55$ thin film. The arrow in **(a)** indicates the $[100]$ direction. $\sim 10\%$ of the sample is not oriented in the $[100]$ direction (top left corner of bright field image). In **(b)**, the reflections corresponding to the MgO substrate are indexed *below* the spot in white.

The MgO zone axis is $\langle 100 \rangle$. The reflections from the film are indexed to the B2 structure *above* the spot in purple (unless indicated with an arrow); arrows were used when the spots were faint or too close to other spots. The zone axis for the film is $\langle 110 \rangle$. Note that the 002 MgO substrate reflection and the -110 film reflection are the same spot.

Superlattice reflections (*i.e.* 001 and 111) for the film are also indicated. The yellow circles correspond to diffraction spots from the top left corner of the bright field image.

(Image courtesy of D. Smith)

2.4 Rutherford Backscattering Spectrometry

In Rutherford backscattering spectrometry (RBS), α -particles (He^{2+}) at 3 MeV hit the sample and are backscattered. The energy of these backscattered particles is dependent on the masses of the atoms in the sample. High Z atoms backscatter particles with only slightly less energy than their initial energy, and the backscattered energy decreases with decreasing Z. This technique was used to determine film composition and areal density (atoms/cm^2) by fitting the experimental spectra using the program SIMNRA. Since the thickness of the samples is known, the total number density (atoms/cm^3) can be calculated. Figure 2.8 is an example of the experimental spectra and the fit.

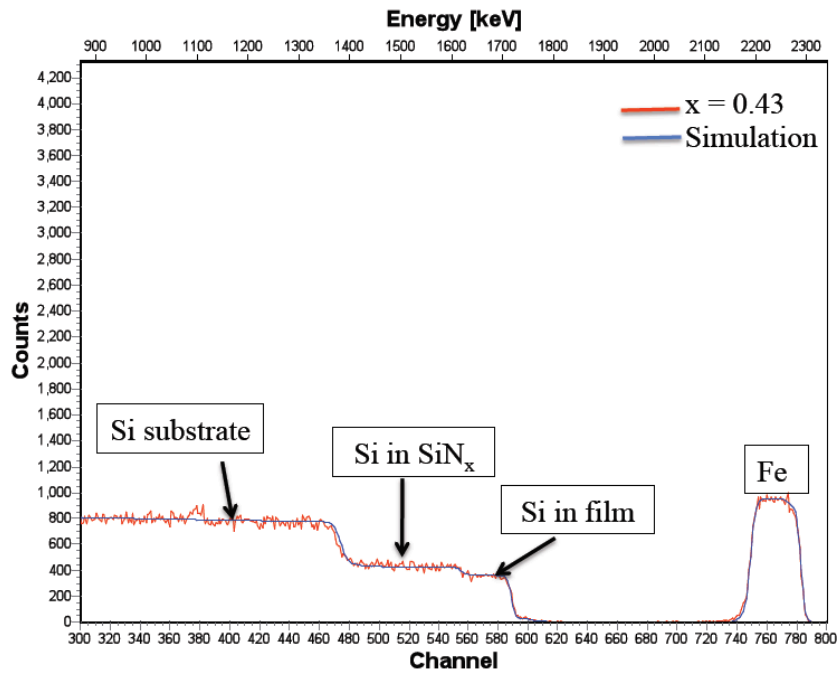


Figure 2.8. Experimental RBS data and fit for an amorphous $x=0.43$ film on SiN_x on Si

2.5 Electronic Transport and Hall Effect

Hall bars for resistivity, magnetoresistance and Hall effect measurements were patterned using standard photolithography and wet etch techniques. $\text{Fe}_x\text{Si}_{1-x}$ alloys were etched in a dilute mixture of hydrofluoric and nitric acid (400mL H_2O : 2mL HNO_3 : 1mL HF). Etch rates were compositionally dependent; faster rates were achieved as x increased. After patterning, the Hall bar was also used to determine film thickness using an Alpha-Step IQ profilometer. 6 measurements were taken and averaged for each sample. The variation between the measurements, which for magnetic and resistivity measurements represents the largest error, was typically 2-5% and often as low as 1%.

Four-point probe dc-resistivity measurements as a function of temperature were performed in a closed cycle refrigerator. Contacts were made to the sample using pressed

indium, and the sample was clamped to the Cu sample holder to ensure a good thermal link.

An image of the Hall device with a schematic of the measurement setup for the magnetoresistance and Hall measurements is shown in figure 2.9. Different orientations of the magnetic field with respect to device are labeled as (a), (b) and (c). Configuration (a) was used for both Hall effect and magnetoresistance measurements, and configurations (b) and (c) were only for MR investigations. Measurements were performed in a Quantum Design SQUID magnetometer at temperatures from 2-300 K in fields of ± 6 Tesla, and contacts to the sample were made with pressed indium. AC measurements were performed at a frequency of 16Hz with a current kept at or below 2 μA to prevent joule heating. A large (0.5 M Ω) reference resistance was used in series with the sample to ensure little to no voltage drop across the sample itself. The measured Hall voltage, $V_{xy,measured}(H)$, and magnetovoltage, $V_{xx,measured}(H)$, were detected with lock-in amplifiers.

Small misalignments in the contacts can produce $V_{xx,measured}$ components in $V_{xy,measured}$. However, V_{xx} is symmetric with H , and V_{xy} is antisymmetric so, the Hall voltage and magnetovoltage can be determined using:

$$V_{xy}(H) = \frac{V_{xy,measured}(H) - V_{xy,measured}(-H)}{2} \text{ and } V_{xx}(H) = \frac{V_{xx,measured}(H) + V_{xx,measured}(-H)}{2} \quad (2.8, 2.9)$$

respectively.⁵⁵ The Hall resistivity (in units of Ωcm) is then calculated using:

$$\rho_{xy}(H) = \frac{E_y}{J_x} \quad (2.10)$$

$$\text{where } E_y = \frac{V_{xy}}{y} \text{ and } J_x = \frac{I}{yt} \quad (2.11, 2.12)$$

I is the current; y is the width of the Hall bar (0.04 cm), and t is the sample thickness.

The magnetoresistance (in units of Ωcm) is calculated using:

$$\rho_{xx}(H) = \frac{V_{xx}yt}{Il} \quad (2.13)$$

where l is the length between the magnetovoltage contacts (0.06 or 0.12 cm).

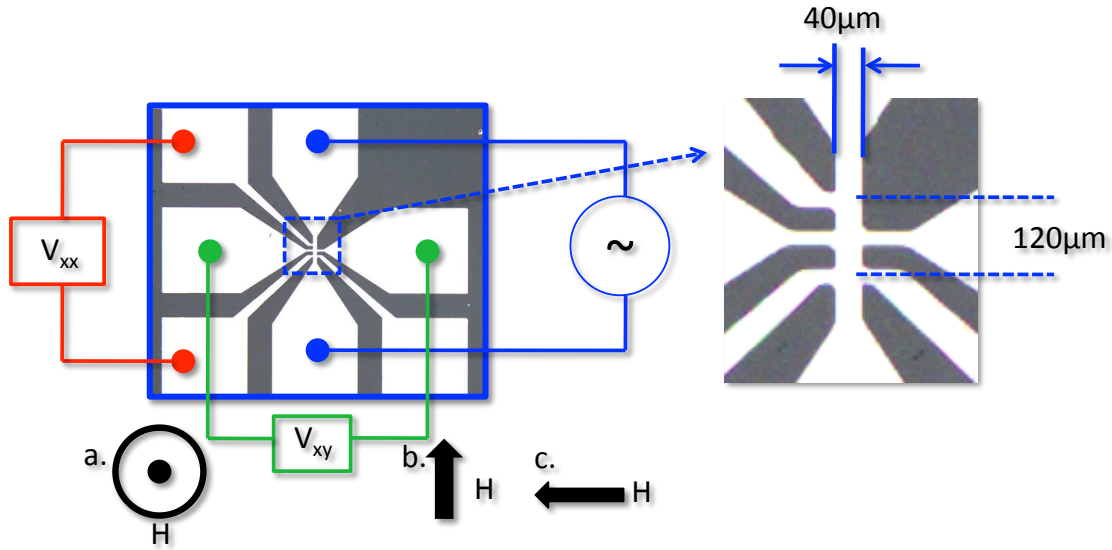


Figure 2.9. Image of hall bar with schematic of experimental setup. Different orientations of the applied magnetic field with respect to the device are shown as (a), (b) and (c). Orientation (a) is used in Hall effect and magnetoresistance measurements, and (b) and (c) are for magnetoresistance measurements.

2.6 Magnetic Characterization

Magnetic measurements were performed in a Quantum Design superconducting quantum interference device (SQUID) magnetometer. Magnetization as a function of applied field was measured at 2K and 300K, and magnetization as a function of temperature (2K-390K) was performed at low fields (less than 1000 Oe). Adobe Photoshop was used to determine the dimensions of the sample, based on a scanned image.

For samples grown on α -SiN_x on Si substrates, a temperature-independent diamagnetic background, determined by fitting the high field slope of the $M(H)$ curve at 300 K, was removed from all $M(H)$ and $M(T)$ data. The diamagnetic background was confirmed the same at 2 K and 300 K and was also independent of whether the sample was measured with the magnetic field in-plane or out-of-plane. For measurements at low fields (<3000 Oe), the diamagnetic background is extremely small, as would be expected. This background was roughly the same for all samples measured; only slight differences were observed due to variations in the thickness of the α -SiN_x layer.

MgO has a low temperature (<10 K) paramagnetic background due to the crystal growth process; the magnitude of this signal varies from substrate batch to substrate batch. At low H , where all of the samples discussed in this work were measured, the signal is linear in H . For each batch, a bare substrate was measured at 2 K, and this signal (normalized by the surface area) was then removed from the sample signal ($M(H)$ and $M(T)$ at $T=2$ K). This method is only reasonable since the paramagnetic background signal from the substrate is small in comparison to the large ferromagnetic signal from the film (2 orders

of magnitude larger for all x). If the ferromagnetic signal from the film is small ($\sim 10^5$ emu) or very large fields (where the paramagnetic background is no longer linear) are needed to saturate the film magnetization, this method is not an appropriate way to remove the paramagnetic background.

Conversion electron Mössbauer spectrometry (CEMS) was performed at room temperature under normal incidence, with a homemade helium-methane gas proportional counter and a ^{57}Co in a Rhodium matrix as the source. Isomer shifts are given with respect to α -iron at 300 K, and the spectra were fitted using the histogram method.^{56,57} In this measurement technique, γ -rays from a moving Co source, where the photon energy is varied by the Doppler effect, impinge on the sample. Fe nuclei in the sample experience a hyperfine magnetic field, which causes a splitting in the nuclear energy levels. Photon absorption occurs at energies corresponding to transitions between these magnetically split levels. In thin films, this absorption is detected by secondary electrons generated when the nucleus decays back to the ground state. The magnetic splitting is dependent on the hyperfine field experienced by the nucleus, making this technique capable of resolving the local Fe environments.

2.7 Synchrotron Techniques

2.7.1 Hard X-ray photoemission spectroscopy (HAXPES)

HAXPES is based on the photoelectric effect, where X-ray photons incident on the sample cause electrons to be ejected. These electrons have a kinetic energy that is equal to the energy of the incident photon less the binding energy, making this technique a very sensitive probe of the binding energies and chemical environments in the sample.

Hard x-ray photoemission measurements were performed at the national synchrotron radiation facility SPring-8 in Japan, using undulator beamline BL15XU. The photon energy set at 5950.3 eV, which is the energy yielding optimal resolution and flux for that particular beamline. The exciting radiation was incident on the sample at a grazing angle of 2.0° as measured from the sample surface plane, and the kinetic energies of the photoemitted electrons were analyzed by a VG Scienta R4000 hemispherical analyzer oriented at an angle of 90° from the direction of the incoming x-rays. The electron takeoff angle as measured with respect to the surface is thus 88° , maximizing bulk sensitivity. Some measurements were also performed at a takeoff angle of 45° to vary the degree of surface vs bulk sensitivity. The measurements were performed at room temperature.

2.7.2 X-ray absorption fine structure (XAFS)

X-ray absorption fine structure measures the modulations in absorption due to the chemical or physical state of an atom.⁵⁸ X-rays incident on a sample promote core electrons to the continuum, and these photoelectrons are backscattered by nearby atoms to the original absorbing atom, thus modulating further X-ray photon absorption. The properties of the backscattered electron are dependent on the distance travelled (bond

length) and the atom it scatters from, making this technique a local probe. Experimental XAFS spectra must be fit to models to extract bond length, coordination number and coordination species.

XAFS was measured at beamline 20-BM-XOR at the Advanced Photon Source (APS) at Argonne National Laboratory (ANL). Room temperature measurements were performed at the Fe K-edge in X-ray fluorescence mode with the electric field of the incoming x-rays oriented perpendicular to the sample plane. A Vortex Si drift detector was used to detect the X-ray fluorescence. The data was fit in R-space using FEFFIT with theoretical scattering amplitudes and phase shifts calculated by FEFF.^{59,60}

2.7.3 X-ray Absorption Spectroscopy (XAS) and X-ray Magnetic Circular Dichroism (XMCD)

In XMCD, circularly polarized light transfers angular momentum to photoelectrons via spin-orbit coupling. In this work, the Fe L-edge is investigated, corresponding to transitions from 2p to 3d states. Since the d-band valance shells have preferred angular momentum directions, the transition probability depends on whether the photon and valance band angular momentum are aligned parallel or anti-parallel. The L₃ (2p_{3/2} → 3d) and L₂ (2p_{1/2} → 3d) edges have opposite spin-orbit coupling (j=l+s, j=l-s, respectively), making the transition probability different for each edge. Additionally, the population of 2p_{3/2} states is 2 times larger than 2p_{1/2}, leading to a larger L₃ intensity.

X-ray absorption spectroscopy (XAS) and X-ray magnetic circular dichroism (XMCD) were performed at room temperature and 79 K in total electron yield (TEY) at the Fe L-edge at beamline 6.3.1 at the Advanced Light Source (ALS), Lawrence Berkeley National Lab, Berkeley CA. The X-rays were incident on the sample at an angle of 30° with respect to the sample surface, and the measurements were performed in total electron yield (TEY) at room temperature. Three scans were taken for each sample, and figure 2.10 shows representative raw data from 3 scans for an x=0.60 amorphous thin film. As indicated in the figure, an energy shift of on the order of 100-200 meV was observed in all measurements. Therefore, the scans on each sample were shifted to the lowest energy (i.e. here scans 1 and 2 were shifted to align to the L₃ peak of scan 3) before averaging. A linear background was fit to the pre-edge and subtracted from the raw spectra; the pre-edge was normalized to zero, and the post edge was set to 1 for each spectra. Each sample was measured in a magnetic field of ±0.5T. I^P and I^{AP} denote the absorption intensity when the photon angular momentum is parallel and antiparallel to the sample magnetization, respectively. The XAS is then defined as $(I^P + I^{AP})/2$, and the XMCD is defined as $I^P - I^{AP}$. The individual orbital and spin moments and the ratio were calculated using.^{61,62}

$$m_{orbital} = \frac{1}{P_{hv} \cos \theta} \frac{2qn_h}{3r}, \quad m_{spin} = \frac{1}{P_{hv} \cos \theta} \frac{(3p - 3q)n_h}{r} \quad (2.14, 2.15)$$

$$\text{and } \frac{m_{\text{orbital}}}{m_{\text{spin}}} = \frac{2q}{9p - 6q} \quad (2.16)$$

where

$$p = \int_{L_3} (I^P - I^{AP}) dE, \quad q = \int_{L_3+L_2} (I^P + I^{AP}) dE \quad (2.17, 2.18)$$

$$\text{and } r = \int_{L_3+L_2} \left(\frac{I^P - I^{AP}}{2} - S(E) \right) dE \quad (2.19)$$

$P_{h\nu}$ is the polarization of the X-ray photons (0.60). θ is the angle between the incident X-ray photons and the sample surface, and n_h is the number of 3d holes. $S(E)$ is a no-free-parameter two-step-like background function removed from the spectra to account for core electrons promoted to the continuum. Since the population of $2p_{3/2}$ states is 2 times larger than $2p_{1/2}$, the step at the L_3 edge is twice as large. $S(E)$ is given as:

$$S(E) = \frac{H(1 + \frac{2}{\pi}) \arctan\left(\frac{E - E_{L_3}}{E_{\text{broad}}}\right)}{3} + \frac{H(1 + \frac{2}{\pi}) \arctan\left(\frac{E - E_{L_2}}{E_{\text{broad}}}\right)}{6} \quad (2.20)$$

H is the average of the 15 highest energy points in the post-edge less the average of the 15 lowest energy points in the pre-edge. E_{L_3} and E_{L_2} are the energies at the L_3 and L_2 absorption peaks, respectively, and the energy broadening (E_{broad}) used was 0.3 eV.

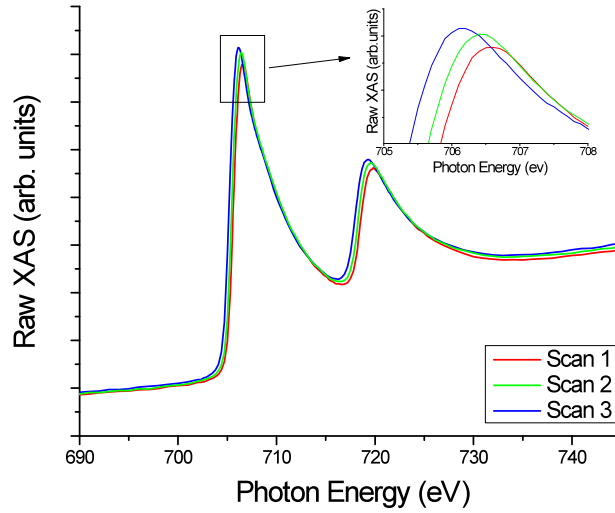


Figure 2.10 Raw XAS spectra for amorphous $x=0.60$, showing an energy shift between scans.

Chapter 3: Chemical Order and Magnetization in Epitaxial, Off-Stoichiometry $\text{Fe}_x\text{Si}_{1-x}$ Thin Films

3.1 Introduction

Different degrees of chemical order, which can significantly tune the magnetic and electronic properties, can be accessed in $\text{Fe}_x\text{Si}_{1-x}$ ($0.55 < x < 0.77$) thin films, making the system an attractive material as a potential spin injector. Thin film growth is required since this composition range exists in the equilibrium phase diagram almost entirely in a two-phase phase field of Fe_3Si and $\epsilon\text{-FeSi}$.¹⁹ Stoichiometric Fe_3Si has the D0_3 crystal structure shown in Figure 3.1a where the unit cell has an fcc Bravais lattice and can be thought of as 8 bcc-like sub-units with Fe (Fe_{II}) on the cube corners and Fe (Fe_{I}) and Si alternating in the body centers.^{13,16} Fe_{II} is surrounded by 4 Fe nearest neighbors (NN) and 4 Si NN and carries a magnetic moment, M , of $1.35 \mu_{\text{B}}$.¹⁶ Fe_{I} is surrounded by 8 Fe NN; M is $2.2 \mu_{\text{B}}$.¹⁶ These two sites are chemically inequivalent. Fe_3Si , a binary Heusler alloy, possess a high Curie temperature and large theoretically predicted spin polarization.^{8,9} Stoichiometric $\epsilon\text{-FeSi}$ has the B20 structure and is considered a ‘Kondo insulator’ with exotic magnetic properties.⁶³ It is also possible to fabricate (metastable) stoichiometric cubic FeSi with the B2 (CsCl) structure; in this structure Fe is located at the cube corners and surrounded by 8 Si NN.¹⁵ Moving to off-stoichiometry compositions in the range $0.55 < x < 0.77$, varying degrees of chemical order are possible. In the completely chemically ordered system (off-stoichiometry D0_3), additional Si (Fe) substitutes onto Fe_{I} (Si) lattice sites (figure 3.1b). Partial ordering occurs in the off-stoichiometry B2 structure, where Fe is ordered at the cube edges, but Fe and Si randomly occupy the body center sites (figure 3.1c). In the A2 structure, there is no long-range chemical ordering, but structural order is maintained.

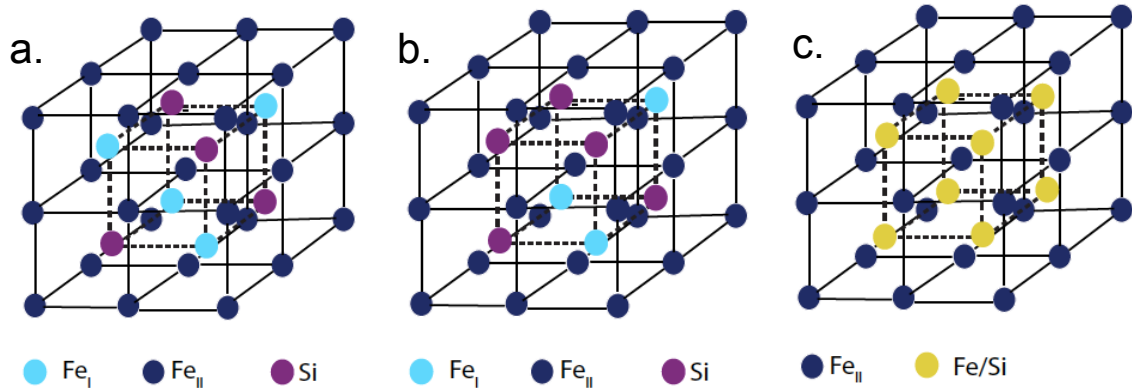


Figure 3.1. (a) D0_3 crystal structure for $x=0.75$ and off-stoichiometry ($x < 0.75$) (b) D0_3 and (c) B2

These varying degrees of chemical order, which can be accessed by thin film growth techniques, can be used to significantly tune the properties of this Heusler alloy.

Experimental work has shown the magnetic properties of bulk $\text{Fe}_x\text{Si}_{1-x}$ alloys (x near 0.75) are strongly dependent on chemical order and Fe concentration.^{16,22} Additionally, theoretical investigations show that the density of states can be tuned by varying the Fe concentration or by doping with small amounts of V, Mn or Cr.^{9,23} Recent work on another Heusler alloy, Co_2FeSi thin films, has shown a reversal of spin polarization due to differences in the density of states between the ordered L2_1 and partially ordered B2 structures.⁶⁴ Clearly, chemical order has an influence on the magnetic and electronic properties of Heusler alloys, however work on $\text{Fe}_x\text{Si}_{1-x}$ thin films has focused on the chemically ordered endpoints of the composition range. Previous studies have investigated compositions deviating slightly from $x=0.75$ and compositions near $x=0.5$.^{14,15,16} Little work has been done between these, with the exception of Berling, *et al.*, who analyzed magnetization but not local chemical order or electronic structure.¹³

In this work, we fabricated and investigated $\text{Fe}_x\text{Si}_{1-x}$ epitaxial thin films ($0.55 < x < 0.77$) with different chemical order (D0_3 and B2); we found that the material has a strong tendency to chemically order so films with the A2 structure were not successfully fabricated. Chemical order was characterized using conversion electron Mössbauer spectroscopy (CEMS). The electronic and magnetic properties of these films were investigated by X-ray absorption spectroscopy (XAS) and X-ray magnetic circular dichroism (XMCD) and compared to theoretical calculations to understand the effects of chemical order on these properties.

3.2 Methods

3.2.1 Theoretical Density Functional Theory (DFT) Calculations

Self-consistent electronic structure calculations for ordered D0_3 $\text{Fe}_x\text{Si}_{1-x}$ ($x=0.77-0.60$), partially ordered B2 $\text{Fe}_x\text{Si}_{1-x}$ ($x=0.67-0.55$) and disordered A2 ($x=0.60-0.80$) were performed within the *ab initio* framework of spin-density functional theory. The Vosko, Wilk, and Nusair parametrization of the exchange and correlation potential was used.⁶⁵ For all systems, the experimental lattice constants (or a linear extrapolation from experimental values) were used. The electronic structure was calculated in a fully relativistic model by solving the corresponding Dirac equation using the spin polarized relativistic multiple-scattering or Korringa-Kohn-Rostoker formalism.⁶⁶ To account for electronic correlations beyond the LSDA, a combined LSDA+DMFT scheme was employed, self-consistent in both the self-energy calculation and the charge density calculation, as implemented within the relativistic SPR-KKR formalism.⁶⁷ Among others, this scheme was successfully used before in describing orbital magnetic moments and XMCD in 3d transition metals.^{68,69} As a DMFT-solver the relativistic version of the so-called Spin-Polarized T-Matrix Plus Fluctuation Exchange (SPTF) approximation was used.^{70,71} In contrast to most other LSDA+DMFT implementations, within the SPR-KKR scheme the complex and energy-dependent self-energy σ_{DMFT} is implemented as an additional energy-dependent potential to the radial Dirac equation, which is solved in order to calculate the new Green's function. This procedure is repeated until self-consistency in both the self-energy and the charge density is achieved. The double

counting problem (separation of the Hubbard Hamiltonian from the LSDA one) was considered within the usual around mean-field (AMF) limit. The self-energy within the DMFT is parameterized by the average screened Coulomb interaction U and the Hund exchange interaction J . For the Fe atoms, $U_{Fe} = 1.5\text{eV}$ and $J_{Fe} = 0.9\text{ eV}$ were used. This is an established value for bulk Fe.⁷² DMFT calculations have been performed for $T=400\text{K}$ and 4096 Matsubara poles were used to calculate the corresponding SPTF self-energy. For the treatment of the chemical disorder in B2 $\text{Fe}_x\text{Si}_{1-x}$ alloys, the coherent potential approximation (CPA) was applied. The CPA is considered to be the best theory among the so-called single-site (local) alloy theories that assume complete random disorder and ignore short-range order. A combination of the CPA and LSDA+DMFT within SPR-KKR method has been used recently.^{68,73,74}

To support the interpretation of the experimental results, the corresponding XAS and XMCD spectra were calculated based on Fermi's golden rule and implemented within the SPR-KKR method.^{56,57} For a direct comparison of the calculated absorption coefficient to experimental data, the corresponding theoretical spectra were broadened in the conventional way; Lorentzian broadening (0.3 eV) was applied to account for the lifetime of the core hole and excited electrons, and Gaussian broadening (0.4 eV) was used to represent finite experimental resolution. The calculations described are referred to as CPA throughout this work.

To investigate the effect of different methods to account for disorder in theoretical DFT calculations, supercell models with 16 atoms were also used. Both D0₃ and B2-like structures were investigated for $x=0.75$. For $x=0.625$ and 0.6875 , some body center Fe atoms of the stoichiometric D0₃ unit cell were replaced by Si, forming off-stoichiometry D0₃-like structures; all the body center atoms were randomized to form B2-like structures. For $x=0.50$, the B2-like and D0₃-like phases are identical with all Fe at cube corner sites surrounded by Si in all the body center sites. The lattice constants of these simulated structures were within 1% of the experimental values. The A2 structure, although not experimentally realized, was also calculated for $x=0.65$. The exchange-correlation functions were treated at the level of generalized-gradient approximation.⁷⁵

3.2.2. Experimental Procedure

Epitaxial $\text{Fe}_x\text{Si}_{1-x}$ thin films (1000-1500 Å) in the composition range $0.55 < x < 0.77$ were grown by electron beam co-evaporation of Fe and Si at 300°C on (001) MgO. Films with concentrations below $x=0.70$ did not grow epitaxially on MgO at 300°C; for these samples, a 30 Å Cr seed layer was deposited at 200°C, followed by the film growth at room temperature in order to obtain epitaxy while limiting interdiffusion of Cr. A similar process was used by Walterfang *et al*.¹⁵ Films intended for X-ray absorption spectroscopy (XAS) measurements were capped with 15-18 Å of Al to prevent oxidation. An epitaxial $x=1.0$ sample was also fabricated as a standard for XAS studies. Structural characterization was performed by x-ray diffraction (XRD) and high-resolution cross section transmission electron microscopy (HRXTEM). The XRD θ - 2θ scans showed only the 100 and 200 (200 and 400) peaks of the B2 (D0₃) crystal structure out-of-plane,

and ϕ scans on the 110 B2 or 220 D0₃ off-axis peak showed sharp peaks (FWHM $\sim 2\text{-}3^\circ$) with the expected four-fold symmetry of an epitaxial film (see figure 2.1 for representative plots). We note the 100 B2 and 200 D0₃ peaks are located at the same 2θ value since the D0₃ unit cell is double the size of the B2 (CsCl) unit cell. The epitaxial relationship between film and substrate is $\text{Fe}_x\text{Si}_{1-x} [100] \parallel \text{MgO} [110]$

⁵⁷Fe conversion electron Mössbauer spectroscopy (CEMS) was used as a local probe of Fe atoms' chemical environment and the resulting atomic magnetic moment. These measurements were performed at room temperature under normal incidence, with a homemade helium-methane gas proportional counter, with ⁵⁷Co in a Rhodium matrix as the source. Isomer shifts are given with respect to α -iron at 300 K, and the spectra were fitted using the histogram method.^{56,57} Macroscopic magnetic properties of the films were investigated with a Superconducting Quantum Interference Device (SQUID) magnetometer at 2K.

X-ray absorption spectroscopy (XAS) and X-ray magnetic circular dichroism (XMCD) were performed at room temperature in total electron yield (TEY) at the Fe L-edge at beamline 6.3.1 at the Advanced Light Source (ALS), Lawrence Berkeley National Lab, Berkeley CA. The spin and orbital moments were calculated based on the methods discussed in 2.7.3.

3.3. Results

3.3.1 Structural Characterization and Chemical Order

The 100 reflection in the A2 (bcc) structure is forbidden by structure factor but present in both D0₃ and B2. From these reflections, it is not possible to distinguish between these two types of order; the nature of the chemical ordering leads to the same intensity and superlattice peak location for both structures with the same composition. Scattering from the (111) planes should produce a diffraction condition for D0₃ but not B2. An estimation of the chemical order is obtained by calculating the intensity ratio of the superlattice to fundamental peaks. The results of these calculations in addition to ratios for perfect chemical order, calculated from atomic scattering factors reported in [54] are plotted in figure 3.2. The ratio decreases as the Fe concentration increases, as expected since at $x=1.0$ the reflection is forbidden. The experimental intensity ratios are close to the calculated values for perfect off-stoichiometry order, indicating epitaxial films with good chemical order. The inset of figure 3.2 is a plot of the out-of-plane lattice constant as a function of Fe concentration. This lattice constant was calculated from the superlattice reflection (*i.e.* 200 D0₃ and 100 B2) in the θ - 2θ x-ray diffraction patterns. The linear variation in lattice constant with x indicates the presence of a single phase.

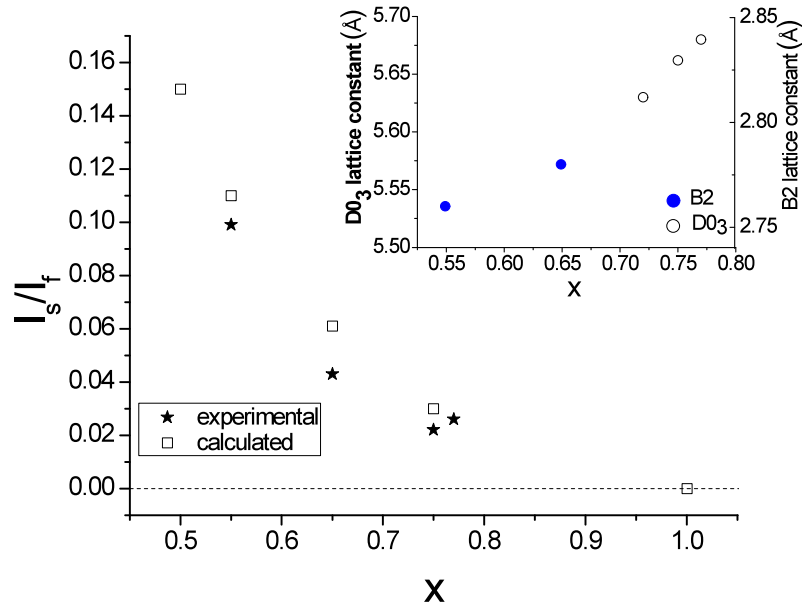


Figure 3.2. Experimental and calculated superlattice to fundamental peak intensity ratios versus x . The inset shows the lattice constants versus x , calculated from the superlattice peak.

HRXTEM was also performed on an epitaxial $x=0.55$ thin film, and figure 3.3 shows the (a) bright field image and (b) electron diffraction pattern. All diffraction spots are indexed to the B2 structure. Lattice fringes are clearly observed in the $[100]$ direction, which corresponds to the out of plane direction of the film. The electron diffraction pattern shows many reflections. The reflections corresponding to the MgO substrate are indexed in white and show the zone axis is $\langle 100 \rangle$. The reflections from the film are indexed in purple; the zone axis for the film is $\langle 110 \rangle$. Superlattice reflections (*i.e.* 001 and 111) are observed, also indicating chemical ordering. These results show the orientation between the film and the substrate is $\text{Fe}_{0.55}\text{Si}_{0.45} [100] \parallel \text{MgO} [110]$. All of these results are consistent with XRD measurements on this sample.

In the top left corner of the bright field image, there is a small region where the lattice fringes are oriented in a different direction, although fringes along the $[100]$ direction can still be distinguished. A Fourier transform of the image from this region reveals spots corresponding to those circled in yellow on the electron diffraction pattern.

The CEM spectrum obtained for $\text{Fe}_{0.77}\text{Si}_{0.23}$ grown on MgO (Figure 3.4a) shows very sharp spectral lines and can be fit with three sextets with in-plane orientation of the magnetic hyperfine field that are represented below to the experimental spectrum. The first component, with a hyperfine field (HF) value of $B_{hf}=19.5$ T, corresponds to the Fe_{II} site in the D0_3 crystal structure of Fe_3Si (see Figure 3.1), in good agreement with other experimental studies.^{14,22} This Fe site has four Fe nearest neighbors (NN) and four Si NN. The second component has a hyperfine field value of $B_{hf}=30.6$ T, which characterizes the

Fe_I site, with eight Fe NN and zero Si NN.²² The last component has a hyperfine field value of $B_{hf}=24.3$ T, corresponding to Fe atoms at the cube edges with five Fe NN and three Si NN, since the sample is off-stoichiometry in Fe concentration.²² The hyperfine field B_{hf} , isomer shift δ and relative area of each component (A_r) are summarized for all samples in Table 3.1.

The CEM spectrum for Fe_{0.75}Si_{0.25} grown on MgO is shown in Figure 3.4b. In this sample, we obtain the three aforementioned components plus one additional sextet, corresponding to the Fe_{II} site with 6 Fe NN.²²

The CEM spectrum obtained for the Fe_{0.65}Si_{0.35} sample (Figure 3.4c) is significantly different, with strong overlapping lines. It has been fit with a wide distribution of magnetically split sextets of varying hyperfine fields and isomer shift values to take into account all the structural and chemical environments of Fe atoms. From this fitting procedure, the average value of the hyperfine field is $\langle B_{hf} \rangle = 14.1$ T.

The CEM spectrum for Fe_{0.55}Si_{0.45} (Figure 3.4d) presents a marked difference from the other spectra. The signal is characteristic of a paramagnetic material with no evidence of magnetically split sextets. This result is consistent with SQUID measurements that confirm the sample is above its transition temperature at room temperature.

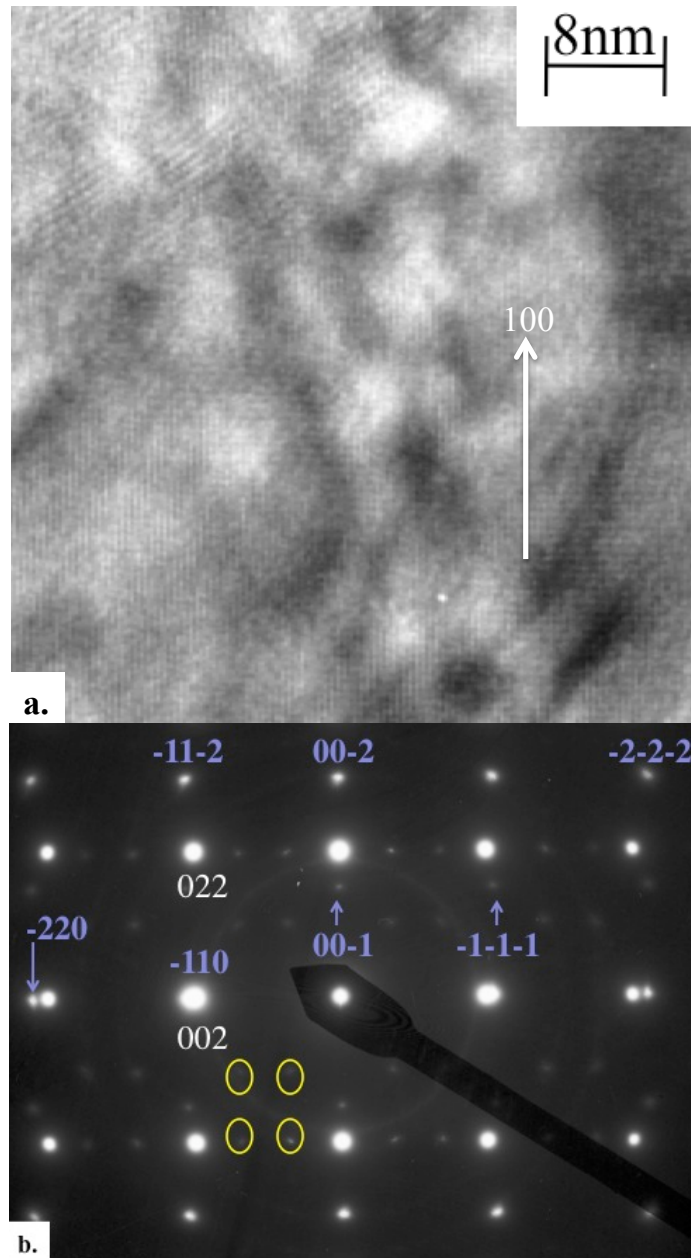


Figure 3.3. (a) Bright field TEM image and (b) electron diffraction pattern from an epitaxial $x=0.55$ thin film. The arrow in (a) indicates the $[100]$ direction. $\sim 10\%$ of the sample is not oriented in the $[100]$ direction (top left corner of bright field image). In (b), the reflections corresponding to the MgO substrate are indexed *below* the spot in white.

The MgO zone axis is $\langle 100 \rangle$. The reflections from the film are indexed to the B2 structure *above* the spot in purple (unless indicated with an arrow); arrows were used when the spots were faint or too close to other spots. The zone axis for the film is $\langle 110 \rangle$. Note that the 002 MgO substrate reflection and the -110 film reflection are the same spot.

Superlattice reflections (*i.e.* 001 and 111) for the film are also indicated. The yellow circles correspond to diffraction spots from the top left corner of the bright field image.

(Image courtesy of D. Smith)

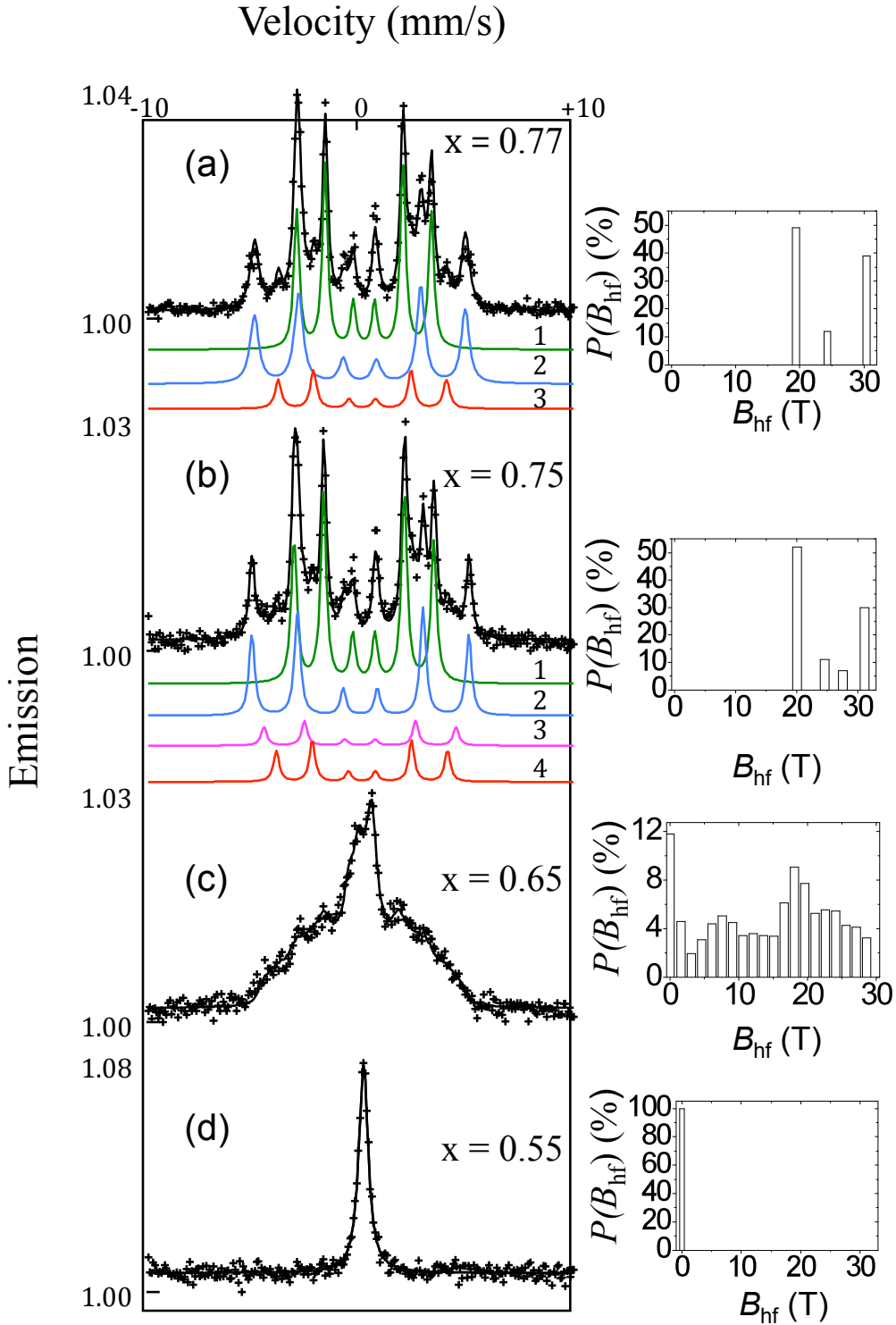


Figure 3.4. Measured CEM spectra at 293 K of epitaxial $\text{Fe}_x\text{Si}_{1-x}$ films on MgO (001) for (a) $x=0.77$, (b) $x=0.75$, (c) $x=0.65$ and (d) $x=0.55$. The right-hand side shows the hyperfine field distribution, $P(B_{\text{hf}})$, for each sample. Corresponding least-squared fitted components (labeled 1-4) are shown below the spectra for (a) and (b); the spectra in (c) are fit with $P(B_{\text{hf}})$.

x	Sample	Comp.	d (mm s ⁻¹)	B_{hf} (T)	A_r
0.77	A	1	0.259	19.4	0.49
		2	0.067	30.4	0.39
		3	0.183	24.3	0.12
0.75	B	1	0.255	20.1	0.52
		2	0.089	31.1	0.30
		3	0.164	24.6	0.11
		4	0.077	27.6	0.07
0.65	D	-	0.144*	14.1*	-

* Average value

Table 3.1. Values of the isomer shift (δ), magnetic hyperfine field (B_{hf}) and relative spectral area (A_r) of the different components (Comp.) deduced from the least-squared fit of the Mössbauer spectra of $\text{Fe}_x\text{Si}_{1-x}$ thin films.

From the CEM spectra a short-range order parameter, $P(4)$, was calculated to quantify the degree of D0_3 chemical order in the films. This parameter was adopted from Gao, *et. al.* and is given below.⁷⁶

$$P(4) = \frac{P^{\text{ex}}(4) - P^{\text{dis}}(4)}{P^{\text{D0}_3}(4) - P^{\text{dis}}(4)} \quad (3.1)$$

$P^{\text{ex}}(4)$ is the experimental fraction of Fe atoms with 4 Fe NN obtained from CEMS. In the well-ordered samples, this number is the relative spectral area for the component with a hyperfine field corresponding to 4 Fe NN, as determined from the fits. For the $x=0.65$ sample with a distribution of B_{hf} , $P^{\text{ex}}(4)$ is the sum of the contributions from components with 22.5T, 21T, 19.5T and 18T hyperfine fields. $P^{\text{dis}}(4)$ is the fraction of Fe atoms that have 4 Fe NN in a random solid solution (A2 structure), calculated from a binomial probability distribution. $P^{\text{D0}_3}(4)$ is the fraction of Fe atoms that have 4 Fe NN in the perfectly ordered D0_3 structure, *i.e.* 2/3. The short-range order parameter, $P(4)$, is only equal to 1 for perfect D0_3 order at $x=0.75$. Table 3.2 gives the calculated order parameters for all of the samples except $\text{Fe}_{0.55}\text{Si}_{0.45}$, which shows a paramagnetic signal in CEMS at room temperature.

x	P(4)	Structure
0.77	0.70	D0_3
0.75	0.74	D0_3
0.65	0.18	B2

Table 3.2. Short range order parameter, $P(4)$, for samples with D0_3 and B2 structure. The sample with composition $x=0.55$ is not reported since CEMS revealed a paramagnet at room temperature.

3.3.2 Electronic Properties

Figure 3.5 shows the (a) experimental and (b) theoretical (CPA) XAS for the Fe concentrations, $x=0.55-1.0$. As the Si concentration increases, broadening of the L_3 edge occurs experimentally. Additional structure exists on the higher energy side of the L_3 peak for the samples containing Si in both theory and experiment. The feature is present at a higher binding energy in the theoretical calculations than what is observed experimentally. The size of the shoulder appears to increase experimentally with increasing Si concentration; for $x=0.55$, the shoulder is not as distinct due to peak broadening. In contrast, the shoulder appears non-monotonic (present for $x=0.75$ and 0.55 but not $x=0.65$) in the theoretical predictions. This result is likely due to how the CPA calculations account for disorder and will be discussed in the next section.

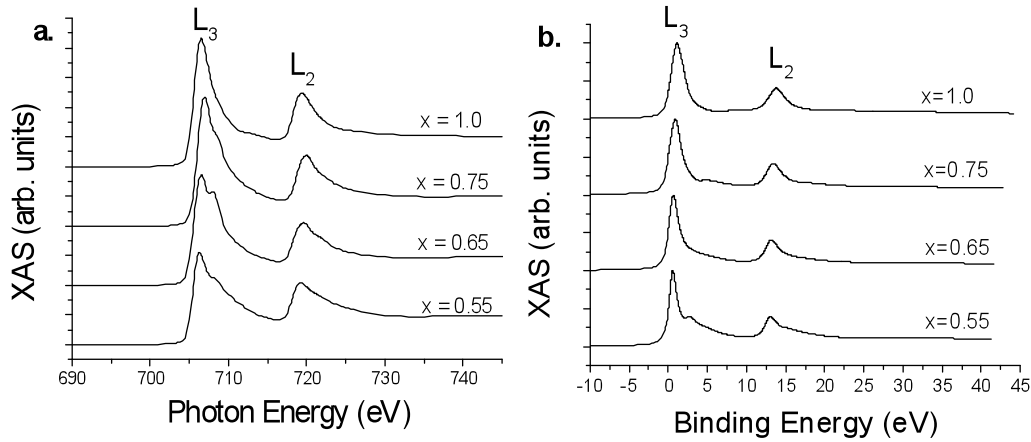


Figure 3.5. (a) Experimental Fe L-edge X-ray absorption spectra and (b) theoretical XAS for $x=0.55-1.0$.

In order to investigate the origin of this peak, the electronic density of states for $x=0.55$ (not shown) and Bloch spectral functions for the $x=0.55$ B2 structure (Figure 3.6a) and non-magnetic bcc Fe (Figure 3.6b) were calculated using the CPA method described. Since the exchange splitting of the bands in the $x=0.55$ composition is small, we compare to non-magnetic bcc Fe; if instead magnetic bcc Fe is considered, the bands being investigated are very high in energy due to large exchange splitting. The density of states for the $x=0.55$ B2 structure indicates the additional peak in the XAS is due to Fe_{II} d-states. The circled regions in figure 3.6a highlight flat bands with d-character, which are expected to contribute to the additional peak. These bands are also present in figure 3.6b, although at higher energy. Hybridization with Si is expected to shift these bands to lower binding energy.

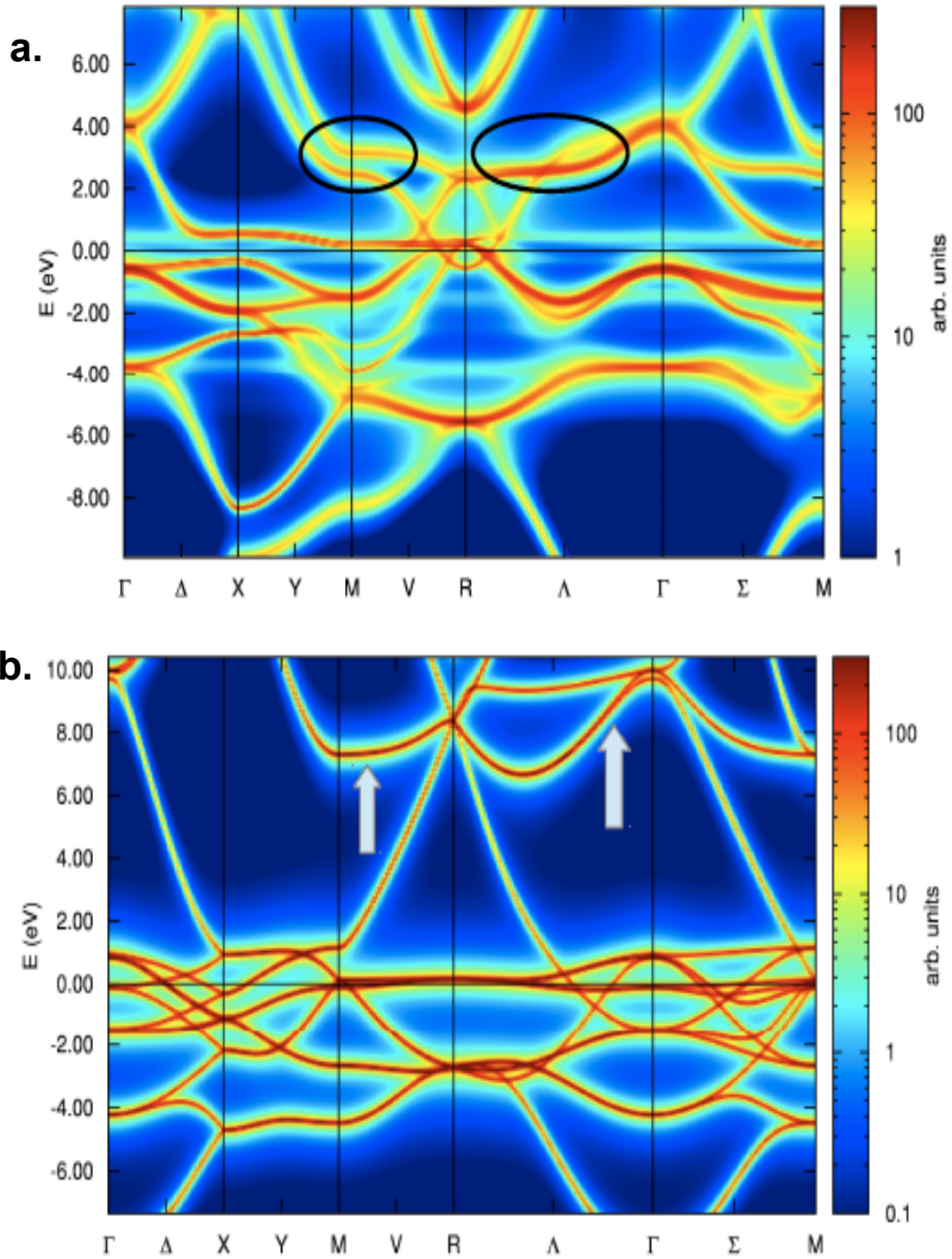


Figure 3.6. Bloch spectral functions for **(a)** the $x=0.55$ B2 structure and **(b)** non-magnetic bcc Fe. The circles in **(a)** indicate the flat bands with d-character, and the arrows in **(b)** show the same bands at higher energy.

3.3.3 Magnetic Properties

From the saturation magnetization at 2 K in M-H curves, μ_B/Fe was calculated for all samples and is presented as a function of composition, x , in Figure 3.7. Also shown in this plot are CPA and supercell theoretical calculations of the magnetic moment for structures with different chemical order, A2, B2, and D0₃ as indicated. The theoretical Fe magnetic moments (CPA and supercell) of the A2 crystal structure are larger than those obtained for the B2 or D0₃ crystal structures, particularly as the Si concentration is increased. The experimental magnetic moments are more similar to the calculated supercell B2 or D0₃ structures than the CPA calculations.

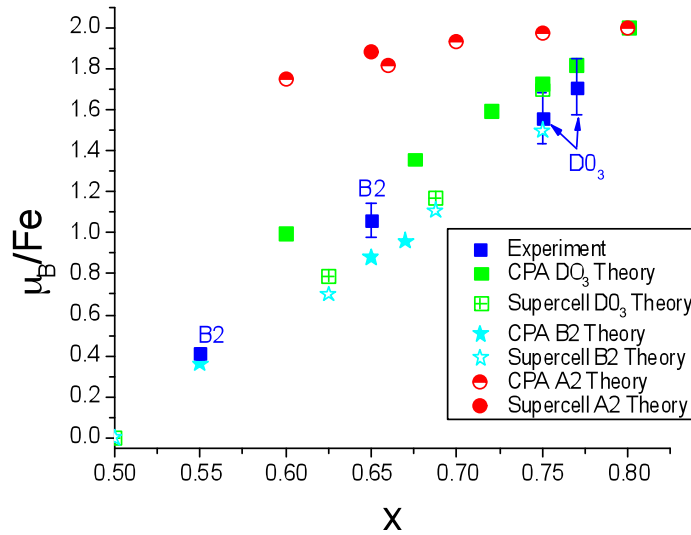


Figure 3.7. Experimental magnetic moments measured at 2 K for $\text{Fe}_x\text{Si}_{1-x}$ epitaxial films and CPA and supercell theoretical calculations for different chemical order – A2, B2 and D0₃.

$M(T)$ for the two lowest Fe concentration samples is shown in figure 3.8. Both show a broad transition, indicating a distribution of magnetic environments in the samples. This observation is consistent with CEMS for $x=0.65$ and indicates some chemical disorder in the system.

The orbital to spin ratio was calculated for all samples, and for the $x=0.75$ and 1.0 thin films the ratios are 0.063 and 0.048, respectively, which are in good agreement with previously reported results on Fe_3Si and Fe thin films.^{14,61} The spin and orbital moments calculated from theory and the experimental spectra at 300 K (and 79 K for $x=0.55$) are shown in Figure 3.9a and 3.9b. The calculations show increasing spin and orbital moments with increasing x ; the experimental trend is consistent for the spin but not the orbital moments. The fact that the experimental orbital moments for $x=0.65$ and 0.75 do not follow the theoretical trend is likely due to local inhomogeneities in the samples, consistent with some chemical disorder observed in CEMS. Though experimental data was measured below T_c for all samples, the theory overestimates the spin moments (and

underestimates the orbital moments). This discrepancy may be due to the discrepancy between CPA theory and experiment for the total moments. The error in the sum rule analysis is estimated to be $\sim 15\%$ due to uncertainty in the incoming X-ray photon polarization and final state effects.

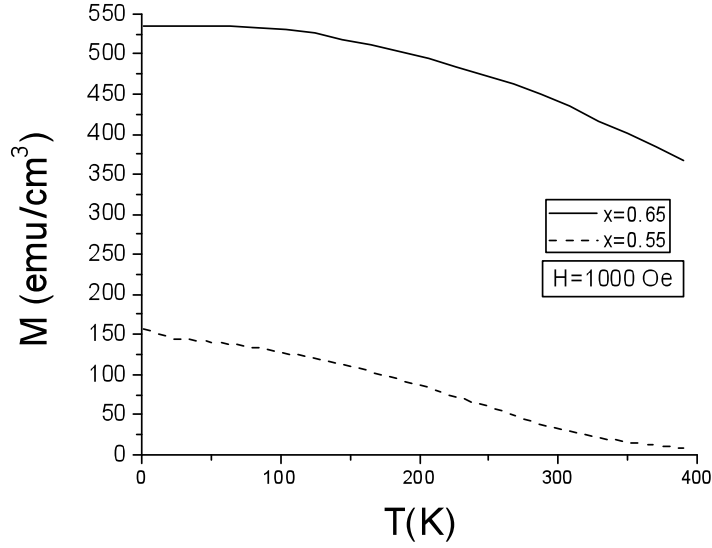


Figure 3.8. $M(T)$ for $x=0.65$ and 0.55 at $H=1000$ Oe.

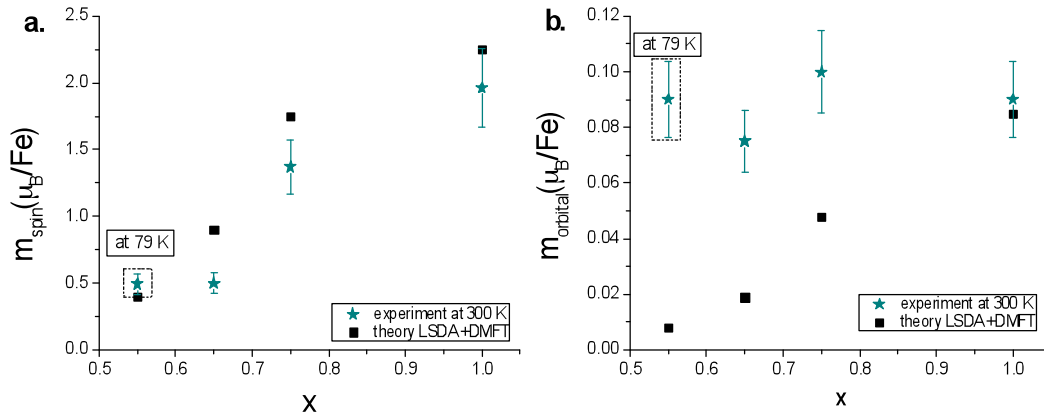


Figure 3.9. Experimental and CPA calculated **(a)** spin and **(b)** orbital moments $x=0.55$ - 1.0 at 300 K. The $x=0.55$ composition is measured at 79 K, as indicated.

3.4. Discussion

The CEMS spectra for $x=0.77$ reflects a site-selective substitution in the perfectly ordered D0_3 crystal structure, meaning that as Fe concentration is increased away from stoichiometric Fe_3Si , the additional Fe substitutes only into the Si sites. This spectra and

the order parameter calculated from it both indicate excellent $D0_3$ chemical order in the sample.

Since the order parameter, $P(4)$, is less than 1 and additional components (Fe with 5 or 6 Fe NN) are present in the fit to the CEMS spectra, the $x=0.75$ sample is not perfectly chemically ordered. This spectrum is consistent with other reports on Fe_3Si thin films grown on MgO and Ge.^{12,14}

The CEMS spectra and the low $D0_3$ order parameter for the $x=0.65$ sample indicate significant chemical disorder. The shape of the hyperfine field distribution is not a Gaussian, meaning it is not a random bcc solid solution of Fe and Si. This result is in agreement with the X-ray diffraction (XRD) pattern where a superlattice peak is observed, indicating that the Fe_{II} sites (cube edges) are still ordered. The sample is only chemically disordered on the Fe_I site, thus it has the B2 structure.⁷⁷

HRXTEM showed small areas (volume fraction $<10\%$) where lattice fringes are oriented in a different direction, corresponding to reflections circled in yellow in the diffraction pattern. Previous work on other bcc alloys has observed similar reflections in the electron diffraction pattern and attributed them to the presence of coherent hexagonal ω -phase precipitates.^{78,79} A more recent work using high-resolution scanning electron microscopy with a high angle annular dark field detector also found these spots and attributed them to additional order along $\{111\}$ type planes.⁸⁰ If small regions in the sample locally had $D0_3$ ordering, this would result in different ordering in $\{111\}$ planes, however from this data, ω -phase precipitates cannot be ruled out. The volume fraction is very small and does not affect the overall properties; XRD (superlattice to fundamental intensity ratio) and magnetization results are consistent with theoretical predictions for a uniform B2 alloy.

The chemical order influences the magnetic moment in these systems. In a random solid solution, an Fe-Fe pair is statistically more likely than in the chemically ordered structure, and in these Heusler alloys the total magnetic moment is strongly dependent on the number of Fe nearest neighbors.¹⁶ Thus the theoretically predicted moment for the A2 structure is much larger than for the B2 or $D0_3$ structure at the same composition. The theoretically predicted magnetic moments for the B2 and $D0_3$ crystal structure are very similar for the supercell calculations but not the CPA. They should, in fact, be essentially the same since the first nearest neighbor environments are the same; on average there are the same number of Fe-Fe first nearest neighbor pairs in both structures. Only the second nearest neighbor environments, which have a weaker effect on the magnetic moment, are different. CPA accounts for disorder by calculating an “average atom”, which evidently produces a different result than the distinct Fe sites in the supercell calculation. We note that the materials investigated here are not expected and do not follow the Slater-Pauling rule for Heusler compounds since they are chemically disordered with a non-integer number of electrons.^{81,82,83}

The additional feature on the high energy side of the L_3 absorption peak is due to hybridization between Si s-states and Fe d-states at the Fe_{II} site, consistent with previous work.¹⁴ The presence of this shoulder in the experimental spectra indicates two chemically distinct Fe sites for all x . The CPA theory predicts the shoulder for the $x=0.75$ composition, where the calculation accounts for two chemically inequivalent Fe sites in the $D0_3$ structure. However, for $x=0.65$ and 0.55 there are no distinct Fe sites due to the “average atom” used in the CPA calculations. Thus, the shoulder is only observed for the $x=0.55$ composition where the “average atom” is mostly Si (90%).

As the Fe concentration decreases from stoichiometric $x=0.75$, the system becomes more chemically disordered, however it never becomes the fully disordered A2. Attempts to grow low Fe concentration samples at reduced growth temperatures to obtain the A2 structure resulted in amorphous films. Surprisingly, the crystalline systems tends toward an ordered structure, B2 for $x \leq 0.65$ and $D0_3$ for $x > 0.65$. CEMS, $M(T)$ and experimental orbital moments all indicate evidence of some chemical disorder in the samples.

3.5. Conclusion

The chemical order, electronic and magnetic properties of epitaxial Fe_xSi_{1-x} thin films ($0.55 < x < 0.77$) were investigated. The films showed excellent structural order and varying degrees of chemical order based on CEMS, HRXTEM and XAS. B2 chemical order was observed for $x \leq 0.65$ and $D0_3$ for $x > 0.65$. Even very far from the equilibrium composition, $x=0.75$, the films still tended towards chemical order; the A2 structure was not successfully fabricated. The theoretically calculated magnetic moments for the B2 and $D0_3$ structures are different in the CPA calculations but not the supercell; both are reduced from the A2 moment due to less Fe-Fe pairs. Experimental and theoretical (CPA) XAS spectra revealed an additional feature on the high energy side of the L_3 peak due to Fe-Si hybridization.

Chapter 4: Magnetism and Local Atomic Structure in Amorphous $\text{Fe}_x\text{Si}_{1-x}$ Thin Films

4.1 Introduction

Magnetism in transition metal alloys is strongly influenced by the local atomic structure; investigations of amorphous and crystalline structures allow the magnetic properties of the same chemical species in a different local atomic environment to be directly compared. Studies have been performed to compare the magnetic properties of amorphous and crystalline Fe-based alloys such as $\text{Fe}_x\text{B}_{1-x}$, $\text{Fe}_x\text{P}_{1-x}$ ($x \sim 0.75$) or $\text{Fe}_x\text{Zr}_{1-x}$ ($x \sim 0.25-0.34$); crystalline $\text{Fe}_x\text{Co}_{1-x}$ and $\text{Ni}_x\text{Fe}_{1-x}$ ($0.5 < x < 1.0$) alloys have also been compared to amorphous (FeCo)G and (NiFe)G (G=SiB, PC or PB).^{84,85,86,87} These studies are limited in one of two ways: either the crystalline analog is a specific stoichiometric phase (e.g. Fe_3B , Fe_3P , Fe_2Zr) thus limiting the composition range of the comparison, or the crystalline system encompasses a wide composition range (e.g. $\text{Fe}_x\text{Co}_{1-x}$ or $\text{Ni}_x\text{Fe}_{1-x}$, $0.5 < x < 1.0$) but the corresponding amorphous phase is formed by alloying with metalloids (Si, B, P or C), which affect the magnetic properties.⁸⁷ Ideally, these investigations should be performed on a single system where amorphous and crystalline structures could both be fabricated over a large composition range, allowing for a direct comparison.

In addition to being a potential spin-injector, the $\text{Fe}_x\text{Si}_{1-x}$ system is unique in that thin film growth techniques allow access to varying degrees of both chemical and structural order over a wide composition range, $0.45 < x < 0.75$. In the crystalline system, three different bcc-like structures (D0_3 , B2, A2), each with a different degree of chemical order are possible. The A2 structure is a chemically disordered random bcc solid solution, and the B2-like structure is a partially ordered CsCl structure with Fe on the cube corner sites and Fe/Si randomly arranged on the body center sites. Finally, the D0_3 -like structure is chemically ordered with Fe on the cube corners and Fe and Si alternating in the body centers. The magnetic moment in these metallic crystalline materials ranges from $0 \mu_B/\text{Fe}$ ($x=0.50$, B2) to $1.65 \mu_B/\text{Fe}$ ($x=0.75$, D0_3).^{13,15} The properties of these various metallic structures differ widely from the $x=0.50$ equilibrium ϵ -FeSi phase, which is a 'Kondo insulator' with exotic magnetic properties.⁶³ Amorphous $\text{Fe}_x\text{Si}_{1-x}$ thin films can also be fabricated, allowing for a comprehensive and direct comparison of the magnetic properties.

Local atomic structures in amorphous solids are generally determined by bond type. In semiconductors with covalent bonding, the structure is typically referred to as a continuous random network (CRN), where each atom has a few (2-4) directional bonds.²⁰ On the other hand, amorphous metals typically form random dense-packed structures with coordination numbers between 8-12 due to the non-directionality of their bonds.²⁰ The structure of an amorphous alloy of Fe and Si might be expected to vary from CRN for the Si-rich compositions to a dense-packed structure on the Fe-rich side.

Amorphous Fe has previously been prepared by quench-condensing and found to be ferromagnetic with a decreased magnetic moment ($1.50 \pm 0.15 \mu_B/\text{Fe}$) as compared to crystalline bcc Fe ($2.20 \mu_B/\text{Fe}$).^{24,25} This reduction was attributed to the distribution of interatomic distances leading to both positive exchange interactions (similar to α -Fe) and negative exchange interactions (similar to γ -Fe). Additionally, many amorphous $\text{Fe}_y\text{Z}_{1-y}$ alloys ($Z=\text{Nb, Ta, Y, Zr, Lu}$) are ferromagnetic as y approaches 1, with moments ranging from 0.7-1.8 μ_B/Fe depending on y and Z , but all exhibit spin glass behavior with decreasing y ($y=0.64$ -0.80).^{26,27,28,29,30} Previous reports on the local structure and magnetism are somewhat contradictory for the Fe-rich compositions ($x>0.5$).^{21,88} Based on analysis of electron diffraction patterns, Mangin *et al.* reported local short-range ordering with approximately 12 nearest neighbors, meaning a local environment similar to fcc γ -Fe.²¹ An alloy with such a local environment should, in principle, be antiferromagnetic. However the same authors also reported relatively large magnetic moments in these films (e.g. 1.44 μ_B/Fe for $x=0.62$).²¹

In this work, we prepared and investigated the magnetic, structural and electronic properties of amorphous $\text{Fe}_x\text{Si}_{1-x}$ thin films and compared these to epitaxial films of the same composition ($0.45<x<0.75$). We found all films to be ferromagnetic at 2 K with large magnetization, M (e.g. 1.73 μ_B/Fe for $x=0.65$); all films with $x\geq 0.60$ were also ferromagnetic at 300 K. Remarkably, the amorphous films possess significantly larger magnetization than their crystalline counterparts. Sum rule analysis of X-ray magnetic circular dichroism (XMCD) spectra show enhancement in both spin and orbital contributions. We performed a careful study of the local atomic structure using X-ray absorption fine structure (XAFS) and compared these data to results of *ab initio* molecular dynamics (MD) calculations based on density functional theory (DFT) to understand the local structural ordering and the enhanced magnetization. The electronic structure and the spin polarization in the amorphous structures with various x and crystalline structures with different chemical order ($x\sim 0.65$) were also compared. Experimental spin polarization measurements were performed using Andreev reflection, and remarkably, the amorphous films show an enhancement in spin polarization relative to crystalline films with the same composition.

4.2. Methods

4.2.1. Theoretical DFT Calculations

Theoretical calculations were performed on amorphous compositions $x=0.50, 0.55, 0.65$ and 0.75. *Ab initio* molecular dynamics simulations were performed to simulate the amorphous structure in an $L_xL_yL_z$ unit cell of volume V containing 128 atoms using the plane-wave-based Vienna *ab initio* simulation package (VASP)⁸⁹, with the projector augmented wave (PAW) method for the description of core-valence interaction.⁹⁰ The exchange-correlation functions were treated at the level of generalized-gradient approximation.⁷⁵ The structure underwent a melting (2000 K) step followed by a quenching (2000 K – 200 K at $3 \times 10^{14} \text{ Ks}^{-1}$) and annealing process (200 K, 5 ps) in a canonical ensemble for the randomization of structural positions of the 128 atoms. The

atomic spacing, positions and cube size L^3 were further optimized before and after the quenching and annealing processes, until forces on each atom were less than $0.01 \text{ eV}\text{\AA}^{-1}$. Throughout this work, an energy cutoff of 350 eV was used for the expansion of plane-wave basis functions. While only the Γ -point was used to sample the Brillouin-zone during the melting, quenching and annealing processes, $3\times3\times3$ Monkhorst-Pack k -points were used for the geometry relaxation and electronic structure determination after the molecular dynamics simulations. For the crystalline $\text{Fe}_x\text{Si}_{1-x}$ alloys, supercell models with 16 atoms were used. Both D0_3 and B2 -like atomic arrangements were investigated for $x=0.75$. For $x=0.625$ and 0.6875 , some Fe atoms in the body centers of the stoichiometric D0_3 unit cell were replaced by Si, in order to form off-stoichiometry D0_3 -like structures; all the body center atoms were randomized to form B2 -like structures. For $x=0.50$, the B2 -like and D0_3 -like phases are identical with all Fe at cube corner sites surrounded by Si in all the body center sites. The lattice constants of these simulated structures were within 1% of the experimental values. The A2 structure, although not experimentally realized, was also calculated for $x=0.65$.

4.2.2. Experimental Procedure

$\text{Fe}_x\text{Si}_{1-x}$ ($0.45 < x < 0.65$) thin films (1300-2200 Å) were grown by electron beam co-evaporation of Fe and Si. Amorphous films were grown at room temperature on amorphous SiN_x on Si substrates, and epitaxial $\text{Fe}_x\text{Si}_{1-x}$ thin films were obtained by deposition on (001) MgO at 200 °C for $x \geq 0.65$. For samples with compositions $x < 0.65$, a Cr layer, deposited at 200 °C on (001) MgO prior to film growth was necessary to obtain epitaxy. The deposition rate for each source was monitored individually with quartz crystal microbalances. The deposition rate for Fe was held at 0.35 Å/s , and the Si evaporation rate was varied to obtain the desired composition. Films were capped with approximately 15 Å of Al to prevent oxidation. Film number densities, n_{total} , and compositions were measured using Rutherford backscattering spectrometry (RBS), and sample thicknesses were measured with an Alpha-Step IQ profilometer. X-ray diffraction (XRD) and high resolution transmission electron microscopy (HRTEM) were used to characterize structure. Magnetization (M) versus field (H) and temperature (T) were measured using a Quantum Design PPMS magnetometer.

X-ray absorption fine structure (XAFS) was measured at beamline 20-BM-XOR at the Advanced Photon Source (APS), Argonne National Laboratory (ANL), Argonne, IL; room temperature measurements were performed at the Fe K-edge in X-ray fluorescence mode with a Vortex Si drift detector. XAFS data were fit in R-space using FEFFIT with theoretical scattering amplitudes and phase shifts calculated by FEFF.^{59,60}

X-ray absorption spectroscopy (XAS) and X-ray magnetic circular dichroism (XMCD) were performed at room temperature and 79 K in total electron yield (TEY) at the Fe L-edge at beamline 6.3.1 at the Advanced Light Source (ALS), Lawrence Berkeley National Lab, Berkeley CA. The spin and orbital moments were calculated based on the methods discussed in 2.7.3.

Andreev reflection spectroscopy was performed to compare the spin polarization in amorphous and epitaxial $x=0.65$ films using either a Nb or Pb tip; no differences were observed between the tip materials. The sample and tip were enclosed in a vacuum jacket and cooled to low temperatures (less than 3 K), where a point contact was established. Differential conductance (dI/dV) and resistance (V/I) were measured from over 40 points on the sample using a lock-in method.

4.3. Results

4.3.1. Magnetism

4.3.1.A. Theoretical DFT Calculations

The compositions $x=0.50$, 0.55 , 0.65 and 0.75 were selected for *ab initio* molecular dynamics (MD) calculations of amorphous $\text{Fe}_x\text{Si}_{1-x}$. For each x , the magnetization is obtained by dividing the total moment by the number of Fe atoms in the cell. The calculated magnetic moment for both amorphous and crystalline alloys is shown in figure 4.1 and agrees well with the experimental data (discussed in section 4.3.1.B.). We note that theory predicts zero magnetic moment for the crystalline (B2) alloy with $x=0.5$ (all Fe are surrounded by Si) and $0.63 \mu_B/\text{Fe}$ for the amorphous alloy, consistent with the experimental results. Also included in figure 4.1 is the calculated magnetic moment for the A2 structure with $x=0.65$. This structure is chemically disordered and has a significantly larger moment than B2 or D0_3 . The B2 and D0_3 structures, for all x studied, have the same magnetic moment; the nearest neighbor environments are the same and only the second nearest neighbors, which have a smaller effect on the magnetization, differ. The magnetic moment in these different structures is strongly dependent on chemical order.

4.3.1.B. Experimental Thin Film Magnetism

Figure 4.1 also shows experimental magnetization at 2 K versus Fe concentration, x , for both crystalline and amorphous films. Strikingly, for all x , the magnetization of the amorphous samples is very large in comparison to crystalline samples with the same compositions. For $x=0.65$, the theoretical moment for the random bcc (A2) structure is also shown; this structure has not been successfully fabricated since the material has a strong tendency to chemically order.

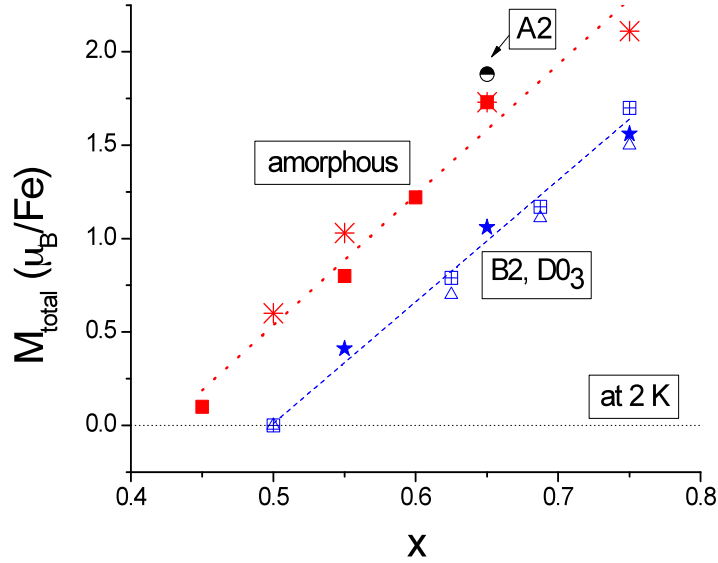


Figure 4.1. Magnetization at 2 K versus Fe concentration for $\text{Fe}_x\text{Si}_{1-x}$ amorphous and crystalline materials. Solid symbols are experimental data: amorphous films (red squares) and epitaxial films (blue stars). Open symbols are theory: amorphous (red stars), A2 (half filled black circle), B2 (blue triangle), D0_3 (blue square with cross). The red and blue dashed lines are a guide to the eye. The error is less than the size of the data points.

Figure 4.2 shows $M(H)$ curves (a) at 300 K for $x=0.65$ amorphous and epitaxial samples and (b) normalized $M(T)$ measurements for amorphous and epitaxial films with $x=0.65$ and $x=0.55$. A comparison of $M(T)$ measurements for all amorphous samples is shown in figure 4.2c. Samples with compositions $x \geq 0.60$ are ferromagnetic at room temperature, and samples with $x < 0.60$ are above or near their transition at room temperature. The $M(T)$ curves for all x show a broad transition, indicating a distribution of magnetic environments. Based on figure 4.1, the composition where ferromagnetic order appears is $x \sim 0.41$. The $x=0.45$ sample is very close to this composition; figure 4.2d shows normalized M versus H/T for this sample and Brillouin functions with $S=1/2$ and $3/2$. The sample shows remanence and M larger at all H than the Brillouin function, indicating weak ferromagnetism.

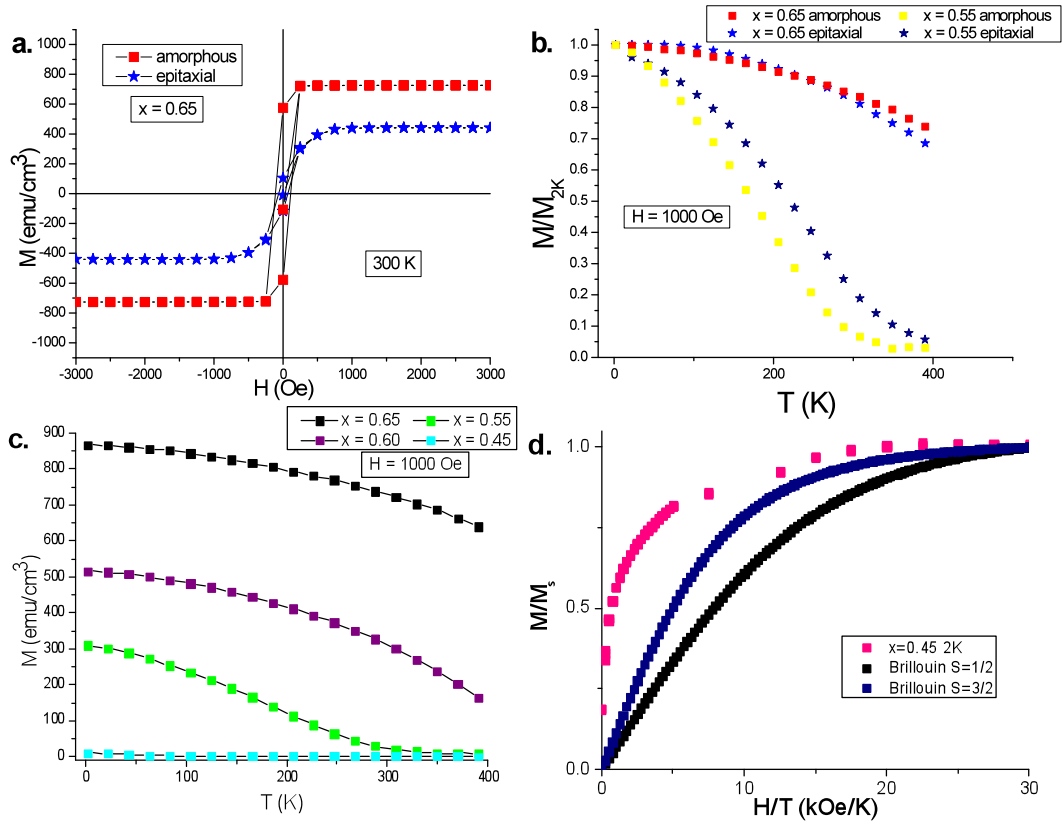


Figure 4.2. (a) $M(H)$ for amorphous and epitaxial $x=0.65$, (b) normalized $M(T)$ measurements for amorphous and epitaxial $x=0.65$ and $x=0.55$, (c) $M(T)$ measurements for all amorphous films and (d) normalized M vs H/T for $x=0.45$ and Brillouin functions ($S=1/2, 3/2$) at 2 K.

Figure 4.3 shows the XAS for (a) the epitaxial samples, $x=0.55-1.0$ and (b) the amorphous samples, $x=0.45-0.65$. The amorphous spectra are broadened in comparison to the epitaxial samples. In both amorphous and epitaxial sample sets, the intensity of the absorption decreases as the Si concentration increases, as expected. From the XMCD spectra, individual spin and orbital moments were calculated and are shown in Figure 4.4a (spin) and 4.4b (orbital) for both the amorphous and epitaxial thin films at 300 K. Our spin and orbital moments for epitaxial $x=0.75$ and 1.0 thin films are in good agreement with previous reports.^{14,61} For other x , the spin moment for both the amorphous and epitaxial films increases with increasing x . The spin moment is larger in the amorphous films. For $x=0.55$ the spin moments at 300 K are near zero since the transition temperature for both films is near 300 K; however in measurements at 79 K, the amorphous film exhibits a much larger spin moment than the epitaxial film. The amorphous films' orbital moments also increase with increasing x and are also larger than the crystalline samples with the same composition. The absolute error in the sum rule

analysis is estimated to be ~15% due to uncertainty in the incoming X-ray photon polarization and final state effects.

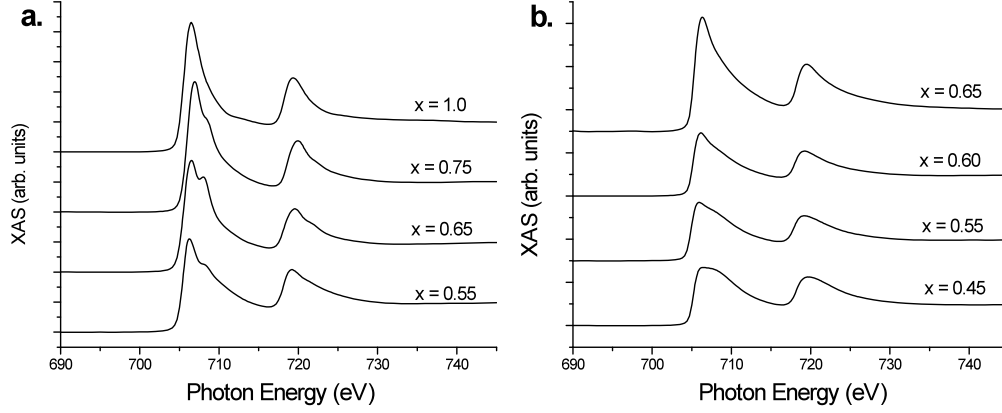


Figure 4.3. XAS spectra for (a) epitaxial and (b) amorphous films.

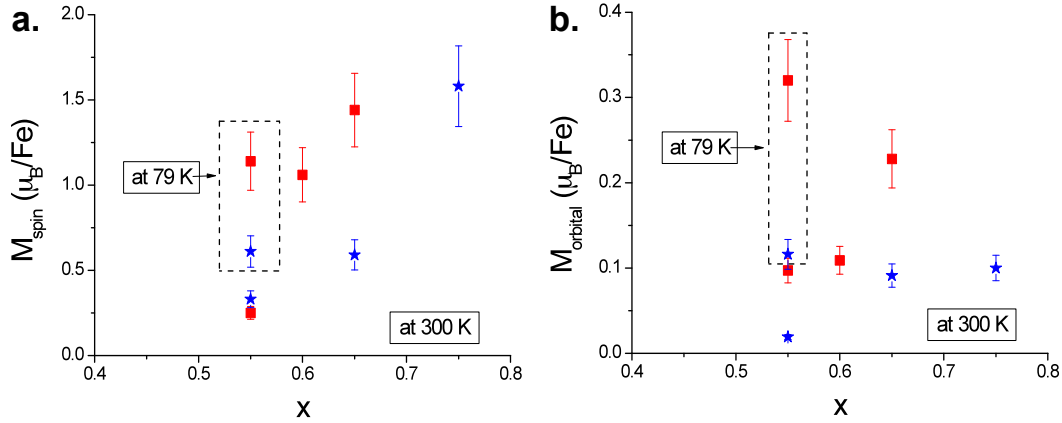


Figure 4.4. (a) Spin and (b) orbital moments, calculated from the sum rules versus x for amorphous and epitaxial thin films. Measurements were performed at 300 K (except as indicated) in ± 0.5 T. Symbols are experimental data: amorphous films (red squares) and epitaxial films (blue stars). The $x=0.55$ data enclosed by a box is at 79 K.

4.3.2. Local Atomic Structure

4.3.2.A. Theoretical DFT Calculations

For each x (0.50, 0.55, 0.65 and 0.75), the total number density, n_{total} , is determined by N/V , where $N = 128$, the total number of atoms and V is the fully relaxed volume after the quenching and annealing process described in 4.2.1. The calculated number density for both amorphous and crystalline alloys is shown in figure 4.5, and agrees well with the experimental data (discussed in 4.3.2.B.).

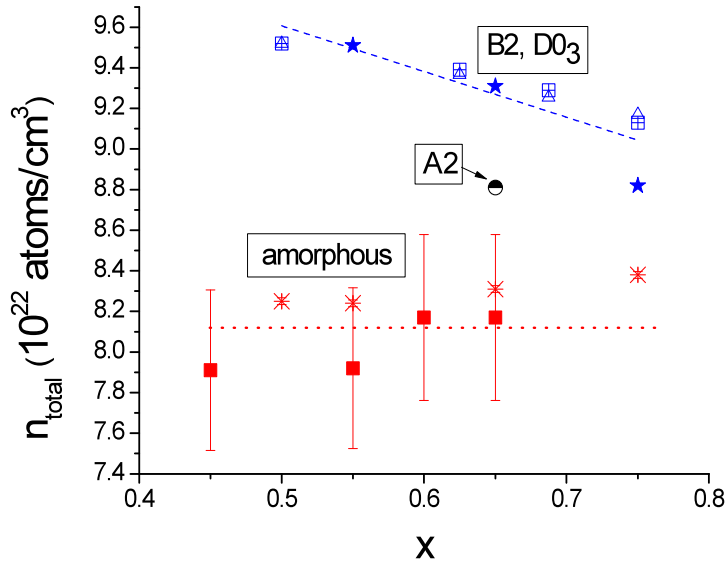


Figure 4.5. Total number density versus Fe concentration for $\text{Fe}_x\text{Si}_{1-x}$ amorphous and crystalline materials. Solid symbols are experimental data: amorphous films (red squares) and epitaxial films (blue stars). Open symbols are theory: amorphous (red stars), A2 (half filled black circle), B2 (blue triangle), D0₃ (blue square with cross). The red and blue dashed lines are a guide to the eye.

The local chemical order in amorphous alloys can be directly characterized by the partial pair correlation function (PCF), which is defined as the number of *e.g.* A-B pairs in the spherical shell ranging from r to $(r + dr)$ around one *A*-type atom. Quantitatively, it is calculated by:

$$g_{AB}(r) = \frac{L^3}{N_A N_B} \frac{\sum_{A,B}^{N_A N_B} n_{AB}(r)}{4\pi r^2 dr} \quad (4.1)$$

where L is the length of the 128-atom cubic unit cell, N_A and N_B are the numbers of *A* and *B* atoms, respectively in the unit cell, and n_{AB} is the average number of *B*- atoms around *A*-type atoms in the spherical shell $r \sim (r + dr)$. There are three partial PCFs and one total PCF for the $\text{Fe}_x\text{Si}_{1-x}$ binary alloys: $g_{\text{FeFe}}(r)$, $g_{\text{FeSi}}(r)$, $g_{\text{SiSi}}(r)$, and $g_{\text{tot}}(r)$.

The DFT calculated total pair correlation function, $g_{\text{tot}}(r)$, is shown in black in figure 4.6a and 4.6b for two representative amorphous $\text{Fe}_x\text{Si}_{1-x}$ alloys, $x=0.55$ and $x=0.65$. Broad peaks are observed instead of the sharp lines of the crystalline phase, indicating the structure is amorphous after the simulated annealing. The first peak of $g_{\text{tot}}(r)$ can be fit well to two Gaussians (green and blue lines), corresponding to the first and second shells of atoms. Each of these shells includes Fe-Fe, Fe-Si and Si-Si pairs. Relative to the

magenta peaks from D0₃ Fe₃Si, the positions are shifted to slightly smaller r , consistent with a decreasing bond length as x decreases.

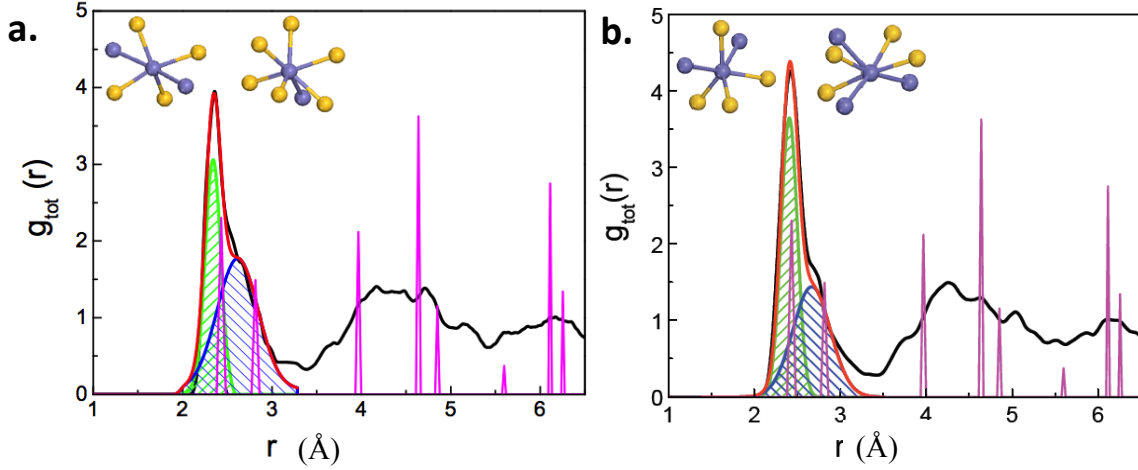


Figure 4.6. The calculated total pair correlation function, $g_{tot}(r)$, (black) of $\text{Fe}_x\text{Si}_{1-x}$ amorphous alloys, (a) $x=0.55$ and (b) $x=0.65$. The green and blue shades display the fitted Gaussians of the first peak, and the red is the sum of the two fits. The $g_{tot}(r)$ of D0₃ Fe₃Si is represented by the magenta lines. The insets display two typical structures of Fe (blue) and Si (yellow) atoms around an Fe atom within 2.3~2.6 Å.

From the total pair correlation function, the coordination number in the first (CN^1) or first + second (CN^2) shell can be determined from:

$$CN^i = n_{total} \int_0^{r_{min}^i} 4\pi r^2 g_{tot}(r) dr \quad (4.2)$$

where r_{min} is the radius at the minimum of the first or second Gaussian. Similarly, the number of Fe-Fe (Fe-Si) pairs in the i shell of nearest neighbors (N_{Fe-Fe}^i , N_{Fe-Si}^i) can be determined from the integral of $g_{Fe-Fe}(r)$ ($g_{Fe-Si}(r)$).

N_{Fe-Fe}^1 , N_{Fe-Si}^1 and N_{Fe-Fe}^2 (the number of Fe-Fe second nearest neighbors) and interatomic distances of the first (r_{Fe-Fe}^1 and r_{Fe-Si}^1) and second shells (r_{Fe-Fe}^2 , r_{Fe-Si}^2) are listed in Table 4.1 for all the compositions investigated. r_{Fe-Si}^1 is slightly smaller than r_{Fe-Fe}^1 , due to the smaller size of Si atoms. Both r_{Fe-Si}^1 and r_{Fe-Fe}^1 increase with x . In the D0₃ and B2 structures, r_{Fe-Si}^1 and r_{Fe-Fe}^1 are equal and also increase with x . No Fe-Fe pairs were observed in the first Gaussian for $x=0.50$ or 0.55 ; for these compositions, Fe atoms are completely surrounded by Si. The coordination numbers, CN^1 and CN^2 are significantly smaller for all x than the corresponding values, 8 and 14 respectively, in the bcc structure. N_{Fe-Fe}^1 increases with x while N_{Fe-Si}^1 decreases causing CN^1 to remain almost unchanged. These data demonstrate that the local chemical order around Fe is intermediate between the bcc-type ($CN^1=8$) and CRN-Si type ($CN^1=4$) structures. For all x , the first shell local environment is dominated by Fe-Si pairs, whereas the second shell is dominated by Fe-Fe pairs.

Atomic % Fe	$N_{\text{Fe-Fe}}^1$	$r_{\text{Fe-Fe}}^1$ (Å)	$[\sigma_{\text{Fe-Fe}}^1]^2$ (Å ²)	$N_{\text{Fe-Si}}^1$	$r_{\text{Fe-Si}}^1$ (Å)	$[\sigma_{\text{Fe-Si}}^1]^2$ (Å ²)	$N_{\text{Fe-Fe}}^2$	$r_{\text{Fe-Fe}}^2$ (Å)	$[\sigma_{\text{Fe-Fe}}^2]^2$ (Å ²)	$N_{\text{Fe-Si}}^2$	$r_{\text{Fe-Si}}^2$ (Å)
0.45 XAFS	0	-	-	4.5 ±0.2	2.33 ±0.05	0.009	5.2 ±0.2	2.70 ±0.05	0.02	-	-
0.50 DFT	0	-	-	5.0 ±0.2	2.36 ±0.02	-	5.5 ±0.5	2.74 ±0.02	-	1.5 ±0.3	2.64 ±0.02
0.55 XAFS	0	-	-	3.7 ±0.2	2.34 ±0.05	0.009	5.6 ±0.2	2.67 ±0.05	0.02	-	-
0.55 DFT	0	-	-	4.3 ±0.2	2.34 ±0.02	-	5.1 ±0.5	2.67 ±0.02	-	1.3 ±0.3	2.62 ±0.02
0.60 XAFS	1.0 (fixed)	2.47 (fixed)	0.05	2.8 ±0.2	2.35 ±0.05	0.007	-	-	-	-	-
0.65 XAFS	2.1 (fixed)	2.47 (fixed)	0.05	2.1 ±0.2	2.34 ±0.05	0.006	-	-	-	-	-
0.65 DFT	2.10 ±0.2	2.47 ±0.02	-	3.7 ±0.2	2.38 ±0.02	-	4.1 ±0.5	2.79 ±0.02	-	1.0 ±0.3	2.72 ±0.02
0.75 DFT	4.06 ±0.2	2.50 ±0.02	-	2.4 ±0.2	2.42 ±0.02	-	3.2 ±0.5	2.83 ±0.02	-	1.2 ±0.3	3.03 ±0.02

Table 4.1. Coordination number, bond length and mean square disorder in bond length from DFT calculations or determined from fits to experimental XAFS data for first shell (grey) and second shell (white).

4.3.2.B. Experimental Structural Characterization

No peaks were observed in θ - 2θ scans of the amorphous films, indicating no significant crystallization. High-resolution (HR) cross-sectional TEM from an $x=0.55$ amorphous sample displayed no clear nanocrystallinity. In a few places, (diameter < 2nm) we observe evidence of poorly defined lattice fringes (see figure 2.6). An $x=0.67$ sample displayed nanocrystals (~20% volume fraction) on the order of 5 nm embedded in an amorphous matrix (see figure 2.5), suggesting nanocrystal precursors increase (in size and number) with increasing Fe concentration.

For the crystalline films, both θ - 2θ and ϕ X-ray diffraction scans were performed. The θ - 2θ scans showed only the 100 and 200 peaks of the bcc crystal structure out-of-plane, and ϕ scans on the 220 off-axis peak showed sharp peaks (FWHM ~2-3°) with the expected four-fold symmetry of an epitaxial film. The presence of the 100 peak indicates B2 or D0₃ chemical order since this peak would be absent in the chemically disordered A2 (bcc) structure. The ratio of the 100 to 200 peak intensities was 0.022, 0.043 and 0.099

for $x=0.75$, $x=0.65$ and $x=0.55$, respectively, which represents good chemical order (comparable to the calculated peak intensity ratios of 0.03, 0.06 and 0.11); note that 100/200 peak ratio is identical for the $D0_3$ and $B2$ structures due to the nature of their chemical ordering. The coherence length of the chemical order and structural order, as calculated from the width of the 100 and 200 peaks respectively, is ~ 240 Å for all x studied. The chemical ordering was $B2$ (CsCl) for $x \leq 0.67$ and $D0_3$ for $x > 0.67$, as determined by conversion electron Mössbauer spectrometry (CEMS).

Figure 4.5 shows the experimental total number density, n_{total} , for the amorphous and crystalline films as a function of x , as well as DFT calculated values. As x increases, the number density of the crystalline films (both the measured and DFT calculated values) decreases due to an increasing lattice constant. By contrast, the number density of the amorphous films is constant with composition and significantly lower than the crystalline films (13-17%).

Figure 4.7 shows the Fe K-edge Fourier transformed XAFS, $|\chi(R)|$, for the $\alpha\text{-Fe}_x\text{Si}_{1-x}$ samples, $x=0.45$ - 0.65 as indicated. The experimental data were analyzed in the k -range from 2 - 11 Å⁻¹. The prominent feature in these data is the peak located at approximately $R=1.85$ Å, which does not significantly shift as Fe concentration increases. However, a significant decrease in amplitude of this peak does occur with increasing Fe. Additionally, a small shoulder appears at approximately $R=2.35$ Å for the $x=0.45$ and $x=0.55$ compositions.

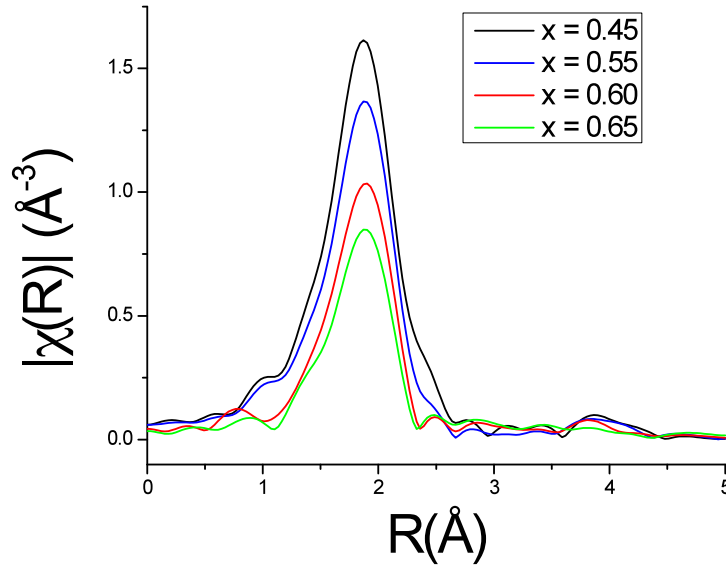


Figure 4.7. Fe K-edge Fourier transformed XAFS, $|\chi(R)|$, for amorphous $\text{Fe}_x\text{Si}_{1-x}$ samples.

Figure 4.8 shows the fit to the experimental X-ray absorption fine structure data, $\chi(R)$ and $\chi(k)$, for $x=0.45$. The R-range used in the fit was 1-3 Å. All the fits were of similar good quality. The number of first and second nearest neighbors around an Fe atom (N_{Fe-Fe}^1 , N_{Fe-Si}^1 and N_{Fe-Fe}^2), the first and second nearest neighbor mean square bond length disorder, ($[\sigma_{Fe-Fe}^1]^2$, $[\sigma_{Fe-Si}^1]^2$ and $[\sigma_{Fe-Fe}^2]^2$) and the first and second nearest neighbor distances (r_{Fe-Fe}^1 , r_{Fe-Si}^1 and r_{Fe-Fe}^2) are determined from the fits and are given in Table 4.1. For all compositions, the fitting routine yields only Si in the first shell if all parameters were allowed to vary. This result is consistent with DFT for $x=0.45$ and 0.55, but DFT showed a small number of Fe-Fe first nearest neighbors for $x=0.60$ and 0.65 (e.g. $N_{Fe-Fe}^1 = 2.1$ for $x=0.65$). We attribute the observed lack of Fe-Fe pairs in the fitting routine to bond length disorder. Since the modulation in X-ray absorption (XAFS signal) relies on constructive interference of backscattered photoelectrons from nearest neighbor atoms back to the original absorber, bond length disorder causes damping of the XAFS signal due to destructive interference from out of phase photoelectrons. To assess this, N_{Fe-Fe}^1 and r_{Fe-Fe}^1 were fixed in the first shell, and $[\sigma_{Fe-Fe}^1]^2$ was allowed to vary. As we fixed N_{Fe-Fe}^1 at higher values, $[\sigma_{Fe-Fe}^1]^2$ increased, indicating a range of possible coordination numbers with comparable fit quality. The variation in bond length ($\sqrt{[\sigma_{Fe-Fe}^1]^2}$) as N_{Fe-Fe}^1 increased was on the order of 0.25-0.26 Å, meaning the first and second shells were no longer distinct. Hence, the theoretical DFT calculations were used as guidance in selecting N_{Fe-Fe}^1 in the fit.

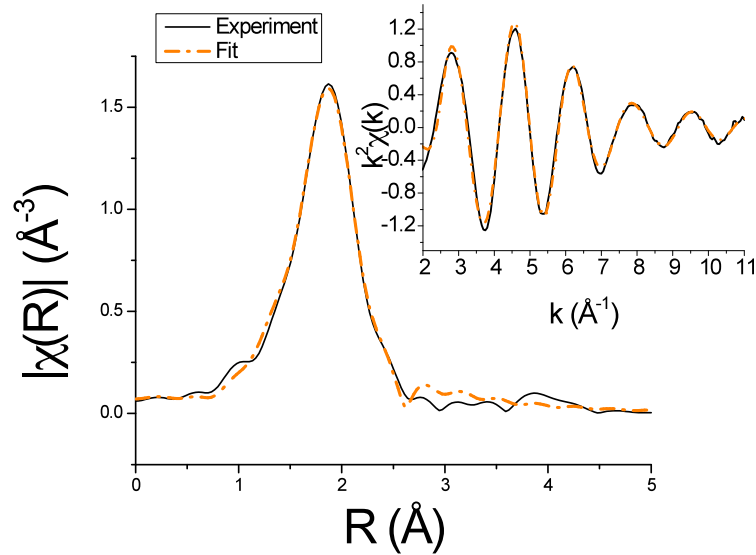


Figure 4.8. Fourier transformed XAFS $|\chi(R)|$ and fit for $x=0.45$. The inset is the XAFS in k-space, weighted by k^2 and the fit.

No Si second nearest neighbors around Fe (N_{Fe-Si}^2) were observed if all parameters were allowed to vary in the fitting routine. However, when the fitting routine was constrained to include Si in the second shell, it either yielded unphysical results (e.g. very large N_{Fe-Fe}^1).

Si) or did not converge, indicating that second shell Si does not contribute to the XAFS signal.

4.3.3. Electronic Structure and Spin Polarization

4.3.3.A. Theoretical DFT Calculations

Figure 4.9a displays the calculated electronic density of states, $D(E)$, for both up (\uparrow) and down (\downarrow) spins for various x in the amorphous structures, and Figure 4.9b shows $D(E)$ for the D0₃, B2, A2 and amorphous structures with compositions near $x=0.65$. Clear spin-splitting is observed in the amorphous bandstructures. Many of the sharp features in the B2 and D0₃ structures are broadened in the A2 and further broadened in the amorphous structure due to increasing disorder. The majority spin channel at E_F switches from spin up (D0₃, B2) to spin down (A2, amorphous), and the large dip in $D\downarrow(E_F)$ for the D0₃ and B2 structures is not present in the A2 or amorphous structures.

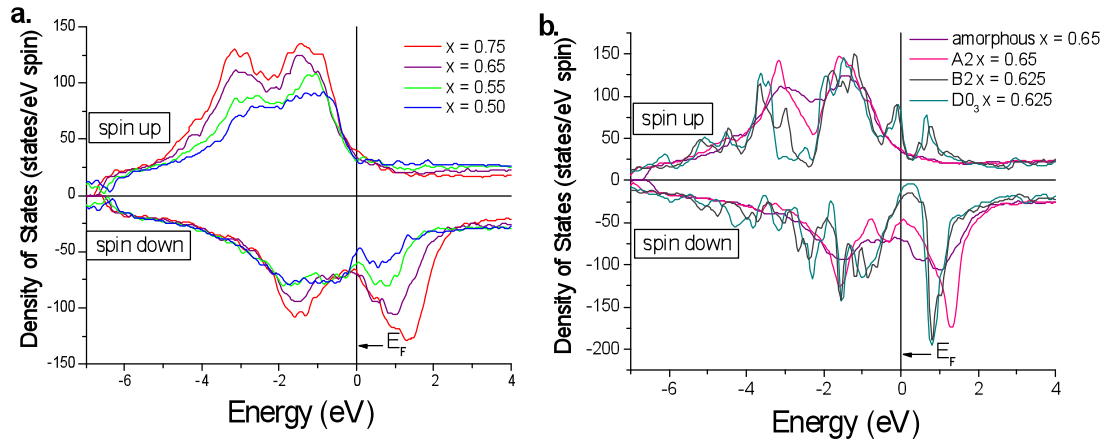


Figure 4.9. Calculated density of states (a) for the amorphous structures with various x and (b) for crystalline and amorphous structures near $x=0.65$.

Figure 4.10 shows M_{total} calculated from the difference between the integrated spin up and spin down channels below the Fermi energy (E_F) divided by the number of Fe and the spin polarization at E_F , $|P|$, for (a) the amorphous structures with various x and (b) the D0₃, B2, A2 and amorphous structures with $x \sim 0.65$. $|P|$ is defined as $|[D\uparrow(E_F) - D\downarrow(E_F)] / [D\uparrow(E_F) + D\downarrow(E_F)]|$. In Figure 4.10a, M_{total} increases with x , as shown in Figure 4.1. Figure 4.10b shows that the D0₃ and B2 structures have the smallest M_{total} , while the values for the A2 and amorphous structures are larger and similar, also as in Figure 4.1. $|P|$ in the amorphous structures is negative and does not significantly change with composition; $D\uparrow(E_F)$ is relatively insensitive to composition and $D\downarrow(E_F)$ changes slightly. The spin polarization in the amorphous material ($x=0.65$) is negative and remarkably larger than the A2 structure; it is nearly as large (although of the opposite sign) as the B2 structure, as indicated in Figure 4.10b.

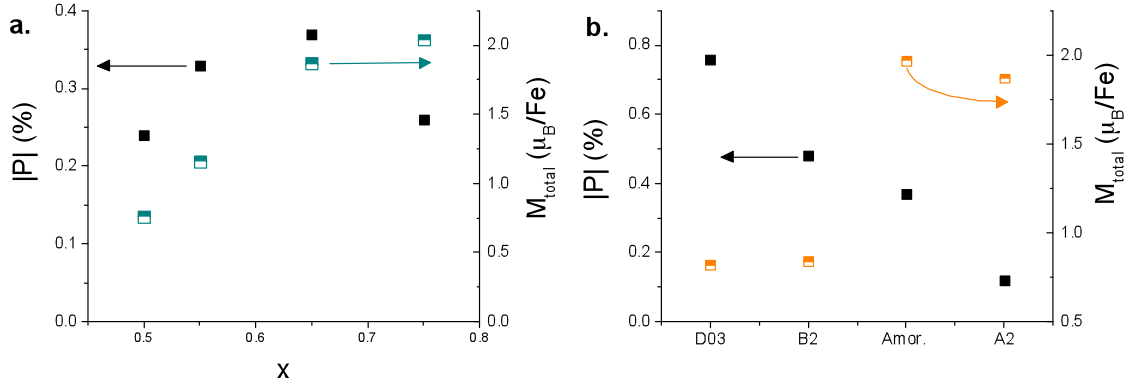


Figure 4.10. The absolute value of spin-polarization, $|P|$, at E_F (solid squares, left axis) and M_{total} (half open squares, right axis) for **(a)** the amorphous structures with various x and **(b)** crystalline and amorphous structures with $x \sim 0.65$. P is positive for D0₃ and B2 and negative for A2 and all amorphous structures.

4.3.3.B. Experimental Spin Polarization Measurements

Representative conductance curves for (a) small interfacial scattering factor, Z , and (b) large Z factor are shown in figure 4.11 for both amorphous and crystalline $x=0.65$ samples in contact with a Pb tip. The open symbols are experimental data, and the lines are the best fit using the Chen-Tesanovic-Chien (CTC) model, which describes the data well.⁹¹ An additional resistance (r_E), independent of the point contact resistance, which is due in part to the sample resistance, is taken into account in the fitting, based on the methods described in [92]. The values for the temperature and superconducting gap (Δ) are based on the experimental parameters; r_E , Z and P are determined by the fit. With similar Z , the conductance curve for the amorphous sample is much lower in magnitude than that of the crystalline, as shown in figure 4.11, indicating a much higher spin polarization. The spin polarization values, obtained from the fits to the conductance curves, are plotted as a function of Z in figure 4.12. The spin polarization decreases for increasing Z factor. For an ideal interface, P is independent of Z , however in reality the interfacial barrier always affects P .⁹¹ Hence, the intrinsic spin polarization is obtained by extrapolating the Z factor to zero. For the amorphous $x=0.65$ sample, P is $68.5 \pm 3.1\%$, and for the crystalline sample, the extrapolation gives $49.2 \pm 0.7\%$.

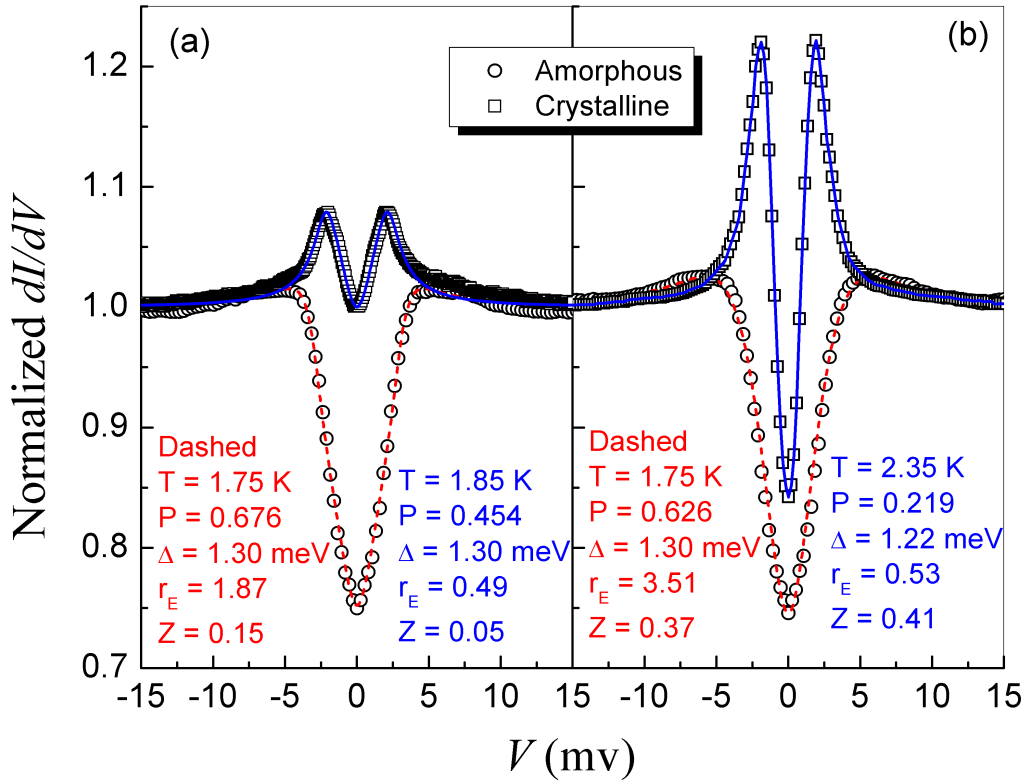


Figure 4.11. Representative conductance curves (with Pb tip) obtained from amorphous and crystalline $x=0.65$ samples with (a) small Z factor and (b) large Z factor. Open squares are experimental data for the crystalline sample; open circles are for the amorphous sample. The solid and dashed lines are the best fit to the data with the parameters listed in the inset.

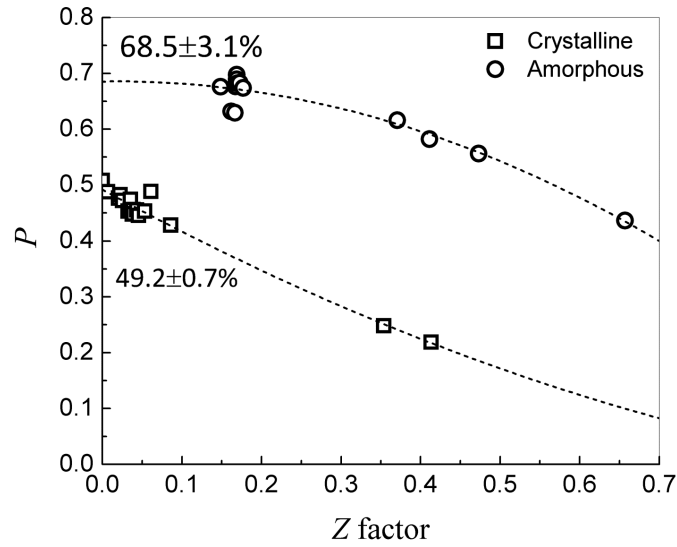


Figure 4.12. The spin polarization of crystalline (open squares) and amorphous (open circles) $x=0.65$ thin films as a function of Z factor. The dashed lines are a guide to the eye.

4.4. Discussion

The Si is significantly more structurally ordered than Fe in the amorphous system. The mean square bond disorder, $[\sigma_{Fe-Si}^I]^2$, is very low, almost an order of magnitude lower than for Fe. The Fourier transformed XAFS signal in figure 4.7 decreases with increasing Fe concentration, meaning ordered Si is contributing the most to the XAFS signal. A further indication of order is the presence of a second shell of Fe (for $x \leq 0.55$), corresponding to the shoulder at approximately $R=2.45 \text{ \AA}$ in figure 4.7. In the higher Fe concentration samples, the second shell is not observed in XAFS because disorder has completely damped the signal. Previous work on amorphous Si alloys has also reported distinct local environments since covalently bonded Si exhibits clear bond directions, and even in amorphous form, it will try to maintain bond lengths and directions that are close to equilibrium.⁹³

The Fe-Fe bond length (2.47 \AA) in the first shell for $x \geq 0.60$ is very close to the expected value for bcc crystalline Fe (2.49 \AA). However, the Fe-Si bond length ($2.33\text{-}2.35 \text{ \AA}$) is reduced compared to the values from crystalline Fe_xSi_{1-x} thin films (2.44 \AA $x=0.75$ and 2.39 \AA $x=0.55$). In fact, this bond length is much closer to the equilibrium Si-Si bond length, 2.35 \AA , further indicating Si is maintaining its equilibrium tetrahedral structure in the amorphous materials. The second shell Fe-Fe (2.70 \AA) bond length in $x=0.45$ and 0.55 is similar to the value in a crystalline $x=0.55$ sample (B2, CsCl structure), 2.76 \AA . In these samples, only Si is in the first shell, and the second shell is slightly further away and contains Fe. This structure is similar in interatomic spacing to a bcc material, where first nearest neighbors are located at $\sqrt{3}/2 a_0$, and the second nearest neighbors are not that much further away at a_0 . The distinct difference between these amorphous materials and a bcc structure is the reduced coordination number. The coordination number ranges between 3.7-4.5, which is much less than 8 in a bcc material. Theoretical DFT calculations find the coordination number actually ranges from 5-6.5, suggesting disorder is damping the experimental XAFS signal and causing a reduction in the observed coordination number. The structure in these materials is intermediate between CRN ($CN^I=4$) and dense random packing ($CN^I=8\text{-}12$).

The atomic density is significantly reduced (13-17%) compared to crystalline films, larger than is commonly seen, and is independent of x (unlike crystalline).^{94,95,96,97,98} The fact that theory and experiment agree indicates that the reduction in measured density of the amorphous films is not due to voids or columnar growth structure. CN^I for the amorphous structure is between 5 and 6.5, versus 8 in the crystalline bcc structure, a difference of about 18-30%, which could account for the large atomic density difference. Based on r_{Fe-Fe}^I and r_{Fe-Si}^I (theoretical and experimental) an approximately 3% decrease in n_{total} with increasing x would be expected, but CN^I slightly increases with increasing x , explaining why n_{total} remains constant.

Despite a reduced number density and coordination number, the magnetic moment is enhanced in the amorphous films, with both larger orbital and spin moments. The enhanced orbital moments are likely due to the lower local symmetry of the amorphous

phase compared to the crystalline phases. The chemically disordered A2 structure has more Fe-Fe pairs than the chemically ordered B2 or D0₃ structures, leading to a larger moment. The amorphous local environments (based on the fraction of Fe-Fe nearest neighbors, $N^1_{\text{Fe-Fe}}/\text{CN}^1$) are approximately intermediate between the chemically disordered A2 structure and the chemically ordered D0₃ or B2 structures; the amorphous materials, while structurally disordered, are only partially chemically disordered. This result is consistent with the local Fe coordination determined by XAFS and DFT theory for all x and by CEMS on amorphous and B2 samples with $x \sim 0.65$. The amorphous materials have a completely different structure; there are however more Fe-Fe pairs than the D0₃ or B2 structures (although less than A2), explaining the observed enhanced moment.

The electronic structure calculations reveal that $|P|$ is robust in the amorphous structures and is negative and comparable in magnitude to the B2 structure. It is larger by more than a factor of 3 than $|P|$ in the hypothetical A2 structure. Evidently, chemical order has a stronger influence on the spin-polarization than structural order. The D0₃ structure has the largest theoretical $|P|$. Remarkably, Andreev reflection measurements reveal that the spin polarization in the amorphous film is significantly larger than the epitaxial (B2) film ($x=0.65$). In fact, the amorphous $|P|$ is also larger than a previous report of the experimental spin-polarization in stoichiometric Fe₃Si with the D0₃ structure.⁹⁹

4.5. Conclusion

Structural and magnetic properties of amorphous and crystalline Fe _{x} Si_{1- x} thin films ($0.45 < x < 0.75$) were investigated. Both theoretical DFT calculations and X-ray absorption fine structure for the amorphous materials indicate a local atomic structure that is well-ordered for Fe-Si pairs and less ordered for Fe-Fe; calculated and experimental interatomic distances are similar to a bcc structure, however with a decreased coordination number. Experimental and theoretical number densities in the amorphous structures are less than in the crystalline phase. An enhanced magnetic moment due to enhanced spin and orbital moments was observed using X-ray magnetic circular dichroism for all amorphous films versus crystalline films of the same composition. This enhancement is found to be due to partial chemical disorder. Remarkably, the spin polarization in the amorphous films is robust and enhanced compared to the crystalline films.

Chapter 5: Hard X-ray Photoemission Spectroscopy (HAXPES) in $\text{Fe}_x\text{Si}_{1-x}$ Thin Films[†]

5.1 Introduction

Significant work has been devoted to Fe_3Si , but very little is known about non-stoichiometric alloys or amorphous alloys.^{14,100,101,102,103} In the composition range, $0.55 < x < 0.75$, a two-phase region of the bulk equilibrium phase diagram, thin film growth can be used to produce homogeneous alloys with varying degrees of structural and chemical ordering. This ordering affects the physical properties of the material, including in particular the electronic structure and magnetic properties, which can be significantly tuned. This work will investigate the role of composition as well as structural and chemical ordering on the electronic properties of homogeneous metastable $\text{Fe}_x\text{Si}_{1-x}$ samples.

For this study, we used hard x-ray photoelectron spectroscopy (HAXPS) to measure core and valence electronic levels for three $\text{Fe}_x\text{Si}_{1-x}$ samples: epitaxial $x=0.72$ (epi- $\text{Fe}_{0.72}\text{Si}_{0.28}$), epitaxial $x=0.67$ (epi- $\text{Fe}_{0.67}\text{Si}_{0.33}$), and amorphous (with some nanocrystals) $x=0.67$ (*a*- $\text{Fe}_{0.67}\text{Si}_{0.33}$). The first sample (epi- $\text{Fe}_{0.72}\text{Si}_{0.28}$) was chosen because $x=0.72$ is close to the Fe content of the stoichiometric alloy, so we expect a high degree of chemical and structural order. The second one (epi- $\text{Fe}_{0.67}\text{Si}_{0.33}$) was selected to study the effect of composition but not structural disorder, and the last one (*a*- $\text{Fe}_{0.67}\text{Si}_{0.33}$) to investigate the combined effects of composition and structural disorder on the electronic structure of these alloys.

X-ray photoelectron spectroscopy (XPS) has been used extensively to study chemical and electronic properties of Heusler alloys.^{31,32,33} However, due to the low inelastic mean-free path (IMFP) of the photoemitted electrons, conventional soft x-ray photoelectron spectroscopy (XPS) measurements are inherently surface-sensitive. This may result in spectra that are dominated by surface-effects, such as roughness, surface reconstruction, native oxides and contaminant layers, a serious deficiency if the bulk properties are of interest. By performing photoemission measurements in the hard x-ray regime, in this particular case at 5950.3 eV, we increase the IMFP of valence electrons by a factor of 4–7 for $\text{Fe}_{0.72}\text{Si}_{0.28}$, with the IMFP of 76 Å, as compared to IMFPs of 11–18 Å in the soft x-ray regime (500–1000 eV).^{34,35}

5.2 Experimental Methods

All films were prepared by electron beam co-evaporation of Fe and Si. The epitaxial samples were grown on MgO (001) at 300°C, and the amorphous sample was grown on amorphous SiN_x deposited on a Si substrate at room temperature. All samples were approximately 2000 Å thick. Compositions were measured using Rutherford

[†] This chapter has been adapted from previously published work: A.X. Gray *et al.* *Phys. Rev. B* **83** 195112 (2011).

Backscattering Spectrometry (RBS), and film thicknesses were determined with a KLA Tencor Alpha Step IQ profilometer. Compositions were also confirmed by analyzing HAXPS core-photoelectron relative peak intensities.

The atomic structure of the films was verified using transmission electron microscopy (α -Fe_{0.67}Si_{0.33}) and x-ray diffraction techniques (epi-Fe_{0.72}Si_{0.28} and epi-Fe_{0.67}Si_{0.33}). TEM results for α -Fe_{0.67}Si_{0.33} indicated partial crystallinity, and the volume fraction of the amorphous matrix was estimated to be on the order of 80%, with ~20% representing nanocrystalline areas. θ - 2θ x-ray diffraction patterns obtained from the epitaxial films indicated a single out-of-plane orientation in the films, and in-plane (ϕ) scans showed the expected four-fold symmetry, confirming epitaxy. From Conversion Electron Mössbauer Spectrometry (CEMS), the epitaxial $x=0.72$ sample is D0₃ while the epitaxial $x=0.67$ sample is B2.

Hard x-ray photoemission measurements were performed at the national synchrotron radiation facility SPring-8 in Japan, using undulator beamline BL15XU. The photon energy set at 5950.3 eV, which is the energy yielding optimal resolution and flux for that particular beamline. The exciting radiation was incident on the sample at a grazing angle of 2.0° as measured from the sample surface plane, and the kinetic energies of the photoemitted electrons were analyzed by a VG Scienta R4000 hemispherical analyzer oriented at an angle of 90° from the direction of the incoming x-rays. The electron takeoff angle as measured with respect to the surface is thus 88°, maximizing bulk sensitivity. Some measurements were also done at a takeoff angle of 45° to vary the degree of surface vs bulk sensitivity. The overall energy resolution was set to 230 meV, and the absolute energy scale was checked frequently against the Au Fermi level, so that the energy positions in all spectra have an accuracy of ± 10 meV.

5.3 Results and Discussion

5.3.1 Core-Level Spectra

Fig. 5.1 shows the Si 1s core-level spectra obtained for all three samples – epi-Fe_{0.72}Si_{0.28} (black), epi-Fe_{0.67}Si_{0.33} (red) and α -Fe_{0.67}Si_{0.33} (blue). The spectra have had a Shirley background subtracted from them, and the heights have been normalized to the maxima.¹⁰⁴ All three spectra show the presence of a chemically-shifted oxide component at ~1843 eV, but the shift is greater for the amorphous sample. No changes in the shape of the main elemental Si peak at a binding energy of ~1839.5 eV are observed between the three samples. However a chemical shift of 0.09 eV towards lower binding energy is observed for epi-Fe_{0.67}Si_{0.33} relative to epi-Fe_{0.72}Si_{0.28}, and an even more prominent shift of 0.31 eV towards lower binding energy is observed for the α -Fe_{0.67}Si_{0.33} sample, relative to epi-Fe_{0.67}Si_{0.33}. These shifts are due to a change in the chemical environment around the Si atoms. The variation in crystallinity of the alloy affects the chemical state of the Si atoms more strongly than the change in the alloy composition, *i.e.* the most significant chemical shift (0.31 eV) occurs between the epitaxial and amorphous alloys of similar composition (Fe_{0.67}Si_{0.33}). In addition, we do *not* observe significant disorder broadening

for the amorphous film, indicating that despite the amorphous structure, there is mostly a single chemical environment for Si in this film.

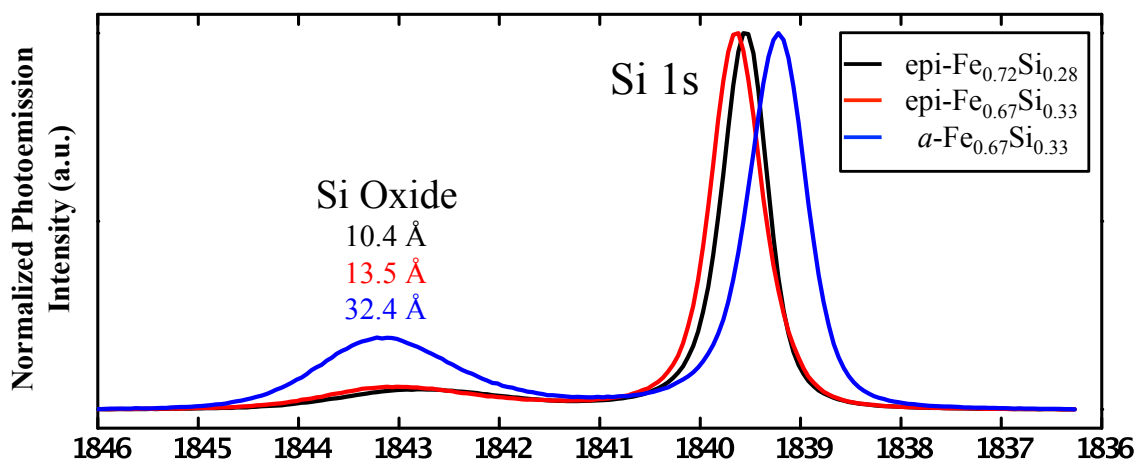


Figure 5.1. Si 1s core peak spectra obtained for all three samples – epi- $\text{Fe}_{0.72}\text{Si}_{0.28}$, epi- $\text{Fe}_{0.67}\text{Si}_{0.33}$ and $\alpha\text{-Fe}_{0.67}\text{Si}_{0.33}$.

The presence of Si oxide is evident due to the second Si 1s oxide peak that is separated from the elemental peak by about 3.3-3.9 eV.¹⁰⁵ This type of chemical shift is due to different chemical environments around Si atoms in the oxide and has been observed in numerous studies (e.g. 105,106). Similar behavior of elemental and oxide peaks is observed for the Si 2p peaks, shown later in this chapter. The intensity of the Si 1s oxide peak for the $\alpha\text{-Fe}_{0.67}\text{Si}_{0.33}$ sample is much higher compared to the epitaxial sample, suggesting a more pronounced oxidation in the amorphous alloy. The oxide thickness can be estimated by comparing the experimental and theoretical ratios of the Si oxide peak intensity to the main Si 1s core peak intensity. For this purpose, the NIST Database program Simulation of Electron Spectra for Surface Analysis (SESSA), which quantitatively predicts photoemission peak intensities, was used.¹⁰⁷ Assuming a single Si thin oxide overlayer, the effective oxide thicknesses for epi- $\text{Fe}_{0.72}\text{Si}_{0.28}$, epi- $\text{Fe}_{0.67}\text{Si}_{0.33}$ and $\alpha\text{-Fe}_{0.67}\text{Si}_{0.33}$ are 10.4 Å, 13.5 Å and 32.4 Å respectively; there is thus about three times as much oxidation for the amorphous sample. Angle-resolved measurements between a takeoff angle of 88° and 45° with respect to the surface, in conjunction with peak-intensity analyses, confirm that the oxide is localized at the surface of the samples.

The possible presence of any form of Fe oxide was investigated using the Fe 2p peaks shown in Fig. 5.2a. Oxidation of Fe has been reported to be accompanied by significant changes in the shapes and binding energies of the Fe 2p_{1/2} and Fe 2p_{3/2} peaks, and comparison between that report and the spectrum obtained here was used to determine the Fe oxidation state.¹⁰⁸ The spectrum in Figure 5.2a match the Fe⁰ spectrum reported in [108], meaning the Fe in our Fe_xSi_{1-x} samples was not significantly oxidized (less than 5%).¹⁰⁸

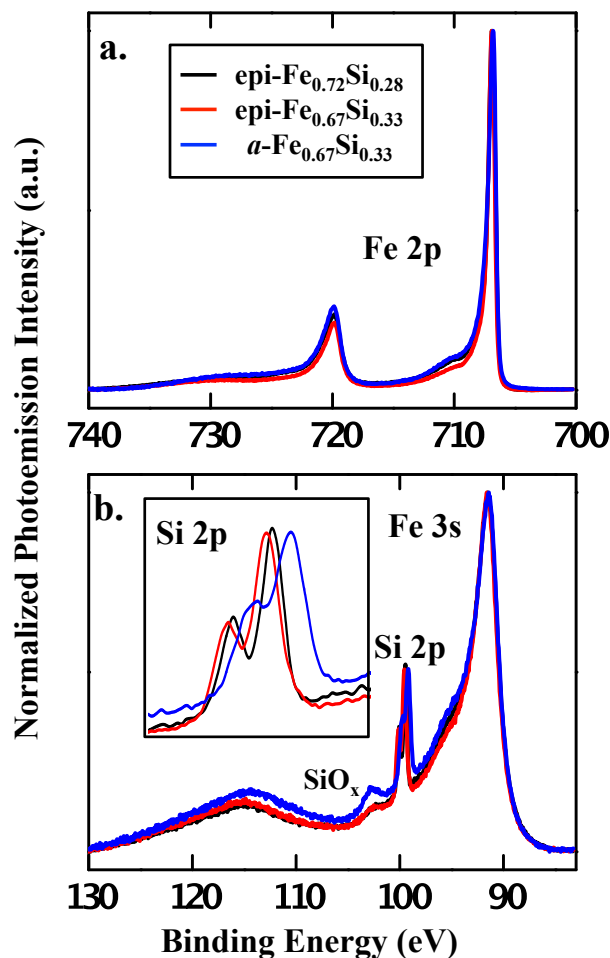


Figure 5.2. (a) Experimental Fe 2p spectra collected for all three samples, which do not exhibit any evidence of iron oxidation. (b) Fe 3s and Si 2p spectra obtained for all three samples. Fe 3s also does not show evidence of oxidation.

The Fe 2p peaks of all three samples are equally sharp, indicating sharply defined local environments in each. LDA calculations performed here predict 0.1-0.3 eV differences in the binding energies of Fe 2p core-levels due to the two different Fe sites (Fe_I and Fe_II). Since these values are comparable with the total experimental resolution (0.23 eV), clear splitting in the peaks cannot be observed. Such site-specific effects are more prominent in the valence-bands, where the electrons from Fe_I and Fe_II have stronger interactions with the different chemical environments of the two lattice sites due to their delocalized nature. This will be discussed in more detail in the next section.

Figure 5.2b shows the overlapping Fe 3s and Si 2p core spectra for all three samples. The spin-orbit splitting of the Si 2p peaks is well-resolved for the epitaxial samples and clearly visible for the amorphous sample (see inset), indicating only one type of Si chemical environment.¹⁰⁹ For the epitaxial films, this is consistent with the ordering observed in x-ray diffraction and CEMS; in both the D0₃ and B2 crystal structures, Si has

only one chemical environment for its nearest neighbors. Only the *next* nearest neighbors differ between the crystal structures, but this difference evidently does not produce a binding energy shift that is significant with respect to the spin-orbit splitting of 0.59 eV.¹⁰⁹ The spin-orbit splitting for the amorphous sample is clearly visible, although broadened and not as well-resolved as the epitaxial samples, also indicating a mostly single Si chemical environment.

5.3.2 Valance-Band Spectra

The broad spectra in figure 5.3(a) show the low-binding-energy valence features between 0 and 15 eV, seen in prior XPS measurements on Fe silicides, and a large peak centered at about 25 eV binding energy.¹¹⁰ With simple linear background subtraction, the latter feature can be decomposed into 4 peaks (Figure 5.3b), centered at 22.5 eV, 24.3 eV, 28.9 eV and 32.9 eV, but with a dominant peak (labeled P2) at 24.3 eV. The intensities of the P2 peaks correlate with the higher-binding energy components of the O 1s peaks (Si oxide peaks) to within 7%. Therefore, the dominant peak (P2) in the sub-valence feature corresponds to the photoemission from O 2s-dominated levels in the silicon-oxide layer.

Four prominent features labeled A, B, C, and D, which have also been observed in prior XPS studies, are shown in the low binding energy region of figure 6.3a.^{110,111,112} The spectral feature A exhibits a characteristic sharp peak for the epi-Fe_{0.72}Si_{0.28} and has also been observed in prior studies of stoichiometric Fe₃Si.^{111,112,113} This sharp peak disappears, however, as the Fe/Si ratio deviates from 3/1. The origin of these features will be discussed in the theoretical section below.

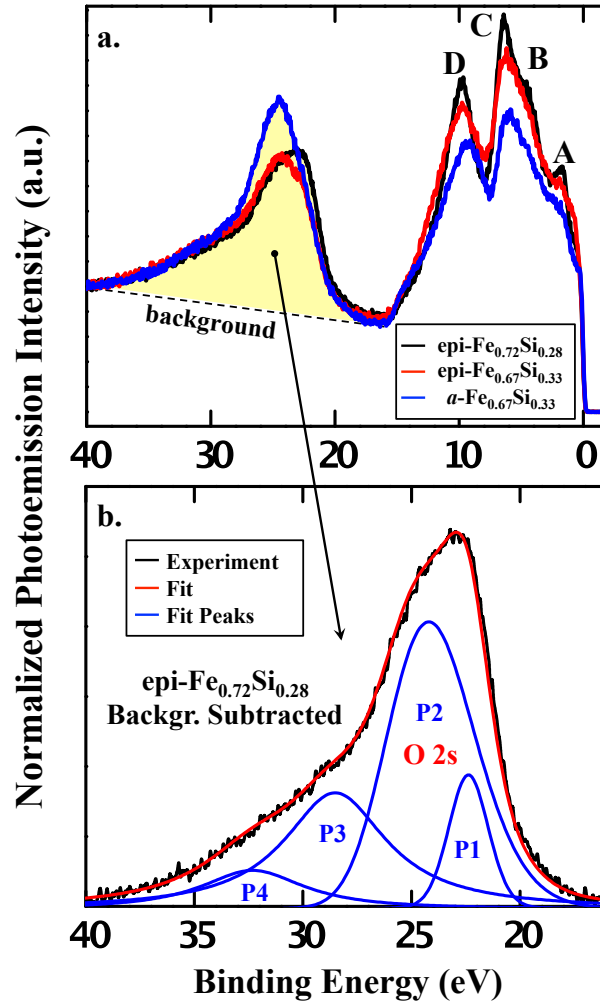


Figure 5.3 (a) Extended valence-band spectra obtained for all three samples, including the valence-band features labeled A-D and the sub-valence feature, later decomposed into four components (P1-P4), and normalized to the high-binding energy inelastic background tail. (b) Higher-binding energy valence feature, background-subtracted and fitted, with a dominant peak (P2) corresponding to the photoemission from O 2s levels in the SiO₂ layer.

5.3.3 Theoretical Analysis

First-principle calculations using the local-spin-density approximation (LSDA) of density functional theory within the spin-polarized fully relativistic Korringa-Kohn-Rostoker Green's function method (SPR-KKR) have been performed.^{114,115} The Vosko, Wilk, and Nusair parameterization was applied for the exchange and correlation potential.⁶⁵ The substitutional disorder has been treated within the coherent potential approximation (CPA).¹¹⁶ The CPA is considered to be the best approach among the so-called single-site (local) alloy theories that assume complete random disorder and ignore short-range order.

This scheme is implemented within the framework of the above mentioned SPR-KKR method. Self-consistent electronic structure calculations of the total and orbital-projected densities of states for three different compositions of $\text{Fe}_x\text{Si}_{1-x}$ were performed using the corresponding experimental lattice constant, e.g. for ordered Fe_3Si in the D0_3 structure ($a=5.63$ Å), for partially disordered $\text{FeFe}_{0.3}\text{Si}_{0.7}$ in the B2 structure ($a=2.79$ Å) and for chemically disordered bcc $\text{Fe}_{0.67}\text{Si}_{0.33}$ ($a=2.79$ Å). As a second step, actual valence-band photoemission spectra were calculated using a recent implementation of the fully relativistic CPA formalism in the framework of the one-step model of photoemission, which implicitly includes all matrix elements.^{117,118}

The calculated total densities of states are shown in figure 5.4 for three materials: D0_3 Fe_3Si , B2 $\text{Fe}_{0.67}\text{Si}_{0.33}$, and A2 $\text{Fe}_{0.67}\text{Si}_{0.33}$. The epi- $\text{Fe}_{0.72}\text{Si}_{0.28}$ sample has the D0_3 structure but deviates from the perfectly-ordered Fe_3Si compound used in the model because of being off-stoichiometry, and the A2 structure (random bcc solid solution) is used as an approximation for the amorphous sample. As expected, the sharp features observed in the densities of states (DOS) of the ordered Fe_3Si are smeared out by chemical disorder in the B2 and A2 structures.

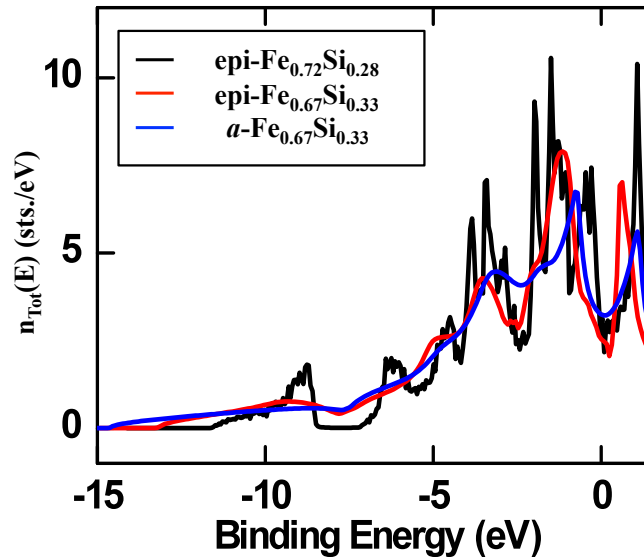


Figure 5.4. Total calculated densities of states for ordered D0_3 Fe_3Si (used as the model for epi- $\text{Fe}_{0.72}\text{Si}_{0.28}$), partially disordered $\text{FeFe}_{0.3}\text{Si}_{0.7}$ in the B2 structure (epi- $\text{Fe}_{0.67}\text{Si}_{0.33}$), and for chemically disordered bcc $\text{Fe}_{0.67}\text{Si}_{0.33}$, used for the amorphous $a\text{-Fe}_{0.67}\text{Si}_{0.33}$ sample.

Based on atomic subshell photoionization cross sections, the intensity distribution will be dominated by transitions involving initial sp-like Fe states in the hard X-ray regime.¹¹⁹ For this reason, complete photoemission calculations including all matrix element effects were performed. Figure 5.5 shows element- and site-resolved photoemission spectra of ordered Fe_3Si , calculated within the one-step model. The calculated KKR electronic-structure wave-functions were used in this calculation, and all matrix element effects

were included. Features A'-D' are present, much like in the experimental spectra. Feature A' is dominated by Fe_I, feature B' is dominated by Fe_{II}, feature C' is about 2/3 Fe_I and 1/3 Fe_{II}, and feature D' is dominated by Si. Comparing to the data in figure 5.3(a), the decreased intensity of peaks A and C between the two epitaxial samples is due to the decrease in Fe_I atoms due to Si substitution. Fe_I dominates the features close to the Fermi level (A, B and C), and these features are found to be the sp-like DOS of Fe_I (not shown here). Due to strong hybridization of the Fe sp-like states with the Fe 3d states, the changes in the observed spectral intensities of the sp states, which dominate the valence-band spectra due to their high photoionization cross sections, can be directly related to the behavior of the Fe 3d states.

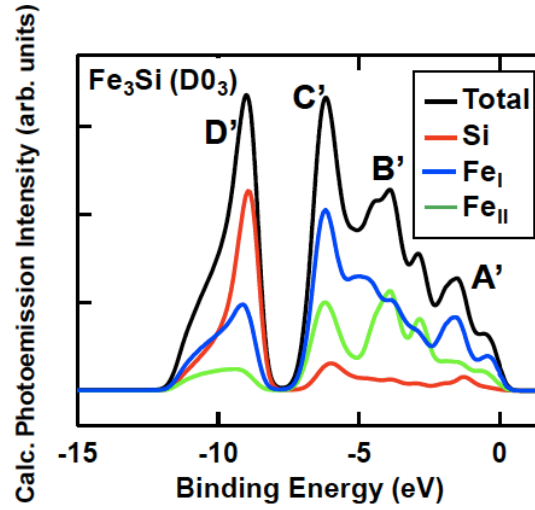


Figure 5.5. Calculated element- and site- resolved angle-integrated XPS spectra for ordered D0₃ Fe₃Si (used to model epi-Fe_{0.72}Si_{0.28}), including 230 meV broadening due to the total experimental resolution.

Finally, figure 5.6 compares the experimental valence spectra for the three materials to angle-integrated valence-band photoemission calculations at 5950.3 eV. Good agreement with the experimental data is obtained. In particular, most features are correctly predicted with regard to position, width, and relative intensity for the epi-Fe_{0.67}Si_{0.33} and *a*-Fe_{0.67}Si_{0.33} samples. All features A-D for epi-Fe_{0.72}Si_{0.28} are also predicted, but peak D (due to the Si 3s states) is predicted to be at lower binding energy (by about 1 eV) than observed experimentally. This result is due to the sample being more Si-rich than the stoichiometric Fe₃Si in the model. Moreover, the calculated spectrum exhibits much sharper features than the experimental one, also due to the disorder broadening from the excess Si of epi-Fe_{0.72}Si_{0.28}.

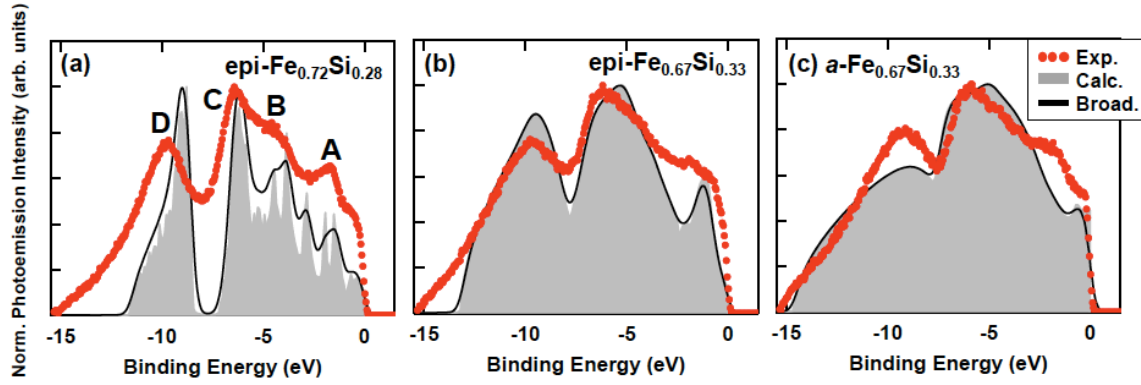


Figure 5.6. Room temperature XPS spectra for (a) ordered $D0_3$ Fe_3Si (used to model epi- $\text{Fe}_{0.72}\text{Si}_{0.28}$), (b) partially disordered $\text{FeFe}_{0.3}\text{Si}_{0.7}$ in the $B2$ structure (used to model epi- $\text{Fe}_{0.67}\text{Si}_{0.33}$), and (c) chemically disordered bcc $a\text{-Fe}_{0.67}\text{Si}_{0.33}$ at a photon energy of 5950.3 eV compared to calculated one-step theoretical spectra shown in grey. The black curves represent a broadening of the theoretical spectra with a 230 meV (FWHM) Gaussian to simulate the experimental resolution. Experimental data, normalized to the high-binding energy inelastic background tail are shown in red.

Remarkably, the D (Si) peak for the amorphous sample is sharper than that for the calculated random crystalline (A2) alloy, suggesting that the amorphous structure possesses on average a better defined local structure around the Si atoms than a random alloy. Also, the amorphous sample shows a clear sign of an A peak, not seen in the random alloy calculations. Better modeling of the amorphous structure is required in order to say more. Despite some minor discrepancies, these one-step photoemission calculations provide a good qualitative description of the data.

5.4 Conclusion

We have investigated the structural and electronic properties of near-Heusler epitaxial and amorphous $\text{Fe}_x\text{Si}_{1-x}$ thin films with $x=0.72$ and $x=0.67$ using hard x-ray photoelectron spectroscopy. Remarkably, the core-level peaks in the amorphous structure show little broadening despite a significant energy shift, suggesting that the local environment around the Si atoms is different than in the crystalline materials but far more uniform than expected. A well-resolved Si 2p spin-orbit splitting for the two epitaxial alloys suggests that nearest-neighbor interactions are the dominant effect on binding energy for the Si atoms in the sample. The Si 2p peak in the amorphous sample also shows spin-orbit splitting, another indication that the local structure around each Si atom is relatively well defined. The valence bands show a broadening of the features when chemical and structural disorder is increased. Distinctly different contributions from the two inequivalent Fe sites in the valence-band spectrum of the most highly ordered ($D0_3$) epitaxial sample is observed. These features are reduced but not completely eliminated in the $B2$ sample and most remarkably for the amorphous sample. Lastly, CPA calculations of the valence band photoemission spectra have been performed and show good

agreement with the experimental spectra, thus confirming the origin of the observed features.

Chapter 6: Electronic Transport and the Anomalous Hall Effect (AHE) in $\text{Fe}_x\text{Si}_{1-x}$ Thin Films

6.1 Introduction

The origin of the Anomalous Hall effect (AHE) in ferromagnetic materials remains controversial, but recently a unified theory has been proposed.^{43,44} The theory generally splits the anomalous Hall conductivity (σ_{xy}) into three regions based on the longitudinal conductivity (σ_{xx}). In the clean limit ($\sigma_{xx} > 10^6 \Omega^{-1}\text{cm}^{-1}$) at low temperatures, the skew-scattering mechanism, which is due to asymmetric spin scattering from impurities with spin-orbit coupling, dominates, and $\sigma_{xy} \propto \sigma_{xx}$.^{44,45,46} In the second regime ($10^4 \Omega^{-1}\text{cm}^{-1} < \sigma_{xx} < 10^6 \Omega^{-1}\text{cm}^{-1}$), the intrinsic mechanism is the dominant contribution to σ_{xy} . The intrinsic contribution is associated with interband spin-orbit coupling that causes a gap to open at band anti-crossing points in the electronic band structure. If the Fermi energy lies near these points, a large Berry phase curvature will occur, significantly enhancing σ_{xy} .^{44,48} In this regime, $\sigma_{xy} = \text{constant}$. Although it may be counterintuitive that the skew-scattering mechanism dominates in a σ_{xx} range with fewer impurities and the intrinsic contribution dominates in a regime with more, the intrinsic contribution is actually independent of the carrier lifetime, τ , while the skew-scattering mechanism is not. So skew-scattering will always dominate when τ is large, as in the clean limit. Numerous experimental results have verified the dependences of the anomalous Hall conductivity in these two regimes for e.g. Fe, Co, Ni, and Gd.^{49,50,51} The low conductivity regime ($\sigma_{xx} < 10^4 \Omega^{-1}\text{cm}^{-1}$, $\rho_{xx} > 100 \mu\Omega\text{cm}$) is less well understood. Experimental results from ultrathin Fe^{52} , chalcogenide-spinel structures ($\text{Cu}_{1-x}\text{Zn}_x\text{Cr}_2\text{Se}_4$)⁵⁰, Fe_3O_4 and $\text{Fe}_{3-x}\text{Zn}_x\text{O}_4$ ⁴⁷ show $\sigma_{xy} \propto \sigma_{xx}^n$ where $1.6 < n < 1.8$. It has been suggested that the observed behavior is due to a gradual decrease in the intrinsic effect due to disorder, however there is no theory to support this scaling.⁴⁴ Conventionally, σ_{xy} is plotted against σ_{xx} , however the carrier concentration seems the more relevant parameter in this regime.

Experimental work on the canonical dilute magnetic semiconductor, $\text{Ga}_{1-y}\text{Mn}_y\text{As}$ by Chun *et al.* in the low σ_{xx} regime showed that variations in the carrier concentration can be used to change the Curie temperature, magnetization (M), the sign of the temperature coefficient of resistivity, α (metallic to insulating) and most importantly the origins of the AHE.¹²⁰ The magnitude of σ_{xy}/M_z was larger than other materials, although consistent with theoretical predictions for ferromagnetic semiconductors.^{120,121} Metallic samples showed an intrinsic AHE (also verified by [122]), while more insulating samples ($\rho_{xx} > 10 \text{ m}\Omega\text{cm}$) display a linear scaling in σ_{xy}/M_z with σ_{xx} , which was attributed to unspecified extrinsic origins.

Here, we study the AHE and M at 2 K in a series of amorphous and epitaxial $\text{Fe}_x\text{Si}_{1-x}$ thin films ($0.45 < x < 0.71$), where the hole carrier concentration (n_h) is varied. We find $\sigma_{xy}/M_z \propto \sigma_{xx}$, similar to the GaMnAs results of ref. 120 although in a limit of much higher carrier concentration and disorder, and do *not* find the scaling relation $\sigma_{xy} \propto \sigma_{xx}^n$ ($1.6 < n < 1.8$).

We suggest the scaling in the low σ_{xx} regime is dominated by dependence on the number of carriers.

6.2. Experimental Procedure

$\text{Fe}_x\text{Si}_{1-x}$ ($0.43 < x < 0.71$) thin films (70-100 nm thickness) were grown by electron-beam co-evaporation of Fe and Si at base pressures below 9.0×10^{-9} Torr. Films were grown both at room temperature and 300°C on both MgO and amorphous- SiN_x on Si substrates. The structure of all films was measured using x-ray diffraction (XRD), conversion electron Mössbauer spectrometry and high-resolution cross-section transmission electron microscopy (HRXTEM). The films with $x=0.71$ and $x=0.67$ grown at 300°C on MgO were found to be epitaxial with the D0_3 and B2 structure respectively. θ - 2θ scans show 100 out-of-plane orientation and azimuthal (ϕ) scans on the off-axis 110 peak show the expected four-fold symmetry. For films with $x=0.43$ -0.71 grown at room temperature on SiN_x/Si substrates, no peaks were observed in XRD. HRXTEM was performed on two samples, $x=0.55$ and 0.67. The bright field TEM image from $x=0.67$ (figure 2.5) displayed a predominantly amorphous structure (80% volume fraction) with some embedded nanocrystals (~20% volume fraction) on the order of 5 nm. The bright field HRXTEM image from the $x=0.55$ sample (figure 2.6) displayed no such nanocrystallinity. In a few places, poorly defined lattice fringes were observed suggesting nanocrystal precursors (diameter < 2nm) form and increase (in size and number) with increasing Fe concentration. Samples with $x \geq 0.67$ are therefore considered partially crystalline and samples with $x < 0.67$ amorphous.

Samples were patterned into a Hall bar (40 μm x 120 μm) with 6 current-voltage (I - V) leads using standard photolithography and wet etch techniques for the Hall effect, magnetoresistance and resistivity measurements. Hall effect measurements were performed between 2 K and 300 K using an ac lock-in technique at approximately 16 Hz, with I kept below 2 μA . Four-point dc-resistivity measurements as a function of temperature (T) and magnetic field (H) were also performed. Magnetization (M) as a function of T and H was measured using a Quantum Design SQUID MPMS.

6.3 Results and Discussion

Figure 6.1a shows a plot of longitudinal resistivity (ρ_{xx}) as a function of temperature for a set of films (epitaxial or amorphous) with different compositions x . The epitaxial films display behavior expected for a typical metal: increasing ρ_{xx} with increasing temperature, *i.e.* a positive temperature coefficient of resistivity (α) at all T . Here α is defined in $\rho_1 = \rho_{\text{ref}} [1 + \alpha(T_1 - T_{\text{ref}})]$ where ρ_1 and ρ_{ref} are the resistivities at $T_1 = 10$ K and $T_{\text{ref}} = 300$ K. $\rho_{xx}(T)$ for the amorphous films is almost T -independent but depends strongly on x . For these films, the mean free path is approximately equal to an interatomic distance and thus nearly temperature independent, leading to a small α . Figure 6.1b is a plot of α versus ρ_{xx} at 2 K for the amorphous and partially crystalline films; α changes sign from positive to negative with increasing x . This behavior has been studied in numerous amorphous

metallic systems where α has been shown to correlate linearly with ρ_{xx} .³⁸ In the present data, α crosses from positive to negative at approximately 150 $\mu\Omega\text{cm}$, typical for amorphous metals.³⁹ The dependence of ρ_{xx} on x and its independence of T indicates that the number of charge carriers decreases as x decreases, as would be expected. In the $x=0.43$ sample, a clear minimum in ρ_{xx} is observed; this minimum is also present in the $x=0.45$ sample. A resistivity minimum can result from a Kondo effect, resonant impurity scattering or insulating grain boundaries (unlikely here since ρ_{xx} does not show an exponential T dependence).¹²³

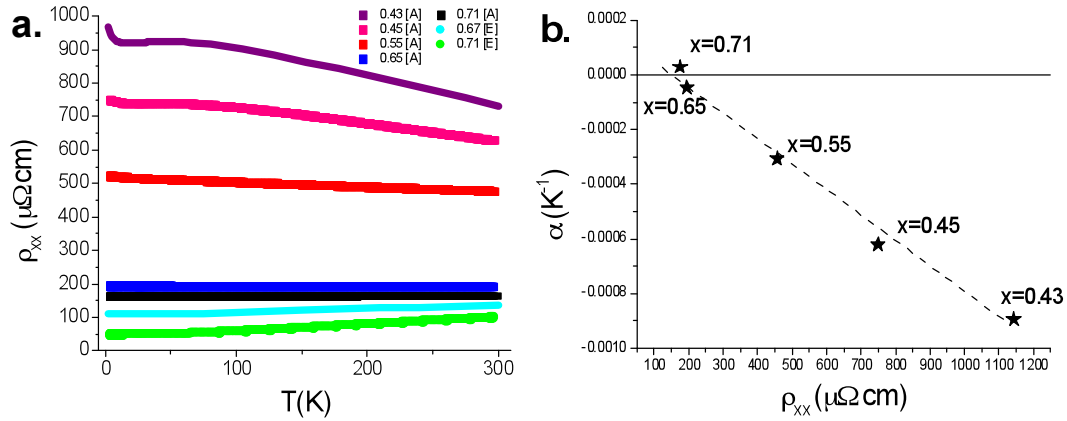


Figure 6.1. (a) Resistivity versus temperature for amorphous films [A] and epitaxial films [E] of varying x . **(b)** Temperature coefficient of resistivity, α , versus longitudinal resistivity, ρ_{xx} , at 2 K for amorphous and partially crystalline films. The line is a guide to the eye.

Figure 6.2 shows in-plane $M(H)$ curves at 2 K for amorphous and epitaxial films with various x ; the inset displays the two lowest Fe concentration amorphous samples on a different scale. Square hysteresis loops are observed for all $x \geq 0.55$, indicating the samples are ferromagnetic. For a given x , M is larger in the amorphous film than the crystalline film. Chemical order in the epitaxial film leads to less Fe-Fe pairs and thus a reduction in M . Further details of this result have been discussed in Chapter 4. We find ferromagnetism occurs in the amorphous $\text{Fe}_x\text{Si}_{1-x}$ system at $x \sim 0.40$, consistent with previous work⁸⁸; the amorphous samples with $x=0.43$ and 0.45 are very near this critical composition, explaining the different shape of the $M(H)$ curves. However, magnetic remanence and an M value at all H larger than what would be expected for a Brillouin function ($S=1/2$, 1 or $3/2$) are observed, indicating that these samples are weakly ferromagnetic. The in-plane and out-of-plane $M(H)$ curves are not significantly different for the amorphous $x=0.43$ and 0.45 samples.

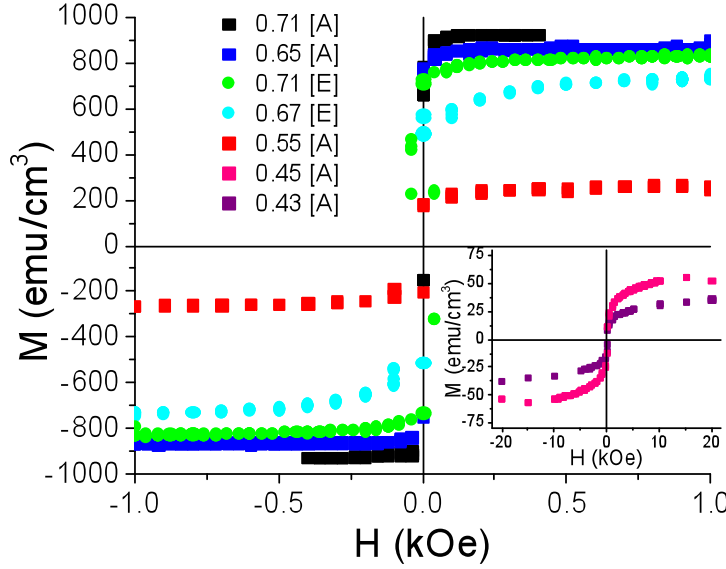


Figure 6.2 In-plane magnetization versus field at 2 K for amorphous [A] and epitaxial [E] films of varying x . The inset in shows $M(H)$ of amorphous $x=0.43$ and 0.45 films on an expanded y-scale. The temperature-independent diamagnetic contribution (visible at high fields, same for H in-plane or out-of-plane) has been removed from all the data.

Magnetoresistance (MR) measurements, $\Delta\rho_{xx}$, [$\Delta\rho_{xx}=\rho_{xx}(H)-\rho_{xx}(0)$] with (a) H applied perpendicular to the film and to the current I , (b) H applied in the film plane and parallel to I and (c) H in the film plane and perpendicular to I were performed at various T on the lowest Fe concentration sample, $x=0.43$ and are shown in Figure 6.3. The contacts were not removed between measurements; only the orientation of the sample with respect to the H and I changed. The magnitude of the MR is small; data for (b) and (c) are the same and differ from (a) (H applied out-of-plane) at all T . At 16 and 30 K, all MR shows a positive H^2 dependence, typical for metals [18]. At 2 K, the out-of-plane MR is negative, and the in-plane MR switches from negative to positive with increasing H . Orbital effects are not the dominant mechanism since (b) and (c) are the same and (a) and (c) differ. Additionally, the out-of-plane and in-plane $M(H)$ data are not significantly different for this sample, indicating that the differences in MR are not due to different $M(H)$ behavior. Similar negative MR has been previously reported at low temperature (below some critical temperature T^*) in amorphous $\text{Gd}_x\text{Si}_{1-x}$ alloys ($x<0.15$) and attributed to interactions between local moments and conduction electrons; similar to (b) and (c) at 2 K, a switch from negative to positive MR was also observed, although at much higher field (~ 25 T).^{124,125,126,127} The different behavior of the 2 K MR between H applied in-plane and out-of-plane was not observed in amorphous $\text{Gd}_x\text{Si}_{1-x}$, however the difference observed here is extremely small in comparison to the enormous MR reported in $\text{Gd}_x\text{Si}_{1-x}$.

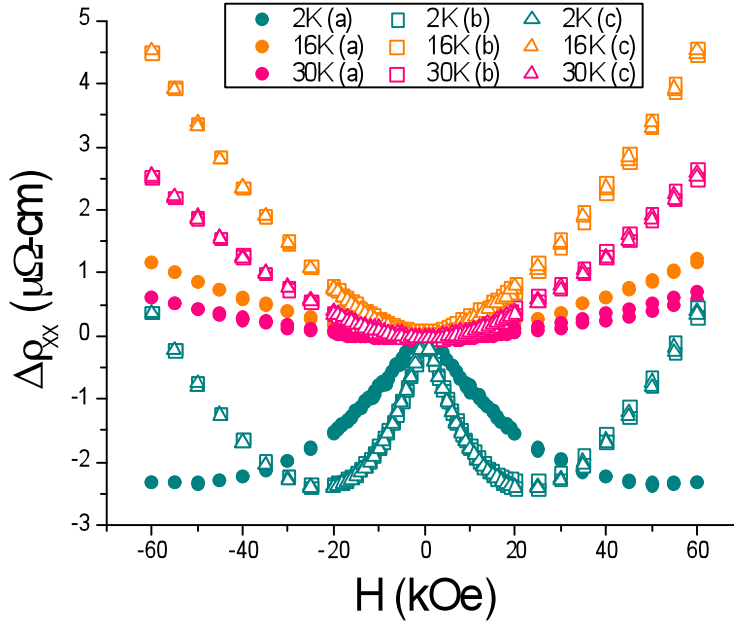


Figure 6.3. Magnetoresistance, $\Delta\rho_{xx}$, [$\Delta\rho_{xx}=\rho_{xx}(H)-\rho_{xx}(0)$] versus applied field with (a) H applied perpendicular to the film and I , with (b) H applied in the film plane and parallel to I and with (c) H in the film plane and perpendicular to I at various T for amorphous $x=0.43$.

The magnetic field dependence (H applied perpendicular to the film plane) of the transverse resistivity (ρ_{xy}) at 2 K is shown in Figure 6.4. The Hall effect in ferromagnetic materials has two contributions, one from the ordinary Hall effect (OHE) due to the Lorentz force, which is proportional H and one from the AHE due to asymmetric scattering, which is proportional to the perpendicular component of M (M_z). The equation describing this effect takes the form:

$$\rho_{xy}(\text{total}) = \rho_{xy}(\text{OHE}) + \rho_{xy}(\text{AHE}) = R_o H + R_s M_z \quad (6.1)$$

Here, R_o is the ordinary Hall coefficient ($R_o = \pm 1/ne$), and R_s is the anomalous Hall coefficient. The magnitude of the AHE is many times larger for the amorphous films than the epitaxial films with the same or similar compositions, an effect also seen in previous transport studies at low temperature of vapor-quenched Fe.²⁴ ρ_{xy} was also here measured at higher T (*i.e.* 16, 30, 300 K) for some samples; the magnitude of ρ_{xy} decreased compared to the 2 K value, quantitatively consistent with its scaling with M_z .

From $\rho_{xy}(H)$ above 1.5 T (where $M(H)$ has saturated) the ordinary Hall effect can be used to determine carrier concentration. The positive slope of $\rho_{xy}(H)$ shows that the primary charge carriers are holes. For $x=0.43$ and 0.45, R_o gives the number of holes, n_h , as approximately $5 \times 10^{21} \text{ cm}^{-3}$ at 2 K. For higher x , $\delta\rho_{xy}/\delta H$ is too small to measure,

meaning that $n_h > 10^{22} \text{ cm}^{-3}$. For $x > 0.45$, a linear extrapolation of n_h was made based on reported values for $x=1.0$ and 0.75 .^{128,129}

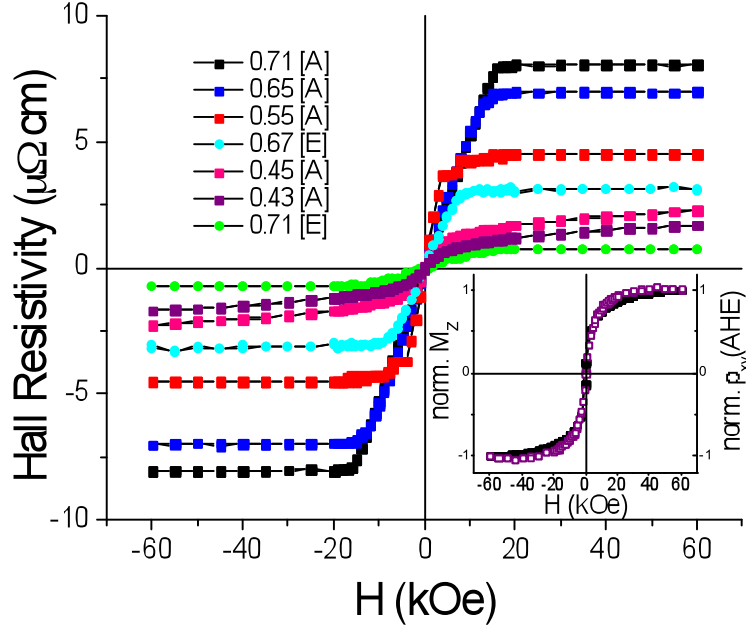


Figure 6.4. Hall Resistivity ρ_{xy} vs H at 2 K for amorphous [A] and epitaxial [E] films of various x . $\rho_{xy}(H) \propto M_z(H)$ for all samples. For $x=0.43$ and 0.45 , a small additional contribution to $\rho_{xy}(H)$ due to the ordinary Hall effect can be seen. The inset shows normalized out of plane magnetization (black squares) and normalized $\rho_{xy}(\text{AHE})$ (purple squares) at 2K for $x=0.43$. $\rho_{xy}(\text{OHE})$ has been subtracted from the data.

The inset of figure 6.4 shows normalized out of plane magnetization (left axis, black squares) and normalized $\rho_{xy}(\text{AHE})$ (right axis, purple squares) for the $x=0.43$ sample. The slope due to the ordinary Hall effect has been removed from $\rho_{xy}(\text{total})$ to show that the AHE scales with M_z . Similar behavior was observed for all samples (see Appendix A). Hysteresis in $M_z(H)$ or $\rho_{xy}(H)$ is not observed in any samples; for $x \geq 0.55$, the magnetic easy axis is in the plane of the film, and $x=0.43$ and 0.45 are weakly ferromagnetic with similar in-plane and out-of-plane $M(H)$ curves (see Appendix B).

The anomalous Hall conductivity is calculated from $\sigma_{xy}(\text{AHE}) = \rho_{xy}(\text{AHE}) / (\rho_{xx}^2 + \rho_{xy}(\text{AHE})^2) \sim \rho_{xy}(\text{AHE}) / \rho_{xx}^2$.⁴⁷ $\rho_{xy}(\text{AHE})$ is obtained by extrapolating $\rho_{xy}(\text{total})$ to zero field. Since $\sigma_{xy}(\text{AHE}) \propto \rho_{xy}(\text{AHE})$, both are $\propto M_z$, and indeed the relation ($\sigma_{xy}(\text{AHE}) \propto M_z$) has been seen in itinerant ferromagnets and magnetic semiconductors, although not observed in heavy fermion systems.⁶³ Figure 6.5 (a) is a plot of σ_{xy}/M_z versus σ_{xx} at 2K for the $\text{Fe}_x\text{Si}_{1-x}$ thin films investigated and a series of $\text{Ga}_{1-y}\text{Mn}_y\text{As}$ samples at 15 K from [120]. We plot σ_{xy}/M_z versus σ_{xx} to interpret the underlying mechanisms in our AHE data based on the theoretical scaling proposed by [43,44]; the different scaling behaviors are

not as obvious when plotting ρ_{xy}/M_z versus ρ_{xx} . The epitaxial samples display a $\sigma_{xy}/M_z =$ constant while the lower σ_{xx} amorphous samples show $\sigma_{xy}/M_z \propto \sigma_{xx}^{1.3}$.

We first discuss the epitaxial samples. In principle, there are two mechanisms, which could give rise to a $\sigma_{xy}/M_z = \text{constant}$: the intrinsic mechanism and the side-jump mechanism. The side-jump mechanism has a much smaller contribution to the AHE in this σ_{xx} regime ($10^4 \Omega^{-1}\text{cm}^{-1} < \sigma_{xx} < 10^6 \Omega^{-1}\text{cm}^{-1}$), and Miyasato, *et. al.* has shown that if $\sigma_{xy} \sim 10^3 \Omega^{-1}\text{cm}^{-1}$, the effect is dominated by the intrinsic mechanism, as in our epitaxial samples.⁵⁰ This result is in agreement with theory and previously reported values where the intrinsic mechanism is dominant to $\sigma_{xx} \sim 10^4 (\Omega\text{-cm})^{-1}$.⁴³

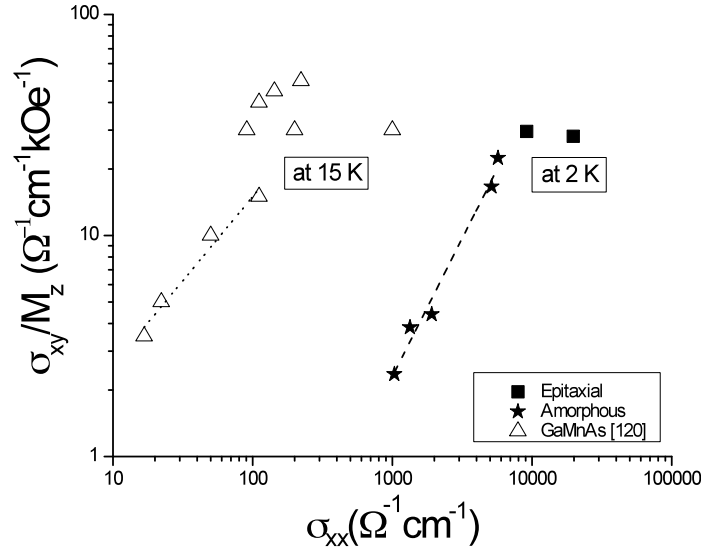


Figure 6.5. σ_{xy}/M_z versus σ_{xx} for amorphous and epitaxial $\text{Fe}_x\text{Si}_{1-x}$ thin films and GaMnAs thin films from [120]. The lines are fits to the low σ_{xx} data; $\sigma_{xy}/M_z \propto \sigma_{xx}^n$ with $n=1.3$ ($\text{Fe}_x\text{Si}_{1-x}$) and 0.8 ($\text{Ga}_{1-y}\text{Mn}_y\text{As}$).

The scaling behavior in the low conductivity regime of the amorphous samples was suggested to be due to the damping of the intrinsic contribution with increased disorder, and to result in $\sigma_{xy} \propto \sigma_{xx}^{1.6-1.8}$, however no rigorous theory exists to support this suggestion.^{43,44,47,50,52} If we plotted σ_{xy} versus σ_{xx} , the scaling behavior would be $\sigma_{xy} \propto \sigma_{xx}^{3.1}$, a significantly different dependence. When the data is instead normalized by M_z , we observe $\sigma_{xy}/M_z \propto \sigma_{xx}$ ($\sigma_{xy}/M_z \propto \sigma_{xx}^{1.3}$ to be precise).

We compare these results to the work of Chun *et al.* on $\text{Ga}_{1-y}\text{Mn}_y\text{As}$.¹²⁰ By varying n_h , the authors change the AHE from an intrinsic (metallic) regime with $\sigma_{xy}/M_z = \text{constant}$ to an insulating regime with $\sigma_{xy}/M_z \propto \sigma_{xx}$. Similarly, in the work presented here, the intrinsic mechanism is dominant in the epitaxial (metallic) films, and the scaling is approximately linear with decreasing σ_{xx} in the amorphous films.

In our $\text{Fe}_x\text{Si}_{1-x}$ films and the $\text{Ga}_{1-y}\text{Mn}_y\text{As}$ films, we find the approximate dependence $\sigma_{xx} \propto n_h^{2/3}$, as shown in figure 6.6 (in the amorphous $\text{Fe}_x\text{Si}_{1-x}$ films this dependence could naively be expected from $\sigma_{xx} = [n^{2/3}e^2l]/[\hbar(3\pi^2)^{1/3}]$ since the mean free path, l , is roughly constant[‡]). Normalizing σ_{xy}/M_z and σ_{xx} by $n_h^{2/3}$ for both of these material systems produces a constant value (figure 6.7), suggesting that the AHE in the low conductivity regime scales with $n_h^{2/3}$. This similarity in scaling near the metal-insulator transition in these two materials persists despite the greater disorder and much higher n_h (2 orders of magnitude) in the $\text{Fe}_x\text{Si}_{1-x}$ thin films, which causes σ_{xx} to be much larger as well.

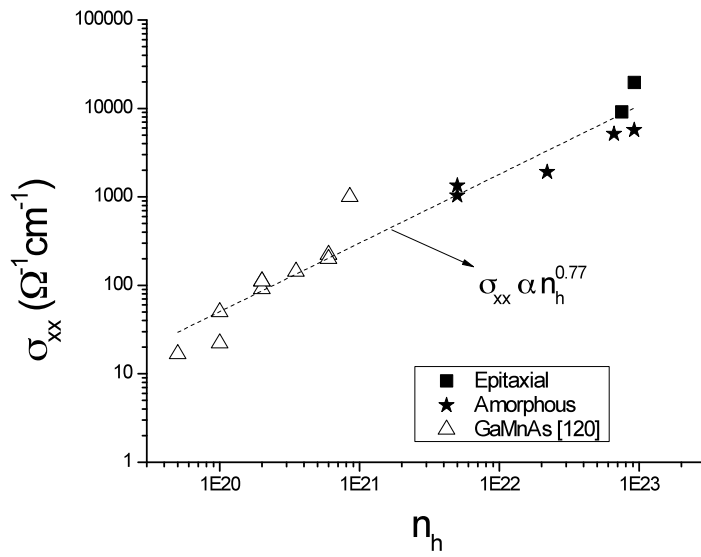


Figure 6.6. σ_{xx} versus n_h , with the relationship $\sigma_{xx} \propto n_h^{0.77}$ for the amorphous and epitaxial $\text{Fe}_x\text{Si}_{1-x}$ thin films at 2 K and $\text{Ga}_{1-y}\text{Mn}_y\text{As}$ at 15 K from ref [120].

[‡] This dependence can be obtained given equation 1.1 and the following relations:
 $m^*v_F = \hbar k_F$, $k_F = (3\pi^2 n)^{1/3}$ and $\tau = l/v_F$.³⁶

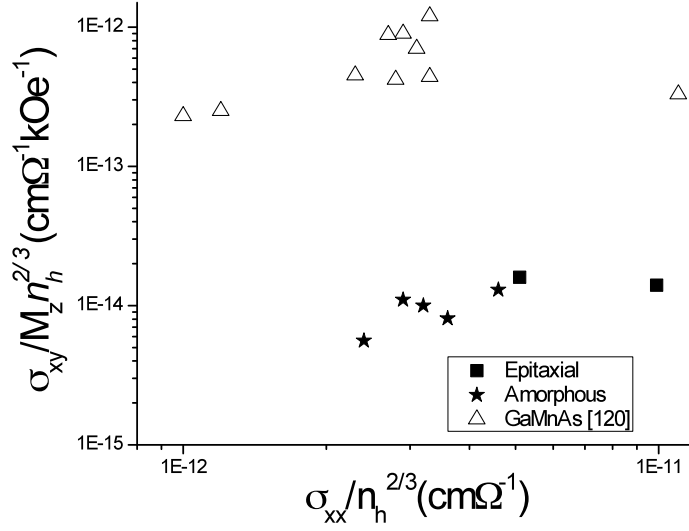


Figure 6.7. $\sigma_{xy}/M_z n_h^{2/3}$ versus $\sigma_{xx}/n_h^{2/3}$ at 2 K for amorphous and epitaxial $\text{Fe}_x\text{Si}_{1-x}$ thin films and at 15 K for $\text{Ga}_{1-y}\text{Mn}_y\text{As}$ thin films from [120].

Figure 6.8 compares σ_{xy}/M_z versus σ_{xx} for our $\text{Fe}_x\text{Si}_{1-x}$ thin films to numerous other itinerant ferromagnets and magnetic semiconductors over a wide σ_{xx} range.^{24,51,52,63,120,130,131,132,133} The three different scaling regimes can be easily observed. In the low σ_{xx} range, where the carrier concentration is changing, the fit to the data shows the similar $\sigma_{xy}/M_z \propto \sigma_{xx}$ dependence ($\sigma_{xy}/M_z \propto \sigma_{xx}^{1.6}$ to be exact). These data further suggest the AHE in the low conductivity regime is dependent on the number of charge carriers.

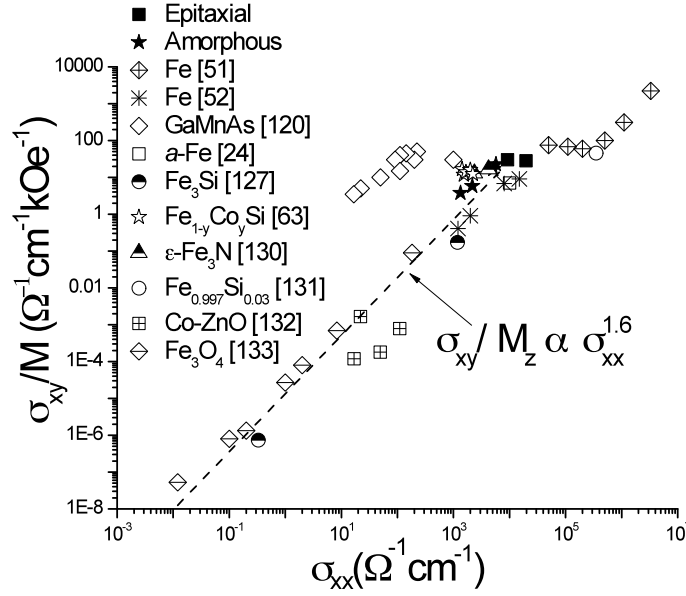


Figure 6.8. σ_{xy}/M_z versus σ_{xx} for epitaxial and amorphous $\text{Fe}_x\text{Si}_{1-x}$ thin films and previously reported itinerant ferromagnets and magnetic semiconductors.^{24,51,52,63,120,130,131,132,133} The line is a fit to the low σ_{xx} data; $\sigma_{xy}/M_z \propto \sigma_{xx}^{1.6}$.

6.4 Conclusion

In conclusion, Hall effect, resistivity, magnetoresistance and magnetization measurements were performed on amorphous and epitaxial $\text{Fe}_x\text{Si}_{1-x}$ thin films, with varying n_h . The longitudinal resistivity at all temperatures decreases with increasing x for all films, and the low Fe concentration amorphous samples ($x=0.43, 0.45$ and 0.55) show a negative temperature coefficient of resistivity. An anomalous Hall effect was observed in all samples and is very large in the amorphous samples. In the epitaxial films, σ_{xy}/M_z is constant, meaning the AHE is dominated by the intrinsic mechanism, as predicted theoretically in this moderate longitudinal conductivity regime. In the amorphous films, we observe $\sigma_{xy}/M_z \propto \sigma_{xx}$, similar to GaMnAs films in this low conductivity range where the intrinsic effect is presumably damped by disorder. In both material systems, the AHE scales approximately with $n_h^{2/3}$, despite orders of magnitude difference in n_h and σ_{xx} . These results were compared to a survey of materials over a broad range in σ_{xx} , and $\sigma_{xy}/M_z \propto \sigma_{xx}$ was also observed, indicating a similar dependence on the number of charge carriers. We hope that this work will stimulate theoretical discussions to better explain the AHE mechanism in the low carrier concentration/low conductivity regime.

Chapter 7: Conclusion

Recently, identifying a material with room-temperature ferromagnetism and a high degree of spin polarization has been of interest for use as a spin-injector in spintronic devices. Fe_3Si has been investigated to this end because it possesses a very high Curie temperature and theoretically predicted high spin polarization. In this work, off-stoichiometry compositions were investigated because thin film growth allows access to varying degrees of chemical and structural order, which can be used to tune and possibly improve the magnetic and electronic properties of the material.

Ultimately, chemical order played the largest role in the magnetic and electronic properties of amorphous and epitaxial $\text{Fe}_x\text{Si}_{1-x}$ films. The magnetization is strongly dependent on the number of Fe-Fe pairs in the local environment, of which there are less in the chemically ordered structures leading to an observed reduction in the magnetic moment of the epitaxial films. As the concentration in the epitaxial films was varied further from stoichiometric Fe_3Si , chemical disorder increased. However, the fully chemically disordered A2 structure was not successfully fabricated; evidently the material has a strong tendency to chemically order. Theoretical and experimental measurements of the electronic band structure revealed disorder broadening as the chemical disorder increased.

The amorphous $\text{Fe}_x\text{Si}_{1-x}$ ($0.43 < x < 0.71$) thin films exhibited some unexpected results. While completely structurally disordered, the local atomic environment was found to be only partially chemically disordered. This structure led to enhancements in the magnetization, anomalous Hall effect (AHE) and spin-polarization versus crystalline films with the same composition. There are more Fe-Fe pairs in the amorphous structure than the D0₃ or B2 structures (although less than a theoretical A2), explaining the observed enhanced moment. The scaling behavior of the AHE was shown to be likely due to the reduction in carrier concentration. Theoretical calculations and experimental measurements of the spin-polarization revealed that it is robust to changes in x and is of the same magnitude or larger than crystalline structures. In fact, the experimental spin polarization in the amorphous films is remarkably larger than experimental measurements on Fe_3Si (D0₃).

This work showed that chemical order is a powerful tool to tune the magnetic and electronic properties of a material system. Although amorphous $\text{Fe}_x\text{Si}_{1-x}$ alloys had not previously been investigated as a potential spin-injector, some compositions showed considerable promise, displaying room temperature ferromagnetism and high spin-polarization. Future work should include fabricating devices to test the viability of these materials as spin-injectors.

Bibliography

- ¹ D. D. Awschalom and M.E. Flatté, *Nature Phys.* **3**, 153 (2007)
- ² K.C. Hall and M.E. Flatté, *Appl. Phys. Lett.* **88**, 162503 (2006)
- ³ S. Datta and B. Das, *Appl. Phys. Lett.* **56**, 665 (1990)
- ⁴ J. Fabian, A. Matos-Abiague, C. Ertler, P. Stano, I. Zutic, *Acta Phys Slovaca* **57**, 565 (2007)
- ⁵ A.H. MacDonald, P. Schiffer, N. Samarth, *Nature Mater.* **4** 195 (2005)
- ⁶ B. Beschoten, P.A. Crowell, I. Malajovich, D.D. Awschalom, F. Matsukura, A. Shen and H. Ohno, *Phys. Rev. Lett.* **83** 3073 (1999)
- ⁷ J.G. Braden, J.S. Parker, P. Xiong, S.H. Chun, N. Samarth, *Phys. Rev. Lett.* **91** 056602 (2003)
- ⁸ Y. Maeda, T. Jonishi, K. Narumi, Y. Ando, K. Ueda, M. Kumano, T. Sadoh, M. Miyao, *Appl. Phys. Lett.* **91**, 171910 (2007)
- ⁹ J. Kudrnovsky, N.E. Christensen, O.K. Andersen, *Phys. Rev. B.* **43**, 5924 (1991)
- ¹⁰ A. Bansil, S. Kaprzyk, P.E. Mijnders, J. Tobola, *Phys. Rev. B.* **60** 13396 (1999)
- ¹¹ K. Hamaya, K. Ueda, Y. Kishi, Y. Ando, T. Sadoh, M. Miyao, *Appl. Phys. Lett.* **93** 132117 (2008)
- ¹² K. Hamaya, T. Murakami, S. Yamada, K. Mibu, M. Miyao, *Phys. Rev. B.* **83** 144411 (2011)
- ¹³ D. Berling, G. Gewinner, M.C. Hanf, K. Hricovini, S. Hong, B. Loegel, A. Mehdaoui, C. Pirri, M.H. Tuilier, P. Wetzel, *J. Magn. Magn. Mater.* **191**, 331 (1999)
- ¹⁴ B. Krumme, C. Weis, H.C. Herper, F. Stromberg, C. Antoniak, A. Warland, E. Shuster, P. Srivastava, M. Walterfang, K. Fauth, J. Minar, H. Ebert, P. Entel, W. Keune, H. Wende, *Phys. Rev. B* **80**, 144403 (2009)
- ¹⁵ M. Walterfang, W. Keune, K. Trounov, R. Peters, U. Ruecker, K. Westerholt, *Phys. Rev. B.* **73**, 214423 (2006)
- ¹⁶ W. A. Hines, A. H. Menotti, J.I. Budnick, T.J. Burch, T. Litrenta, V. Niculescu, K. Raj, *Phys. Rev. B* **13**, 4060 (1976)
- ¹⁷ J.M.D. Coey and M. Venkatesan, *J. Appl. Phys.* **91**, 8345 (2002)
- ¹⁸ J.M.D. Coey, *Magnetism and Magnetic Materials*, Cambridge University Press, Cambridge, 2010
- ¹⁹ H. Okamoto, ASM International, Alloy Phase Diagrams, 1990 [online]
<http://www1.asminternational.org/asmenterprise/APD/ViewAPD.aspx?id=901081>
- ²⁰ J.M.D. Coey, *J. Appl. Phys.* **49**, 1646 (1978)
- ²¹ Ph. Mangin, G. Marchal, B. Rodmacq, Chr. Janot, *Philos. Mag.* **36**, 643 (1977).
- ²² M.B. Stearns, *Phys. Rev.* **129**, 1136 (1963)
- ²³ M. Pugaczowa-Michalska, A. Go, L. Dobrzynski, S. Lipinski, *J. Magn. Magn. Mater.* **256**, 46 (2003)
- ²⁴ S. J. Raeburn and R. V. Aldridge, *J. Phys. F.* **8**, 1917 (1978)
- ²⁵ W. Felsch, *Z. Physik*, **219**, 280 (1969)
- ²⁶ M. Ohta, A. Fujita and K. Fukamichi, *J. Alloys Compd.* **308**, 38 (2000)
- ²⁷ A. P. Malozemoff, A. R. Williams, K. Terakura, V. L. Moruzzi and K. Fukamichi, *J. Magn. Magn. Mater.* **35**, 192 (1983)

- ²⁸ T. Goto, K. Kuroda, H. Komatsu, K. Fukamichi, *J. Magn. Magn. Mater.* **104-107**, 135 (1992)
- ²⁹ J.M.D. Coey, D. Givord, A. Lienard, J.P. Rebouillat, *J. Phys F.: Metal Phys.* **11**, 2707 (1981)
- ³⁰ N. Heiman, N. Kazama, *Phys. Rev. B.* **19**, 1623 (1979)
- ³¹ W. H. Wang, M. Przybylski, W. Kuch, L. I. Chelaru, J. Wang, Y. F. Lu, J. Barthel, H. L. Meyerheim, and J. Kirschner, *Phys. Rev. B* **71**, 144416 (2005)
- ³² M. V. Yablonskikh, J. Braun, M. T. Kuchel, A. V. Postnikov, J. D. Denlinger, E. I. Shreder, Y. M. Yarmoshenko, M. Neumann, and A. Moewes, *Phys. Rev. B* **74**, 085103 (2006)
- ³³ H. Miyazaki, K. Soda, S. Yagi, M. Kato, T. Takeuchi, U. Mizutani, and Y. Nishino, *J. Vac. Sci. Technol. A* **24**, 1464 (2006)
- ³⁴ C. J. Powell, A. Jablonski, I. S. Tilinin, S. Tanuma, and D. R. Penn, *J. Electron Spectrosc. Relat. Phenom.* **98**, 1 (1999)
- ³⁵ S. Tanuma, C. J. Powell, and D. R. Penn, *Surf. Interface Anal.* **37**, 1 (2005)
- ³⁶ C. Kittel, *Introduction to Solid State Physics*, John Wiley and Sons, Inc., New York, 1986
- ³⁷ P.A. Lee, T.V. Ramakrishnan, *Rev. Mod. Phys.* **57** 287 (1985)
- ³⁸ J.H. Mooij, *Phys. Stat. Sol. (A)*, **17**, 521 (1973)
- ³⁹ C.C. Tsuei, *Phys. Rev. Lett.* **57**, 1943 (1986)
- ⁴⁰ T.R. McGuire and R.I. Potter. *IEEE T. Magn.*, **11**, 1018 (1975)
- ⁴¹ I.A. Campbell, A. Fert, *Ferromagnetic Materials vol. 3*, North Holland Publishing Company, Amsterdam (1982)
- ⁴² M. Sakai, D. Kodama, T. Sakuraba, Z. Honda, S. Hasegawa, A. Kitajima, A. Oshima, K. Higuchi, O. Nakamura, *Jpn. J. Appl. Phys.* **51** 023001 (2012)
- ⁴³ S. Onoda, N. Sugimoto, N. Nagaosa, *Phys. Rev. Lett.* **97**, 126602 (2006)
- ⁴⁴ N. Nagaosa, J. Sinova, S. Onoda, A.H. MacDonald, N.P. Ong, *Rev. Mod. Phys.* **82**, 1539 (2010).
- ⁴⁵ J. Smit, *Physica.* **21**, 877 (1955)
- ⁴⁶ J. Smit, *Physica.* **24**, 39 (1958)
- ⁴⁷ D. Venkateshvaran, W. Kaiser, A. Boger, M. Althammer, M.S. Ramachandra Rao, S. T. B. Goennenwein, M. Opel, R. Gross, *Phys. Rev. B.* **78**, 092405 (2008)
- ⁴⁸ D. Xiao, M.-C. Chang, Q. Niu, *Rev. Mod. Phys.* **82**, 1959 (2010)
- ⁴⁹ Y. Shiomi, Y. Onose and Y. Tokura, *Phys. Rev. B.* **79**, 100404 (2009)
- ⁵⁰ T. Miyasato, N. Abe, T. Fujii, A. Asamitsu, S. Onoda, Y. Onose, N. Nagaosa, Y. Tokura, *Phys. Rev. Lett.* **99**, 086602 (2007)
- ⁵¹ R. Schad, P. Beliën, G. Verbanck, V. V. Moshchalkov, Y. Bruynseraede, *J. Phys.: Condens. Matt.* **10**, 6643 (1998)
- ⁵² S. Sangiao, L. Morellon, G. Simon, J. M. De Teresa, J. A. Pardo, J. Arbiol, M. R. Ibarra, *Phys. Rev. B.* **79**, 014431 (2009)
- ⁵³ B.D. Cullity and S.R. Stock, “*Elements of X-ray Diffraction*”, Prentice Hall, New Jersey (2001)
- ⁵⁴ J.H. Hubbell, Wm.J. Veigele, E.A. Briggs, R.T. Brown, D.T. Cromer, R.J. Howerton, *J. Phys. Chem. Ref. Data*, **4**, 471 (1975)

- ⁵⁵ W. Teizer, F. Hellman, R.C. Dynes, *Phys. Rev. B.* **67** 121102(R) (2003)
- ⁵⁶ J. Teillet, F. Varret, J. Juraszek, MOSFIT program, unpublished.
- ⁵⁷ J. Juraszek, O. Zivotsky, H. Chiron, C. Vaudolon and J. Teillet, *Rev. Sci. Instrum.*, **80** 043905 (2009).
- ⁵⁸ M. Newville, “*Fundamentals of XAFS*”, Tutorial, 2004 [online]
http://xafs.org/Tutorials?action=AttachFile&do=view&target=Newville_xas_fundamentals.pdf
- ⁵⁹ M. Newville, B. Ravel, D. Haskel, J.J. Rehr, E.A. Stern and Y. Yacoby, *Physica B* **208/209** 154 (1995)
- ⁶⁰ J.J. Rehr and R. C. Albers, *Rev. Mod. Phys.* **72**, 621 (2000)
- ⁶¹ C.T. Chen, Y.U. Idzerda, H.-J. Lin, N.V. Smith, G. Meigs, E. Chaban, G.H. Ho, E. Pellegrin and F. Sette, *Phys. Rev. Lett.* **75**, 152, (1995)
- ⁶² M. Meinert, J. Schmalhorst, H. Wulfmeier, G. Reiss, E. Arenholz, T. Graf and C. Felser, *Phys. Rev. B.* **83** 064412 (2011)
- ⁶³ N. Manyala, Y. Sidis, J.F. DiTusa, G. Aeppli, D.P. Young and Z. Fisk, *Nature Materials*, **3**, 255 (2004)
- ⁶⁴ P. Bruski, S. C. Erwin, M. Ramsteiner, O. Brandt, K.-J. Friedland, R. Farshchi, J. Herefort and H. Reichert, *Phys. Rev. B.* **83** 140409(R) (2011)
- ⁶⁵ S. H. Vosko, L. Wilk, and M. Nusair, *Can. J. Phys*, **58**, 1200 (1980)
- ⁶⁶ H. Ebert, D. Kodderitzsch, J. Minar, *Rep. Prog. Phys.* **74**, 096501 (2011)
- ⁶⁷ J. Minar, *J. Phys.: Cond. Mat.* **23** 253201 (2011)
- ⁶⁸ S. Chador *et al.* *Europhys. Lett.* **82** 37001 (2008)
- ⁶⁹ O. Sipr, J. Minar, A. Scherz, H. Wende, H. Ebert, *Phys. Rev. B*, **84**, 115102 (2011)
- ⁷⁰ M.I. Katsnelson, A.I. Lichtenstein, *Eur. Phys. J. B*, **30** 9 (2002)
- ⁷¹ L.V. Pourovskii, M.I. Katsnelson, A.I. Lichtenstein, *Phys. Rev. B.*, **72** 115106 (2005)
- ⁷² J. Sanchez-Barriga *et al.* *Phys. Rev. Lett.*, **103** 267203 (2009)
- ⁷³ J. Minar *et al.* *Phys. Rev. B.*, **72** 045125 (2005)
- ⁷⁴ O. Sipr, J. Minar, S. Mankovsky, H. Ebert, *Phys. Rev. B.*, **78** 144403 (2008)
- ⁷⁵ J. P. Perdew, K. Burke, and M. Ernzerhof, *Phys. Rev. Lett.* **77**, 3865 (1996)
- ⁷⁶ Z.Q. Gao and B. Fultz, *Hyperfine Interact.* **94**, 2361 (1994)
- ⁷⁷ K. Trunov, M. Walterfang, W. Keune, N. K. Utochkina and A. Trunova, *Thin Solid Films* **516**, 6205 (2008)
- ⁷⁸ D. de Fontaine, *Met. Trans. A*, **19A** 169 (1988)
- ⁷⁹ A. Prasetyo, F. Reynaud, H. Warlimont, *Acta Metall. Mater.* **24** 1009 (1976)
- ⁸⁰ R.P. Sankaran, C. Ophus, V. Radmilovic, A.M. Minor and J.W. Morris, Jr., *to be published*
- ⁸¹ I. Galanakis, P.H. Dederichs, N. Papanikolaou, *Phys. Rev. B.*, **66** 174429 (2002)
- ⁸² S. Wurmehl, G.H. Fecher, H.C. Kandpal, V. Ksenofontov, C. Felser, H.-J. Lin, J. Morais, *Phys. Rev. B.* **72** 184434 (2005)
- ⁸³ B. Balke, G.H. Fecher, H. C. Kandpal, C. Felser, K. Kobayashi, E. Ikenaga, J.-J. Kim, S. Ueda, *Phys. Rev. B.* **74** 104405 (2006)
- ⁸⁴ C.L. Chien, D. Musser, E.M. Gyorgy, R.C. Sherwood, H.S. Chen, F.E. Luborsky and J.L. Walter, *Phys. Rev. B.* **20**, 283 (1979)
- ⁸⁵ N. Lustig, J.S. Lannin, J.M. Carpenter and R. Hasagawa, *Phys. Rev. B.* **32**, 2778 (1985)

- ⁸⁶ M. Maurer, J.M. Friedt and J.P. Sanchez, *J. Phys. F: Met. Phys.* **15**, 1449 (1987)
- ⁸⁷ K. Moorjani and J.M.D. Coey, *Magnetic Glasses*, Elsevier, New York, 1984.
- ⁸⁸ Ph. Mangin, G. Marchal, *J. Appl. Phys.* **49**, 1709 (1978)
- ⁸⁹ G. Kresse, J. Furthmüller, *Phys. Rev. B* **54**, 11169 (1996)
- ⁹⁰ P.E. Blöchl, *Phys. Rev. B* **50**, 17953 (1994)
- ⁹¹ T. Y. Chen, Z. Tesanovic, and C. L. Chien, *Phys. Rev. Lett.*, **109**, 146602 (2012)
- ⁹² T. Y. Chen, S. X. Huang, and C. L. Chien, *Phys. Rev. B*, **81**, 214444 (2010)
- ⁹³ Li Zeng, J.X. Cao, E. Helgren, J. Karel, E. Arenholz, Lu Ouyang, David J. Smith, R. Q. Wu and F. Hellman, *Phys. Rev. B*, **82**, 165202 (2010)
- ⁹⁴ H.S. Chen and B.K. Park, *Acta Metall. Mater.* **21**, 395 (1973)
- ⁹⁵ R. Hasegawa and R. Ray, *J. Appl. Phys.* **49**, 4174 (1978)
- ⁹⁶ F. Spaepen, *J. Non-Cryst. Solids*, **31**, 207 (1978)
- ⁹⁷ G.S. Cargill III, *Solid State Phys.* **30**, 227 (1975)
- ⁹⁸ J. Logan, *Phys. Stat. Sol. A*, **32**, 361 (1975)
- ⁹⁹ A. Ionescu, C.A.F. Vaz, T. Trypinotis, C.M. Gürtler, H. Garcia-Miquel, J.A.C. Bland, M.E. Vickers, R.M. Dalgliesh, S. Langridge, Y. Bugoslavsky, Y. Miyoshi, L.F. Cohen, K.R.A. Ziebeck, *Phys. Rev. B*, **71** 094401 (2005)
- ¹⁰⁰ J. Herfort, H.-P. Schönherr, A. Kawaharazuka, M. Ramsteiner and K.H. Ploog, *J. Cryst. Growth* **278**, 666 (2005).
- ¹⁰¹ Y. Ando, K. Hamaya, K. Kasahara, Y. Kishi, K. Ueda, K. Sawano, T. Sadoh, and M. Miyao, *Appl. Phys. Lett.* **94**, 182105 (2009)
- ¹⁰² T. Yoshitake, D. Nakagauchi, T. Ogawa, M. Itakura, N. Kuwano, Y. Tomokiyo, T. Kajiwarra, and K. Nagayama, *Appl. Phys. Lett.* **86**, 262505 (2005)
- ¹⁰³ B. Jenichen, V. M. Kaganer, J. Herfort, D. K. Satapathy, H. P. Schönherr, W. Braun, and K. H. Ploog, *Phys. Rev. B* **72**, 075329 (2005)
- ¹⁰⁴ D. A. Shirley, *Phys. Rev. B* **5**, 4709 (1972)
- ¹⁰⁵ F. J. Himpsel, F. R. McFreely, A. Taleb-Ibrahimi, J. A. Yarmoff, and G. Hollinger, *Phys. Rev. B* **38**, 6084 (1988)
- ¹⁰⁶ J. M. Hill, D. G. Royce, C. S. Fadley, L. F. Wagner and F. J. Grunthaner, *Chem. Phys. Lett.* **44**, 225 (1976)
- ¹⁰⁷ W. Smekal, W. S. M. Werner, and C. J. Powell, *Surf. and Interf. Anal.* **37**, 1059 (2005)
- ¹⁰⁸ S. J. Roosendaal, B. van Asselen, J. W. Elsenaar, A. M. Vredenberg, and F. H. P. M. Habraken, *Surf. Sci.* **442**, 329 (1999)
- ¹⁰⁹ E. Landemark, C. J. Karlsson, Y.-C. Chao, and R. I. G. Uhrberg, *Phys. Rev. Lett.* **69**, 1588 (1992)
- ¹¹⁰ B. Egert and G. Panzner, *Phys. Rev. B* **29**, 2091 (1984)
- ¹¹¹ I. N. Shabanova, V. I. Kormilets, and N. S. Terebova, *J. Electron Spectrosc. Relat. Phenom.* **114**, 609 (2001)
- ¹¹² I. N. Shabanova, N. S. Terebova, and V. I. Kormilets, *Phys. Solid State* **42**, 1196 (2000)
- ¹¹³ Y. T. Cui, A. Kimura, K. Miyamoto, K. Sakamoto, T. Xie, S. Qiao, M. Nakatake, K. Shimada, M. Taniguchi, S.-I. Fujimori, Y. Saitoh, K. Kobayashi, T. Kanomata, and O. Nashima, *Phys. Status Solidi A* **203**, 2765 (2006)

- ¹¹⁴H. Ebert, *et al.* The Munich SPR-KKR package, version 5.4, H. Ebert et al. <http://olymp.cup.uni-muenchen.de/ak/ebert/SPRKKR> (2009)
- ¹¹⁵ H. Ebert, in *Electronic Structure and Physical Properties of Solids*, edited by H. Dreyssé (Springer, Berlin, 2000), vol. 535 of *Lecture Notes in Physics*, p. 191.
- ¹¹⁶ J. S. Faulkner and G. M. Stocks, *Phys. Rev. B* **21**, 3222 (1980)
- ¹¹⁷ J. Braun, J. Minár, F. Matthes, C. M. Schneider, and H. Ebert, *Phys. Rev. B* **82**, 024411 (2010)
- ¹¹⁸ H. Ebert and J. Schmitalla, *Phys. Rev. B* **55**, 3100 (1997)
- ¹¹⁹ J. H. Scofield, Tech. Rep. UCRL-51326, LLNL (1973)
- ¹²⁰ S.H. Chun, Y.S. Kim, H.K. Choi, I.T. Jeong, W.O. Lee, K.S. Suh, Y.S. Oh, K.H. Kim, Z.G. Khim, J.C. Woo and Y.D. Park, *Phys. Rev. Lett.* **98**, 026601 (2007)
- ¹²¹ T. Jungwirth, Q. Niu, A.H. MacDonald, *Phys. Rev. Lett.* **88** 207208 (2002)
- ¹²² Y. Pu, D. Chiba, F. Matsukura, H. Ohno and J. Shi, *Phys. Rev. Lett.* **101** 117208 (2008)
- ¹²³ Z. Boekelheide, David W. Cooke, E. Helgren and F. Hellman, *Phys. Rev. B*, **80** 134426 (2009)
- ¹²⁴ F. Hellman, M.Q. Tran, A.E. Gebala, E.M. Wilcox and R.C. Dynes, *Phys. Rev. Lett.* **77** 4652 (1996)
- ¹²⁵ P. Xiong, B.L. Zink, S.I. Applebaum, F. Hellman and R.C. Dynes, *Phys. Rev. B*. **59** R3929 (1999)
- ¹²⁶ E. Helgren, J.J. Cherry, L. Zeng and F. Hellman, *Phys. Rev. B*. **71** 113203 (2005)
- ¹²⁷ W. Teizer, F. Hellman and R.C. Dynes, *unpublished work*.
- ¹²⁸ S. Foner, *Phys. Rev.* **107** 1513 (1957)
- ¹²⁹ Y. Kobayashi, T. Kaneko, M. Kamogawa, K. Asai, K. Akiyama, H. Funakubo, *J. Phys. D: Appl. Phys.* **40** 6873 (2007)
- ¹³⁰ Y.H. Cheng, R.K. Zheng, H. Liu, Y. Tian, Z.Q. Li, *Phys. Rev. B*. **80** 174412 (2009)
- ¹³¹ Y. Shiomi, Y. Onose, Y. Tokura, *Phys. Rev. B*. **79** 100404(R) (2009)
- ¹³² H. S. Hsu, C. P. Lin, S. J. Sun, H. Chou, *Appl. Phys. Lett.* **96** 242507 (2010)
- ¹³³ A. Fernández-Pacheco, J. M. De Teresa, J. Orna, L. Morellón, P. A. Algarabel, J. A. Pardo, and M. R. Ibarra, *Phys. Rev. B*. **77** 100403 (2008)

Appendix A: Anomalous Hall Effect and Out-of-Plane Magnetization

This appendix displays the normalized anomalous Hall resistivity, $\rho_{xy}(\text{AHE})$, and the normalized out of plane magnetization, M_z , for all samples investigated in Chapter 6. The plots show that in all cases $\rho_{xy}(\text{AHE})$ scales with M_z . For all figures, the red symbols are $\rho_{xy}(\text{AHE})$ and the black symbols are M_z . For the amorphous $x=0.45$ and 0.43 samples, the linear ordinary Hall effect contribution has been removed.

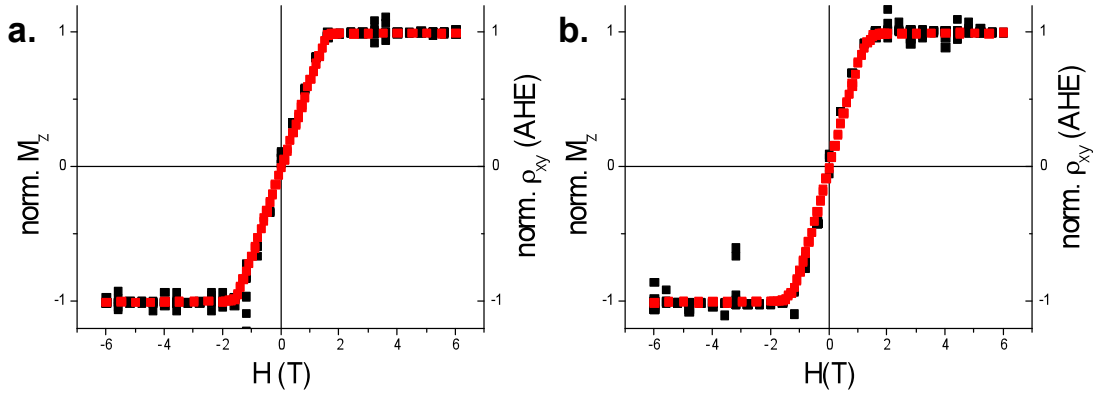


Figure A.1. Normalized out of plane magnetization (black squares) and normalized $\rho_{xy}(\text{AHE})$ (red squares) for amorphous (a) $x=0.71$ and (b) $x=0.65$ films.

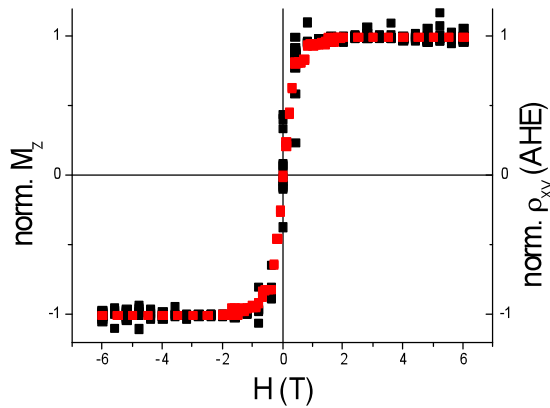


Figure A.2. Normalized out of plane magnetization (black squares) and normalized $\rho_{xy}(\text{AHE})$ (red squares) for the amorphous $x=0.55$ film.

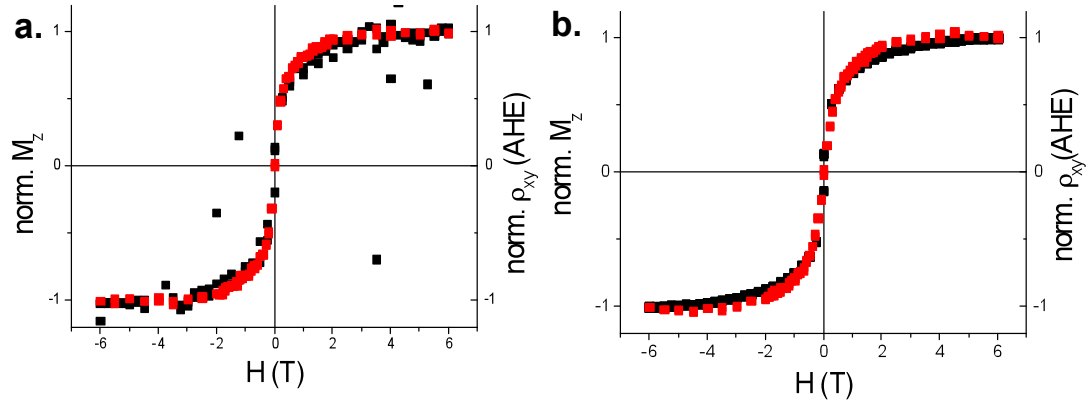


Figure A.3. Normalized out of plane magnetization (black squares) and normalized ρ_{xy} (AHE) (red squares) for amorphous (a) $x=0.45$ and (b) $x=0.43$ films. ρ_{xy} (OHE) has been subtracted from the data.

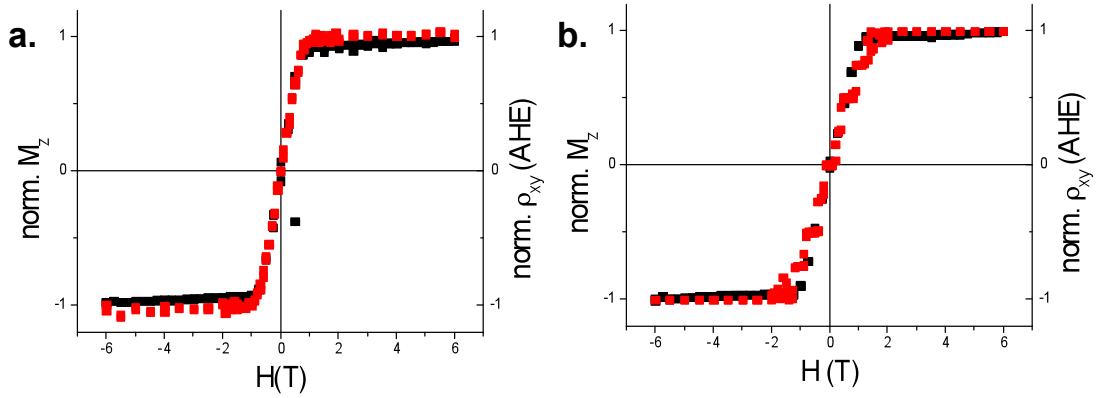


Figure A.4. Normalized out of plane magnetization (black squares) and normalized ρ_{xy} (AHE) (red squares) for epitaxial (a) $x=0.71$ and (b) $x=0.67$ films

Appendix B: In-plane and out-of-plane magnetization

For amorphous and epitaxial samples with $x \geq 0.55$, the magnetic easy axis is in the plane of the film. Figure B1 is a representative plot of in-plane and out-of-plane $M(H)$ curves for an amorphous sample with $x=0.55$, where a clear difference is observed between the two H orientations. In contrast, amorphous samples with $x < 0.55$ (epitaxial samples with $x < 0.55$ were not fabricated) did not exhibit a significant difference between in-plane and out-of-plane orientations; figure B2 shows in-plane and out-of-plane $M(H)$ curves for amorphous (a) $x=0.45$ and (b) $x=0.43$ samples. The curves are slightly different for $x=0.45$ and fall on top of each other for $x=0.43$.

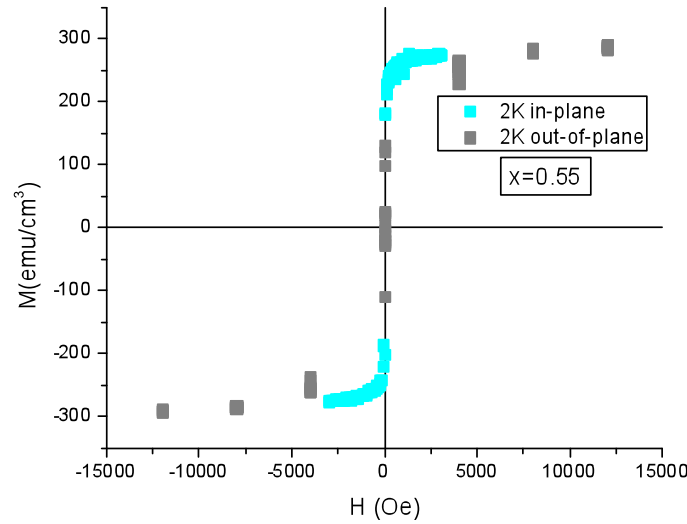


Figure B1. In-plane and out-of-plane $M(H)$ curves at 2 K for an amorphous $x=0.55$ sample. Amorphous and epitaxial samples with $x \geq 0.55$ exhibited similar results.

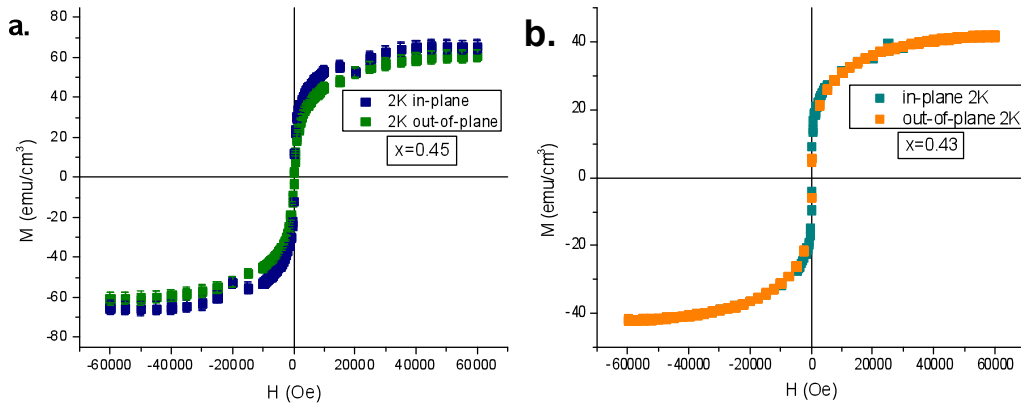


Figure B2. In-plane and out-of-plane $M(H)$ curves at 2 K for amorphous (a) $x=0.45$ and (b) $x=0.43$ thin films.